Elastic Scattering of Protons and Pions From Polarized ^{3}He at Intermediate Energies

by

Bart William Larson

B.Sc. University of British Columbia 1986

M.Sc. Simon Fraser University 1990

A THESIS SUBMITTED IN PARTIAL FULFILLMENT OF

THE REQUIREMENTS FOR THE DEGREE OF

DOCTOR OF PHILOSOPHY

in the Department

of

PHYSICS

SIMON FRASER UNIVERSITY

December 1991

APPROVAL

NAME: Bart William Larson

DEGREE: Doctor of Philosophy

TITLE OF THESIS: Elastic Scattering of Protons and Pions by Polarized ^{3}He at Intermediate Energies

EXAMINING COMMITTEE:

Chairman: Professor E.D. Crozier

Professor O. F. Häusser
Senior Supervisor

Dr. M.C. Vetterli
Research Scientist, SFU and TRIUMF

Dr. P. Schmor
Research Scientist, TRIUMF

Professor D. Boal
Dept. of Physics, SFU

Professor W. P. Alford
External Examiner
Professor, Dept. of Physics, UWO

Date Approved: December 9, 1991

PARTIAL COPYRIGHT LICENSE

Title of Thesis/Project/Extended Essay

Elastic Scattering of Protons and Pions From Polarized ^3He. at Intermediate Energies.

Author:

(signature)

BART LARSON

(name)

Dec/12/91.

(date)

Abstract

A novel cryogenic technique has been used to produce polarized ^{3}He targets with a relative density of up to $p = 12$ atmospheres (or ≈ 3 x 10^{20} ^{3}He atoms/cm^3; $p = 1$ atmosphere corresponds to 760 Torr or 101.3 kPa pressure at 273 K). In these targets the ^{3}He nuclei are polarized by spin exchange collisions with optically pumped rubidium atoms. From transmission measurements at wavelengths of 790-800 nm, pressure shifts, linewidths and lineshape asymmetries for the Rb $5S_{1/2} \rightarrow 5P_{1/2}$ D1 transition have been determined. The Rb spin destruction rate was found to exhibit a quadratic increase versus ^{3}He pressure; this might indicate the importance of Rb-^{3}He-^{3}He collision processes. The transmission results for circularly polarized light are well described by a model which predicts the dependence of the average Rb polarization on Rb density, ^{3}He pressure, light intensity and cell geometry. The Rb – ^{3}He spin exchange cross section, $< \sigma_{SE} v > = 6.1 \times 10^{-20}$ cm^{3}s^{-1}, was found to be independent of ^{3}He pressure up to $p = 12.1$ atmospheres. Maximum ^{3}He polarizations of up to 70% were achieved with cells of 35 cm^3 volume containing ^{3}He at $p = 7$-10 atmospheres.

This target has been used to measure cross sections and spin observables in elastic scattering of both pions and protons from polarized ^{3}He. Angular distributions of cross sections and the spin observables A_{OOON}, A_{OONO}, and A_{OONN} have been measured for the elastic scattering of polarized protons from polarized ^{3}He at incident proton energies of 200, 290, 400 and 500 MeV. Measurements were made at 12 angles in the range 24° - 73° for most of the energies. The results are compared to two nonrelativistic microscopic momentum space optical model calculations. One calculation utilizes the Distorted Wave Impulse Approximation (DWIA) formalism whereas the second uses the Distorted Wave Born Approximation (DWBA). The overall agreement with the data is poor. For the target related spin observables (A_{OOON} and A_{OONN}) the DWBA calculation represents a significant improvement

over the DWIA model but the observables are poorly described whereas the beam related asymmetry (A_{OONO}) is well described.

The measurement of elastic scattering of 100 MeV π^+ from a polarized ^{3}He target is, together with recent measurements on the spin-1/2 nuclei ^{13}C and ^{15}N, the world's database for pion scattering from polarized spin-1/2 complex nuclei (A>2). Measurements have been made at lab angles of 60°, 80° and 100°, with the largest value $A_y = 0.89 \pm 0.12$ occuring at 80° near a cross section minimum. This asymmetry is the largest observed to date in pion scattering from a spin-$\frac{1}{2}$ nucleus. The A_y data are qualitatively reproduced by a schematic model. However agreement with the data is significantly improved when realistic three-body Faddeev wave functions and a full nonlocal DWIA reaction model is used.

Dedication

To my Parents.

Acknowledgement

First, I wish to thank my supervisor, Prof. Otto Häusser, for his financial support and valuable guidance over the duration of this work. I must also thank the many collaborators whose participation was responsible for making the ^{3}He program a success. To Mike Vetterli, Ed Brash, Dave Whittal, and Paul Delheij I am especially grateful for your advice, assistance and friendship.

I am also indebted to my family who have always been there to provide support, both financial and spiritual.

Finally, I wish to thank my fiancée, Tracey, for her patience, support and understanding through all of my years as a student. You have been my inspiration.

Contents

List of Figures

List of Tables

Chapter 1

Introduction

The discovery, by Goudsmit and Uhlenbeck in 1925, that the electron must possess an intrinsic angular momentum or "spin" in order to explain the fine structure in alkalai metal atomic spectra, led to the conclusion that any elementary particle could have spin. It was established shortly thereafter that electrons, protons and neutrons all have a spin $s = \hbar/2$. It was not until 1952 that the first results from scattering of a polarized proton beam from a nuclear target were published. The first nuclear physics experiment to utilize both a polarized beam and a polarized target was performed in 1955. The beam was a polarized neutron beam and the target was an ^{116}In target polarized to the level of 2.1%. The term "polarization" is most easily defined for an ensemble of spin-1/2 particles. For a spin-1/2 particle there exists only two possible values of the $\hat{\mathbf{z}}$ component of the spin, +1/2 and -1/2 in units of $\hbar$ where $\hat{\mathbf{z}}$ defines the quantization axis. If the number of particles in the +1/2 state is N_+ and the number in the -1/2 state is N_- then the polarization of the ensemble is

$$P = \frac{N_+ - N_-}{N_+ + N_-} \tag{1.1}$$

which can have any value between +1 and -1.

Previous polarized target work has focussed on hydrogen and deuterium targets which have been used in nuclear physics experiments to test details in the fundamental N-N interaction. The ^{3}He nucleus is an ideal nucleus with which

to complement this (ongoing) work. ^{3}He nuclei have few enough nucleons to be described by accurate theoretical wave functions, yet large enough to exhibit the complexity of many-body nuclear effects. Nuclear scattering experiments using a ^{3}He target should therefore provide an exceptional testing ground for many-body reaction theories.

1.1 The Polarization of ^{3}He Nuclei

The polarization of the nuclear spin of ^{3}He is of interest from several perspectives. Applications of polarized ^{3}He in atomic physics, surface physics and quantum statistics have been discussed in a recent review by Leduc[1]. The motivation for the present work was the production of polarized ^{3}He targets for applications in nuclear and particle physics. To a good approximation polarized ^{3}He can be viewed as a polarized neutron. The two protons are predominantly in a spatially symmetric S-state, with the unpaired neutron carrying about 90% of the nuclear spin[2]. Quasielastic and deep inelastic scattering of longitudinally polarized electrons from polarized ^{3}He can provide information on the electric and magnetic form factors of the ^{3}He nucleus[3] and on the internal spin structure of the neutron. The strong interaction of slow neutrons with polarized ^{3}He has been used as a spin filter for neutron beams[4]. Experiments in which intermediate energy protons and pions are scattered from polarized ^{3}He determine largely unexplored spin–dependent scattering amplitudes which can be sensitive to both the detailed 3-body wavefunction and the reaction dynamics used in a particular model.

Brute force nuclear orientation methods using low temperatures ($\sim$ 5 mK) and large magnetic fields ($\sim$ 5 T) have achieved sizeable polarizations in solid ^{3}He[5]. The large magnetic fields and low heat capacity of the solid make these targets of limited use for applications in nuclear and particle physics. Presently the only practical methods employ optical pumping, i.e. the absorption of polarized light by the atom, and transfer of the atomic polarization to the nucleus by the hyperfine

interaction. In the optical pumping of metastable ^{3}He the 2^3S_1 - 2^3P transition of helium is pumped by $\lambda = 1.08\ \mu m$ light and the polarization is transferred from the metastable to the ground state by metastability exchange collisions[6]. The low ^{3}He density associated with producing metastables in a weak discharge can be overcome using cryogenic storage cells[7]. At present such targets satisfy the luminosity demands of experiments in nuclear and particle physics if large currents ($\gg 1\ \mu A$) of primary internal or external beams are available.

Experiments with weak primary ($\sim 10^{10}$ particles/second), or with even weaker secondary ($\sim 10^6$-10^7 particles/second), beams require polarized ^{3}He targets with nuclear densities $> 10^{20}$ nuclei/cm^3, 1-2 orders of magnitude more than has been achieved so far with metastable optical pumping. Targets of the necessary figure of merit (which can be defined as the product of areal density times polarization squared) can be produced using optical pumping of alkalis and polarization transfer from the alkali to ^{3}He via spin exchange collisions. This method, which was discovered by Bouchiat *et al.*[8] and studied further by Gamblin and Carver[9], is made possible by the extremely long nuclear relaxation times, T_1, of ^{3}He nuclei achievable in suitable containment cells. Calculations by Herman[10] confirmed that the spin exchange cross sections are surprisingly large for ^{3}He and ^{21}Ne. Polarization of noble gas nuclei by spin exchange has since been actively studied both experimentally and theoretically [11]–[16]. Using solid state diode lasers or dye lasers capable of producing $\sim$ 1 Watt of light output, Chupp and collaborators[17][18] have achieved significant ^{3}He polarizations at high density ($p \approx 3$ atmospheres) although the volumes of these targets were limited to only a few cm^3. With the advent of tuneable Ti:Sapphire (Ti^{3+}:Al_2O_3) lasers, about 5 Watts of infrared light per laser system are now available for optical pumping of Rb or K vapour. Since the volume of Rb vapour which can be pumped to $\approx$ 100% polarization increases linearly with the available laser power [17][18] much larger polarized target volumes can now be realized. A cryogenic technique has been developed at TRIUMF to increase the

target density from $p = 3$ to 12 atmospheres and the target volume to > 35 cm^3. Over the past two years this work has increased the figure of merit of the targets by more than an order of magnitude. This has made it possible to perform hadronic scattering experiments with external proton and pion beams at TRIUMF. Elastic scattering of both protons and pions from polarized ^{3}He is the subject of this thesis.

The tuneability and narrow linewidth ($\sim$ 18 GHz) of Ti:Sapphire lasers makes them suitable for studying the pressure broadened lineshape of the Rb D1 line. Measurements of the D1 lineshape parameters and of the Rb spin destruction rates at various Rb densities and ^{3}He pressures between $p = 3$–12 atmospheres are presented in chapter 2. These properties must be known to predict the average Rb polarization and hence the maximum possible ^{3}He polarization. An unexpectedly strong increase of the Rb spin destruction rate Γ_{SD} with ^{3}He pressure was found. This affects the laser power per unit volume required to produce $\sim$ 100% polarized Rb vapour at large ^{3}He pressures. The pressure dependence of the cross section for Rb–^{3}He spin-exchange collisions and the rates for depolarization processes in the cell volume have also been determined. The presentation and discussion of these results is presented in Chapter 2 preceded by a brief review of the theory of optical pumping and spin exchange and a description of the polarized ^{3}He apparatus and experimental technique.

1.2 $\vec{p}$-$^3\vec{He}$ Elastic Scattering

In the "Optical Model" of nuclear reactions, the incident particle enters a potential well (the field of the nucleus) and is scattered. If the particle is to dissipate energy, i.e. participate in processes other than elastic scattering , this potential must contain an imaginary part in addition to the real part. This is analogous to the absorption of light in a medium with a complex index of refraction; hence the name "Optical Model". Early forms of the Optical Model used a potential well shape similar to that of the nuclear matter density distribution. A frequently used

parametrization of the optical potential was the Woods-Saxon form which is also used to describe nuclear charge and matter distributions. The parameters of the optical potential in this "phenomenological" approach were adjusted to reproduce elastic scattering data for the system of interest. The model was modified to include spin dependence with the addition of a term proportional to $\vec{L} \cdot \vec{S}$. Formal solutions for the scattering amplitude are obtained by solving the Schrödinger equation with this optical potential.

The advent of multiple scattering theories as developed by Watson [19] or Kerman McManus and Thaler (KMT)[20] which gave a prescription for calculating the N-Nucleus optical potential in terms of the free NN interaction (impulse approximation) and the nuclear wavefunction, marked the birth of the "microscopic" approach to N-Nucleus scattering. A brief account of the KMT approach is given in Appendix A. The N-nucleus optical potentials constructed using this formalism contain the full spin and isospin structure of the NN scattering amplitude. Much work has been done in an attempt to unravel the complicated spin structure of this N-nucleus interaction.

Since the elastic scattering of protons from ^{3}He involves four identical particles, if charge independence is assumed, a full description of p-^{3}He scattering requires the solution of a four body problem. Faddeev-type methods have been employed to provide N-^{3}He scattering solutions at energies below 5 MeV [21]. Calculations at intermediate energies are presently being attempted[22]. The most complete calculation available at present is the momentum space microscopic optical model of Landau[23]. The full optical potential consists of the NN T-matrix multiplied by a nuclear spin or matter density which have been obtained from electron scattering data. The p-^{3}He scattering amplitude is obtained by solving the Schrödinger equation with this potential. Although the theory utilizes several approximations it contains no adjustable parameters apart from the choice of the NN T-matrix. The 500 MeV data are also compared to a similar model, developed by Ray *et al.*[24],

which allows for adjustment of the nuclear densities in order to reproduce p-^{3}He cross section and analyzing power data. A more detailed discussion of these models is given in chapter 3.

The $\vec{p}$-$^3\vec{He}$ system is a spin $\frac{1}{2} \otimes \frac{1}{2}$ system and therefore has many similarities to the elementary NN system. In particular the NN and p-^{3}He T-matrices or scattering amplitudes have the same spin-space structure[25][26],

$$\begin{aligned} T &= [(a+b) + (a-b)\vec{\sigma}_p \cdot \hat{\mathbf{n}}\vec{\sigma}_2 \cdot \hat{\mathbf{n}} + (c+d)\vec{\sigma}_p \cdot \hat{\mathbf{m}}\vec{\sigma}_2 \cdot \hat{\mathbf{m}} + (c-d)\vec{\sigma}_p \cdot \hat{\mathbf{l}}\vec{\sigma}_2 \cdot \hat{\mathbf{l}} \\ &+ e(\vec{\sigma}_p + \vec{\sigma}_2) \cdot \hat{\mathbf{n}} + f(\vec{\sigma}_p - \vec{\sigma}_2) \cdot \hat{\mathbf{n}}]/2 \end{aligned} \tag{1.2}$$

where $\vec{\sigma}_p$ refers to the spin of the projectile (proton) and $\vec{\sigma}_2$ to that of the target. The spatial directions are defined so that $\hat{\mathbf{n}}$ is normal to the scattering plane, $\hat{\mathbf{m}}$ is along the direction of momentum transfer and $\hat{\mathbf{l}}$ is in the direction of the incident beam. In the NN system however, the f amplitude is exactly zero due to the fact that target and projectile are identical particles (if charge independence is assumed [23]).

A description of a recent TRIUMF experiment in which the observables A_{OOON}, A_{OONO}, A_{OONN} and σ were measured for the reaction ^{3}He($\vec{p}$,p) at various energies is given in the first part of chapter 3.

The dependence of these observables on the 6 complex amplitudes of Equation 1.2 are[23]

$$\sigma = (|a|^2 + |b|^2 + |c|^2 + |d|^2 + |e|^2 + |f|^2)/2 \tag{1.3}$$

$$A_{OONO} = Re(a^*e + b^*f)/\sigma \tag{1.4}$$

$$A_{OOON} = Re(a^*e - b^*f)/\sigma \tag{1.5}$$

$$A_{OONN} = (|a|^2 - |b|^2 - |c|^2 + |d|^2 + |e|^2 - |f|^2)/2\sigma \tag{1.6}$$

where the first two indices refer to the polarization state of the projectile and the target in the final state, the third to the projectile polarization in the initial state and the last to the target polarization in the initial state. The subscript o means

that the polarization is zero (for the beam) or not measured (for the scattered beam and recoil particles). Since the a, b and e amplitudes are expected to be large[23] for p-^{3}He scattering, the measurement of both A_{OOON} and A_{OONO} provides a clear indication of the magnitude of the f amplitude.

The experiment utilized only $\hat{\mathbf{n}}$ type beam and target polarizations and is the first part of a program which will eventually yield measurements of *all* spin observables which depend only on the beam and target polarizations in the initial state. Although polarized beams have been in use for some time, suitable polarized nuclear targets (A>2) have only recently been developed. Consequently, the only previously existing data on $\vec{\text{p}}$-^{3}He polarization observables were those of Hasell *et al.* [27] who used a liquid target to measure cross sections and analyzing powers (A_{OONO}) in $\vec{\text{p}}$-^{3}He scattering at energies of 200, 300, 415 and 515 MeV although there are also cross section data extending up to 1 GeV[28]. The only other existing proton elastic scattering measurement using a polarized spin-1/2 nuclear target is that of Hoffmann *et al.*[29] performed with 500 MeV protons incident on a polarized ^{13}C target. Measurements of cross sections, analyzing powers and the target related observables A_{OOON} and A_{OONN} for ^{3}He are presented in chapter 3.

1.3 π^+-$^3\vec{\text{He}}$ Elastic Scattering

Asymmetry measurements using polarized nuclear targets have only recently become feasible[30]-[32] and with the development of an optically pumped high density polarized ^{3}He target[32] are possible even with pion fluxes of 10^6–10^7 s^{-1}. Measurements of this type provide valuable new information on the spin dependent part of the π-nucleus scattering amplitude. Much theoretical work has gone into describing and understanding the π–nucleus interaction[33]-[37]. In general, predictions depend on the nuclear structure input, the elementary π–nucleon amplitudes and the reaction model. In the last decade or so, several momentum space calculations which use a first-order optical potential and a multiple scattering series to predict

π-^{3}He elastic scattering observables have been published [35]-[41]. The first attempts to depart from the purely phenomenological approach and incorporate the microscopic formalism [35],[39],[38], led the authors to make some approximations which are unnecessary [40] for the pion scattering case. The "semi-factorization" approximation of Landau[39] is an example. In this model the optical potential is constructed from a simple product of a matter or spin density and the πN T-matrix folded with a harmonic oscillator wavefunction. Since calculations which utilize the full trinucleon wavefunction are now possible[40],[41], it is not necessary to rely on the factorization approximation. Aside from the use of a fully theoretical wavefunction for ^{3}He the principal difference between the factorized approach and the full calculation is that the latter allows for a correct treatment of the Fermi motion of the target nucleons and for nonlocalities or momentum dependence of the NN interaction. The microscopic formalism for π-nucleus scattering follows very closely that of p-nucleus scattering which is outlined in appendix A. Details regarding calculations of π-^{3}He elastic scattering observables are given in chapter 4.

For spin-1/2 targets in the $1p$ shell[30][31],^{13}C and ^{15}N, relatively small asymmetries have been observed. A conclusive interpretation is also made difficult by uncertainties in standard wavefunctions for the nuclear ground state which give a poor description of the measured magnetic form factors, e.g. in ^{13}C [42] at momentum transfers $q \sim 2$ fm^{-1}. In contrast to this the ^{3}He nuclear wave function can be calculated with good accuracy from the Faddeev equations using realistic NN potentials as input[43]. Therefore, for ^{3}He the nuclear structure uncertainties are almost negligible compared to p–shell nuclei and, furthermore, large asymmetries are expected. The $^3\vec{\mathrm{He}}(\pi^+,\pi^+)$ reaction is thus an ideal probe of the detailed spin dependence of the spin $0 \otimes \frac{1}{2}$ nuclear scattering amplitude[39]-[41].

It can be shown[44] that the scattering amplitude T for a spin $0 \otimes \frac{1}{2}$ system

must consist of a spin independent or central part and a spin-dependent part ie.

$$T = f(\theta) + ig(\theta)\hat{\mathbf{n}} \cdot \vec{\sigma} \tag{1.7}$$

where f(θ) is the non-spin-flip (spin independent) amplitude, $g(\theta)$ is the spin-flip amplitude and $\vec{\sigma}$ is the nuclear Pauli spin matrix. Defining $\mathbf{k}$ and $\mathbf{k}'$ as the momentum vectors of incoming and outgoing pions, respectively, the unit vector $\hat{\mathbf{n}}$ $\equiv \mathbf{k}\times\ \mathbf{k}'/|\mathbf{k}\times\ \mathbf{k}'|$ is in the direction perpendicular to the scattering plane. The differential cross section, $\sigma = |f|^2 + |g|^2$, is determined by the incoherent sum of the amplitudes, whereas the analyzing power, $A_y = 2Im\{fg^*\}/\sigma$, is sensitive to the interference between them. To date only cross section measurements have been performed on ^{3}He at a variety of pion energies ranging from 30 [45] to 295 MeV [46]. In π^+-^{3}He scattering the cross section depends strongly on the spin dependent amplitude near the cross section minimum[41] only, since g is near its maximum, f is near its minimum and they are comparable in magnitude. The benchmark test for reaction models has thus been the accuracy to which the cross section minimum was predicted. The analyzing power, on the other hand, has a strong dependence on the magnitude of g and on the relative phase between f and g even when the spin-flip amplitude is significantly smaller than the non-flip one thus retaining sensitivity over a wider range of scattering angle or momentum transfer. An experiment, in which the elastic scattering observables σ and A_y were measured for the reaction ^{3}He(π^+,π^+) at an incident energy of 100 MeV, is described in chapter 4.

Chapter 2

The Optically Pumped Polarized ^{3}He Target

This chapter begins with a discussion of the theory of optical pumping and spin-exchange in Rb-N_2-^{3}He gas mixtures. The polarization of ^{3}He nuclei involves the contact hyperfine interaction between the nuclear spin of ^{3}He and the atomic spin of the alkali (Rb) which is polarized by the optical pumping process. This interaction is effective during the brief time of Rb–^{3}He collisions. Since the time scales for polarization transfer ($\approx$10 hrs) and for optical pumping of the alkali ($\approx$1 ms) differ by seven orders of magnitude the steady state ^{3}He polarization is directly proportional to P_{Rb}, the average alkali polarization in the target volume, independent of the relative concentrations of alkali and ^{3}He. We shall show that transmission data for the alkali D1 line for both linearly and circularly polarized light contain the information necessary to predict P_{Rb}. In addition to its dependence on P_{Rb}, the ^{3}He polarization also depends on the ratio of rates for spin exchange and for depolarization processes in the volume. In our discussion we follow closely the notation of earlier work (see e.g. ref. [18]). The effect of the ^{85,87}Rb nuclear spins is neglected since the laser linewidth ($\approx$ 18 GHz) far exceeds the Rb hyperfine splittings (3.04 GHz and 6.87 GHz respectively).

2.1 The Optical Pumping Process

The first topic of this section is the absorption of linearly polarized light by Rb vapour since it yields information necessary for the interpretation of circularly polarized light absorption. A discussion of the optical pumping and spin exchange processes follows.

2.1.1 Absorption of Linearly Polarized Light by Rb Vapour

Linearly polarized (σ_o) laser light is absorbed by both $m_s = \pm 1/2$ substates of the Rb $5s\ ^2S_{1/2}$ ground state. Since the Rb vapour is always unpolarized, the absorption lineshape parameters can be determined independently of the incident light intensity. These parameters are then used to interpret the light transmission data obtained with circularly polarized light. The Rb volume is illuminated by a uniform, parallel beam of infrared photons of frequency ν. The intensity of the laser light after traversing a sample of thickness x is given by

$$ln[I(0)/I(x)] = \sigma_\nu [Rb]\, x = \kappa_\nu x \tag{2.1}$$

where $[Rb]$ is the rubidium number density, κ_ν is the inverse absorption length, and the cross section for absorption of a photon of wavelength λ_o is

$$\sigma(\delta\nu) = \frac{\lambda_o^2}{8\pi}\Gamma_{nat}\left[\frac{\Gamma}{(\delta\nu)^2 + (\Gamma/2)^2} + \frac{b\delta\nu}{\Gamma}e^{-\frac{|\delta\nu|}{\Gamma_a}}\right]. \tag{2.2}$$

The first term in equation (2.2) describes a Lorentzian lineshape which is symmetric with respect to the detuning parameter $\delta\nu = \nu - \nu_o(p)$. The total pressure broadened width Γ is much larger than the natural linewidth Γ_{nat} (5.66 MHz), the Doppler broadened width (0.6 GHz), or the laser linewidth (18 GHz). In addition to pressure broadening, one observes a pressure shift of the resonance frequency, $\nu_o(p) - \nu_o(0)$, and an asymmetry in the lineshape. The cause of these effects can be viewed[47,48] as a distortion of the Rb $5s\ ^2S_{1/2}$ and $5p\ ^2P_{1/2}$ atomic levels by the Rb-^{3}He interatomic potential. The second term in equation 2.2 is a convenient

parametrization of the observed lineshape asymmetry, characterized by two new parameters b and Γ_a. It should be noted that this term does not contribute to the frequency integral of the cross section which is related to the D1 oscillator strength (f) via

$$\int_{-\infty}^{+\infty} \sigma \; d(\delta\nu) = \frac{\lambda_o^2}{4}\Gamma_{nat} = \pi r_e c f, \tag{2.3}$$

independently of pressure broadening. For the allowed, strong electric dipole D1 transition it is safe to assume that the free values $\Gamma_{nat} = (2\pi\tau)^{-1} = 5.66$ MHz and $f = 0.337$ are unchanged by the presence of the ^{3}He buffer gas. Since the asymmetric part of the absorption cross section is identically zero at the resonance frequency ($\delta\nu = 0$) the absorption maximum is unaffected by it. For more thorough discussions of the physics of pressure broadened lineshapes the reader is referred to refs. [47,48] .

2.1.2 Polarization of Rb by Absorption of Circularly Polarized Light

Unlike linearly polarized D1 light which is absorbed by both magnetic substates of the $5s\ ^2S_{1/2}$ Rb ground state, circularly polarized $\sigma_\pm$ light can be absorbed by the $m_s = \mp 1/2$ substate only. The propagation of the σ_+ light intensity in the medium is described by the equation

$$\frac{dI_\nu^+(x)}{dx} = -2I_\nu^+ \sigma_\nu [Rb] \rho_- \tag{2.4}$$

where σ_ν is the cross section for scattering of linearly polarized light in unpolarized Rb vapour equation 2.2, and I_ν^+ is the intensity of circularly polarized σ_+ light incident on the sample. The m-dependence of the transition probability accounts for the factor of 2. The case of optical pumping with σ^+ light is displayed in Figure 2.1.

For ease of notation we define rates for circularly and linearly polarized photons, $\gamma_\nu^+ = I_\nu^+ \sigma_\nu$ and $\gamma_\nu^o = I_\nu^o \sigma_\nu$, respectively. Making use of the identity $\rho_+ = 1 - \rho_-$,

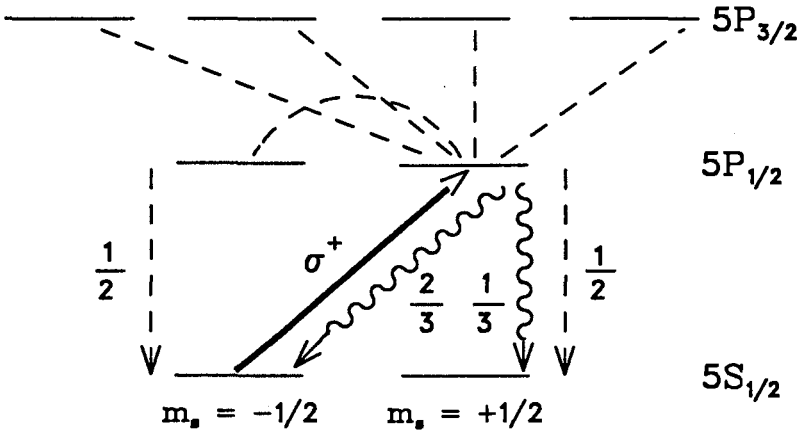

Figure 2.1: Optical pumping of Rb vapour with σ^+ light. The solid arrow depicts the absorption of circularly polarized light by the Rb vapour. The wavey lines indicate radiative decay to the ground state. The dashed lines represent nonradiative quenching and mixing due to collisions with N_2 molecules.

we obtain the occupation probabilities ($\rho_\pm$) of the $m_s = \pm 1/2$ substates from the time-independent solution of the optical pumping rate equation

$$\frac{d\rho_+(x)}{dt} = \left(\gamma_\nu^+(x) + \gamma_\nu^o(x) \ + \Gamma_{SD} - D\frac{d^2}{dx^2}\right)\rho_-(x) - \left(\frac{\Gamma_{SD}}{2} + \frac{\gamma_\nu^o(x)}{2}\right) = 0\,. \quad (2.5)$$

The spin destruction rate, $\Gamma_{SD} \approx <\sigma_{SD}v>[Rb]$, has previously been assumed (see e.g. ref. [17]) to represent Rb depolarization in Rb-Rb ($\uparrow\uparrow \rightarrow \uparrow\downarrow$) collisions where $<\sigma_{SD}v>$ is the velocity averaged spin destruction cross section. It will be shown that additional spin destruction arises from the presence of ^{3}He buffer gas. D, an effective

diffusion constant for Rb atoms in ^{3}He gas, is introduced to account for differences in the Rb polarizations near the cell boundary and in the uniform medium. A further assumption used in deriving the above rate equation is that collisional mixing in the excited ($5p\ ^2P_{1/2}$) state due to the presence of a small amount of N_2 quench gas results in 50% probabilities of de-excitation to the $m_s = -1/2$ and $m_s = +1/2$ substates of the ground state. We have calculated[49] the quenching factor for the Rb D1 line at an N_2 pressure of 120 torr to be $\approx$50 using experimental quenching cross sections[50]. This is dicussed in more detail in the following section. Numerical integration of equation (2.5) shows that the equilibrium polarizations, $P(x) = \rho_+(x) - \rho_-(x)$, are attained about 1 ms after the laser light is switched on. The possibility that the light is elliptically polarized rather than circularly polarized is included in the γ° terms. We have found that the ellipticity of the laser light used for optical pumping can be made to be negligibly small (see Section 2) and therefore disregard these terms in the following discussion.

The traditional method of determining the spin destruction rate Γ_{SD} (see e.g. ref. [10]) consists of starting from unpolarized alkali vapor, then illuminating the sample with light of a fixed frequency such that the light transmission grows exponentially from a finite small value to the equilibrium value. We have used here instead the steady-state solution of equation 2.5 and extracted Γ_{SD} from the detailed frequency dependence. The steady-state method is sensitive not only to Γ_{SD}, but also to depolarization effects at the cell walls which can easily be missed by the single-frequency time dependent method.

In the steady state the propagation of the laser light can be followed through the sample numerically by solving the time-independent equations 2.4 and 2.5 at each value of x starting with the boundary condition $P_{Rb} = 0$ at the cell wall, $x = 0$. The ansatz

$$P_{Rb} = \beta(1 - e^{-\alpha x}) \tag{2.6}$$

is used to model the rapid build up of the Rb polarization as a function of distance

from the cell wall. The quantities $\rho_-(x) = \frac{1}{2}(1 - P_{Rb})$ and $d^2\rho_-/dx^2$ can be written in terms of α and β,

$$\rho_-(x) = \frac{1}{2}(1 - \beta + \beta e^{-\alpha x}) \tag{2.7}$$

and

$$\frac{d^2\rho_-(x)}{dx^2} = \frac{\beta\alpha^2}{2} e^{-\alpha x}. \tag{2.8}$$

Substitution of these two quantities into the optical pumping rate equation 2.5 yields the required expressions for α and β,

$$\beta = \frac{\gamma_\nu^+}{\gamma_\nu^+ + \Gamma_{SD}} \qquad (x \to \infty) \tag{2.9}$$

$$\alpha = \sqrt{\frac{\gamma_\nu^+ + \Gamma_{SD}}{D}} \qquad (x = 0), \tag{2.10}$$

where $\beta \approx 1$ for all x if the incident light intensity is sufficiently high and α^{-1} gives the effective thickness of an unpolarized Rb layer that exists at the cell wall. One can then calculate $\alpha(x)$ and $\beta(x)$ at each x given the value of $\gamma_\nu^+(x)$ and subsequently determine $P_{Rb}(x)$ where

$$P_{Rb}(x) = \rho_+(x) - \rho_-(x) = \frac{\gamma_\nu^+(x)}{\gamma_\nu^+(x) + \Gamma_{SD}} \left(1 - e^{-\sqrt{\frac{\gamma_\nu^+(x)+\Gamma_{SD}}{D}}x}\right). \tag{2.11}$$

Fitting the data obtained at a range of frequencies centered on the resonance frequency, provides values for Γ_{SD}, the average Rb polarization, and the effective diffusion constant D. From equation 2.11 it is apparent that high Rb polarization requires the ratio of photon absorption rate γ_ν^+ to spin destruction rate Γ_{SD} to be large.

2.1.3 Radiationless Quenching of Excited Rb Atoms

The N_2 molecule has a virtual continuum of vibrational and rotational levels which can absorb energy and angular momentum from the electrons in excited Rb orbitals during Rb-N_2 collisions. These interactions cause non-radiative transitions from the Rb $5p\ ^2P_{1/2}$ and $5p\ ^2P_{3/2}$ levels to the $5s\ ^2S_{1/2}$ level. Therefore the normally radiative

Table 2.1: Quenching and Mixing Cross Sections for Rb-N_2 Mixtures

Cross Section	Value ($\AA^2$)
Q_{10}	58 ± 12
Q_{20}	43 ± 11
Q_{12}	16
Q_{21}	23

decay mode is said to be "quenched". Rb-N_2 collisions also cause mixing between the $5p\ ^2P_{1/2}$ and $5p\ ^2P_{3/2}$ levels. Using the collision cross sections for these processes given by Krause *et al.* [50], it is possible to describe the evolution of the population of Rb atoms in a particular angular momentum state i.e. the $5p\ ^2P_{1/2}$ state by a rate equation,

$$\frac{dN_{p_{1/2}}}{dt} = S_1 + N_{p_{3/2}} Z_{21} - N_{p_{1/2}}[\tau_1^{-1} + Z_{12} + Z_{10}] = 0 \tag{2.12}$$

for which $\frac{dN_{p_{1/2}}}{dt} = 0$ is the steady state condition. S_1 is the rate at which electrons are optically pumped from the $5S_{1/2}$ level into the $5P_{1/2}$ level. This is accomplished using laser light of 794.8 nm wavelength. The transition frequencies Z_{10}, Z_{12} and Z_{21} correspond to the transitions, $5P_{1/2} \rightarrow 5S_{1/2}$, $5P_{1/2} \rightarrow 5P_{3/2}$ and $5P_{3/2} \rightarrow 5P_{1/2}$, respectively. The frequencies are defined by $Z_{ij} = N_{N_2} V_r Q_{ij}$ where N_{N_2} is the N_2 number density, V_r is the average relative velocity, and Q_{ij} is the cross section for the appropriate transition. Quenching cross sections for the Rb-N_2 mixture are given in table 2.1.

Similar rate equations can be written for the remaining level and for the case of optical pumping to the $5P_{3/2}$ level using 780 nm light. Solution of this coupled set of linear equations yields the relationship

$$\left(\frac{I_0}{I}\right)_1 = 1 + \tau_1 Z_{10} + \tau_1 Z_{12} - \frac{\tau_1 \tau_2 Z_{12} Z_{21}}{1 + \tau_2 Z_{20} + \tau_2 Z_{21}} \tag{2.13}$$

for pumping with D1 (794.8 nm) light. The mean radiative lifetimes of the $5P_{1/2}$ state (τ_1) and $5P_{3/2}$ state (τ_2) are 2.81×10^{-8} s and 2.70×10^{-8}s respectively. I_0 is the resonance flourescent intensity measured in the absence of N_2 quench gas and I is the same quantity measured with the addition of quench gas. About 120 torr of N_2 quench gas in Rb vapour at $\sim$ 450 K yields $(I_0/I)_1 \approx 50$.

2.1.4 Polarization Transfer by Spin Exchange Collisions

The ^{3}He polarization ($\tilde{P}$) is given by $\tilde{\rho}_+ - \tilde{\rho}_-$ where $\tilde{\rho}_\pm$ is the probability of finding the ^{3}He nucleus with magnetic quantum number $m = \pm 1/2$. The ^{3}He polarization is strongly dependent on three parameters: i) the Rb polarization P_{Rb}, ii) the velocity averaged spin exchange cross section $< \sigma_{SE} v >$, and iii) the wall relaxation rate of the cell Γ_w. The time evolution of the ^{3}He polarization is inferred from the rate equation

$$\frac{d\tilde{\rho}_+}{dt} = \left[\frac{\Gamma_w}{2} + \gamma_{SE}\ \rho_+\right]\tilde{\rho}_- - \left[\frac{\Gamma_w}{2} + \gamma_{SE}\ \rho_-\right]\tilde{\rho}_+ \ , \tag{2.14}$$

where $\gamma_{SE} = < \sigma_{SE} v > [Rb]$. With the substitution $\tilde{\rho}_- = 1 - \tilde{\rho}_+$, one obtains the solution

$$\tilde{P}(t) = P_{Rb}\frac{\gamma_{SE}}{\gamma_{SE} + \Gamma_w}\left(1 - e^{-(\gamma_{SE}+\Gamma_w)t}\right) \tag{2.15}$$

if the laser light is switched on at $t = 0$, and

$$\tilde{P}(t) = \tilde{P}(0)e^{-(\gamma_{SE}+\Gamma_w)t} \tag{2.16}$$

if the laser is switched off at $t = 0$. Equation 2.15 describes the optical pumping situation. High polarization is obtained when $P_{Rb} \approx 1$ and $\gamma_{SE} \gg \Gamma_w$. Equation 2.16 describes the evolution of the ^{3}He polarization in the presence of unpolarized Rb vapour (laser off). As P_{Rb} does not appear in this equation, polarization decay at high temperature provides the most accurate means of determining $\gamma_{SE} + \Gamma_w$. Γ_w can be measured separately at low temperature where γ_{SE} is negligibly small.

2.2 Experimental Technique

Polarized ^{3}He target cells produced at TRIUMF have been designed to meet the requirements of proton and pion scattering experiments. For proton beam experiments where the beam diameter is approximately 2 mm, target cells of 17 mm outer diameter and 8 cm length (volume $\approx$ 17 cm^3) are adequate. For experiments with secondary pion beams, the beam diameter is much larger (2.5 cm full width at $\frac{1}{10}$ maximum) and larger diameter target cells are needed. Cells for pion applications have typically 23-26 mm inner diameter and a length of 8 cm (volume $\approx$ 35 cm^3).

2.2.1 Target Cell Construction

Cells made of alumino–silicate glass (Corning 1720) are more resistant against reactions with alkali atoms and exhibit longer wall relaxation times, Γ_w, than other types of glass. A schematic drawing of the setup used in making high density polarized ^{3}He target cells is displayed in Fig. 2.2. The target cell is connected by a thin capillary to a glass manifold also made of Corning 1720 glass. The manifold is pumped down to a pressure of $< 5\text{x}10^{-8}$ Torr and baked out at T $\approx$ 250 °C for several days. A sealed glass ampule which contains the Rb metal is broken by the impact of a glass-coated steel ball and the Rb is subsequently chased by flame into the cell portion of the manifold. The system is then filled with ultra–high purity ^{3}He gas which has passed through a tube immersed in liquid ^{4}He. The liquid helium acts as a cold trap for further purification of the ^{3}He gas. From the opposite side a few Torr of ultra–high purity N_2 quench gas is added to the manifold contents. The N_2 gas passes through a trap cooled to 77 K by liquid N_2 for additional purification.

The manifold pressure is measured by a BARATRON pressure transducer to an accuracy < 1 Torr. The fraction f of the total volume that the cell occupies is determined by submerging the cell in liquid N_2 (T = 77 K) after the ^{3}He gas has been added, i.e.

$$f = (\frac{p_R}{p_{77}} - 1)/(\frac{T_R}{77K} - 1)\ , \tag{2.17}$$

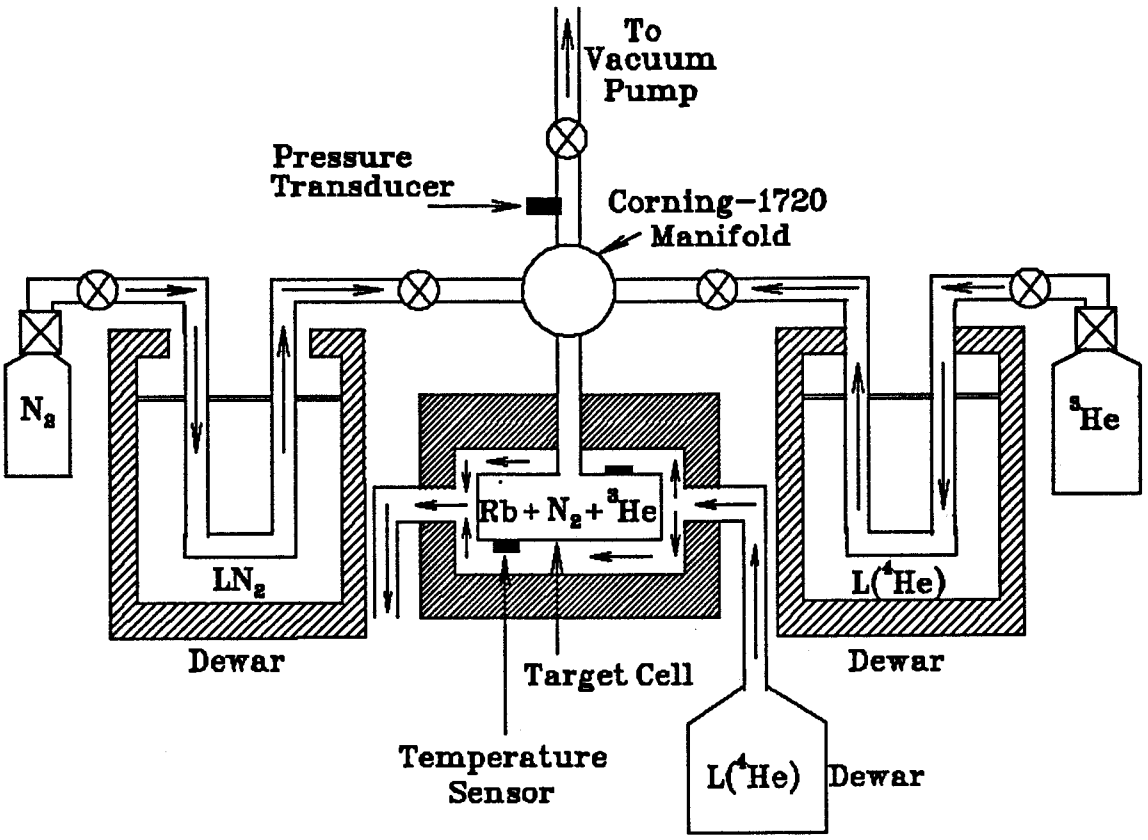

Figure 2.2: Apparatus for making ^{3}He target cells.

where T_R and p_R are room temperature and pressure. The target cell is then enclosed in an insulated cavity and cooled by the flow of helium gas from a liquid helium dewar. Passing the cold gas (T < 8 K) over the cell surface causes an increase of the ^{3}He density in the cell, and a decrease in the warm part of the manifold. The temperature of the cell is measured to an accuracy of ± 1 K at T = 10 K by two independent silicon diode thermal resistors. As the cell is cooled, the pressure in the manifold drops below atmospheric pressure, which ensures that the capillary will seal itself when the cell is pulled from the manifold by melting the capillary with a flame. The final cell pressure at 273 K is then given by $p_{273} = \left(\frac{273}{T_C}\right) p_C$, where T_C is the temperature of the cold cell at the moment the capillary is sealed, and p_C is the pressure measured by the transducer. In practice, temperature fluctuations encountered while the cell is being pulled off by application of the flame, render a direct temperature reading inaccurate. Instead, the effective cell temperature at pulloff is determined from

$$T_C = \frac{T_R p_C f}{p_S - (1-f)p_C} , \tag{2.18}$$

where p_S is the pressure at room temperature. The relative density p can thus be obtained to an accuracy of ±2%. The pressures for some of our best cells are given in Table 2.3 together with wall relaxation times Γ_w^{-1}.

2.2.2 The Optical Pumping Apparatus

The cells are heated to ~450 K in an oven made of the polyimide VESPEL to produce Rb vapour of the required number density [Rb] ≈ 4 x 10^{14} cm^{-3}. The oven has a distributed heat flow around the cell which can be finely adjusted. This was necessary to reduce temperature gradients over the cell volume which introduce large uncertainties in [Rb]. Care was taken that the temperature variation did not exceed 3 K over the full cell surface. An uncertainty of ± 1.5K at 453 K implies a 6% uncertainty in the Rb number density.

A parallel beam of infrared light from a frequency tuneable Ti:Sapphire laser is

used to uniformly illuminate the cylindrical glass cells perpendicular to the 8 cm long cell axis (see Fig. 2.3). The Ti:Sapphire laser is continuously pumped by a high power Ar^+ ion laser with $\sim$ 20–25 Watts of visible light. The efficiency of converting the Ar pump light into infrared light at 794.7 nm is $\sim$ 20%. We have two such systems running in parallel producing a combined power of $\approx$ 8–10 Watts of 795 nm light. For polarized target experiments the full available power is used, whereas for the transmision measurements the laser power was reduced to retain sensitivity to the spin destruction rate, Γ_{SD}.

The laser linewidth ($\sim$ 18 GHz) is much smaller than the total absorption width Γ of the Rb D1 line which is dominated by pressure broadening. The laser lineshape may therefore be considered a delta function for the purpose of calculating the frequency-dependent cross section (equation 2.2) as was assumed in Section 2.1. The average frequency of the infrared light was measured with a BURLEIGH wavemeter. The transmitted light intensity was measured with a NEWPORT 818-SL photodiode, calibrated for the frequency range of interest relative to two COHERENT power meters which agreed to better than 2%. Collimation of the photodiode to a small area (0.07 cm^2) ensured that the light traversed nearly the full inner diameter of the glass cells. Measurements of the transmitted light intensities over a range of frequencies near the D1 resonance determine the Rb absorption lineshape.

The frequency calibration of the Ti:Sapphire laser could be checked frequently and conveniently by observing D1 and D2 resonance fluorescence in a reference cell which contained pure Rb vapour at $\approx$450 K. This was essential for measurements of the small pressure shifts of the D1 and D2 absorption maxima. Experimentally determined corrections were applied to the data to account for reflection, absorption and refraction effects in the glass of the cell and of the entrance and exit windows of the oven in which it was mounted. Small corrections were also necessary to renormalize small frequency-dependent variations in the intensity of the incident light. Transmission scans were performed on four cells, each containing several mg

of Rb metal, ≈120 Torr of N_2 quench gas (relative density $p = 0.16$ atmospheres) and ^{3}He gas of relative density $p = 2.94$, 6.44, 8.97, and 12.1 atmospheres, respectively (see Table 2.2). The results obtained are presented in the following section. For scans with circularly polarized light a 3 mT holding field was applied along the direction of the incident light.

Measurements of γ_{SE} required that the cells be optically pumped for several hours to build up the ^{3}He polarization. The laser light was then blocked to allow the decay of the polarization. The bulk ^{3}He polarization could be analyzed and reversed using the nuclear magnetic resonance (NMR) technique of adiabatic fast passage (AFP) at a frequency of ~100 kHz. At least two decay curves were measured for each cell: one at room temperature to determine the wall relaxation rate Γ_w, and one at T ~ 450 K to determine $\gamma_{SE} + \Gamma_w$.

Absolute normalization factors were obtained by comparing the ^{3}He AFP NMR signals (typically 0.3 V) with weak proton AFP NMR signals from water-filled cells of the same dimension (typically 1 μV). Our NMR setup is similar to the one described by Chupp *et al.*[17]. An independent check of the NMR method has recently been developed at TRIUMF[51]. The new method is based on the special properties of the $^3\vec{\mathrm{H}}\mathrm{e}(\vec{\mathrm{p}},\pi^+)^4\mathrm{He}$ reaction and is sensitive only to ^{3}He in the beam interaction region. Parity conservation in the strong interaction, channel spins 1 and 0 for entrance and exit channels, and parity change in the reaction, imply the identities $A_{OONN} = 1$ and $A_{OONO} = A_{OOON}$ for spin correlation parameter and beam- and target-related analyzing powers[44]. After determining the beam-related analyzing power A_{OONO} for 416 MeV polarized protons at a laboratory scattering angle of 28°, absolute ^{3}He polarizations were obtained to an accuracy of ±0.02. The absolute ^{3}He polarization results from the reaction method are in good agreement with the AFP NMR measurements. The reaction method is more direct and less susceptible to systematic errors than NMR, but requires expensive accelerator time. The ^{3}He polarization results of the present work were obtained with the more readily

available NMR method.

2.2.3 Principles of NMR

To a very good approximation a gas of ^{3}He atoms can be considered an ensemble of free spin - 1/2 particles. A discussion of NMR techniques involves determining the equations of motion of such an ensemble in the presence of an arbitrary magnetic field. First the case of a static magnetic field H_o will be considered[52]. This will introduce the formalism which will later be applied to the case where the field is no longer static.

In the Heisenberg picture, the equation of motion for a spin operator $\vec{I}$ is

$$\frac{d\vec{I}}{dt} = \frac{i}{\hbar}[\mathcal{H}, \vec{I}] \tag{2.19}$$

where the Hamiltonian $\mathcal{H}$ for a spin in a magnetic field $\vec{H}$ is $\mathcal{H} = -\gamma\hbar\vec{H}\cdot\vec{I}$. This equation holds in the general case where a static magnetic field defines the spin quantization axis. It is customary to label this direction $\hat{z}$. Evaluating the commutator for this component of the spin, the equation of motion becomes

$$\frac{d\vec{I}}{dt} = -i\gamma[(H_xI_x + H_yI_y + H_zI_z), I_z] = \gamma(H_yI_x - H_xI_y) = \gamma(\vec{I}\times\vec{H})_z \tag{2.20}$$

which is precisely the form of the classical equation of motion for the precession of a magnetic moment $\vec{M}$ in a magnetic field

$$\frac{d\vec{M}}{dt} = \gamma\vec{M}\times\vec{H}\ . \tag{2.21}$$

Since the classical description gives the same result as a quantum mechanical one, only a classical treatment will be given here.

Since it is of interest to consider the perturbation of a spin sytem in a static magnetic field by an oscillating magnetic field, it will be illuminating to transform the equations of motion to a reference frame which rotates about the static magnetic field axis at an angular velocity ω. It is easily shown (see for example Abragam[52])

that the rate of change of an arbitrary time dependent vector $(d\vec{A}(t)/dt)_L$ in the lab frame is related to that in the rotating reference frame by

$$\left(\frac{d\vec{A}(t)}{dt}\right)_L = \left(\frac{d\vec{A}(t)}{dt}\right)_R + \vec{\omega} \times \vec{A} \,. \tag{2.22}$$

Using equation 2.22 and substituting $\vec{M}$ for $\vec{A}$ it is evident that

$$\left(\frac{d\vec{M}(t)}{dt}\right)_R = \gamma \vec{M} \times \left(\vec{H} + \frac{\omega}{\gamma}\right) \tag{2.23}$$

This equation warrants some discussion. First, it is evident that the form of equation 2.23 is identical to that of Eqn. 2.21 if the magnetic field is replaced by an effective field $H_e = H + \omega/\gamma$. If we consider the case where H is a static magnetic field H_o then $\vec{M}$ will be constant in the rotating frame if we choose the angular velocity $\omega = -\gamma H_o$. In the laboratory frame the magnetization is then precessing about the static field direction. This is just the well known Larmor precession.

We would now like to consider the case where the total field H is the sum of the constant field H_o in the $\hat{z}$ direction and a rotating field H_1 of angular velocity ω pointing in the $\hat{x}$ direction in the rotating frame. In the rotating frame the field is still static and we have

$$H_e = \left(H_o + \frac{\omega}{\gamma}\right)\mathbf{k}' + H_1\mathbf{i}' \,. \tag{2.24}$$

Defining an additional characteristic angular velocity $\omega_1 = -\gamma H_1$, the magnitude of the effective field is

$$H_e = \left[\left(H_o + \frac{\omega}{\gamma}\right)^2 + H_1^2\right]^{\frac{1}{2}} = -\frac{a}{\gamma} \tag{2.25}$$

where

$$a = -\left[(\omega_o - \omega)^2 + \omega_1^2\right]^{\frac{1}{2}} - \frac{\gamma}{|\gamma|} \,. \tag{2.26}$$

The angle θ between the effective and static fields is then given by

$$\tan(\theta) = \frac{H_1}{H_o + \frac{\omega}{\gamma}} = \frac{\omega_1}{\omega_o - \omega} \tag{2.27}$$

$$\sin(\theta) = \frac{\omega_1}{a}, \quad \cos(\theta) = \frac{\omega_o - \omega}{a}. \tag{2.28}$$

The magnetic moment M then precesses about the direction of the effective field H_e. From these equations it is evident that addition of the oscillating field has little effect if its frequency is far removed from ω_o and it is small enough in magnitude. However, an oscillating field which is small compared to H_o can reorient the magnetization if the frequency difference $\omega_o - \omega$ is roughly of the order of ω_1. This is the basic principle of Magnetic Resonance.

Experimentally the reorientation of the magnetization is performed by application of an r.f. driving field of frequency ω at right angles to the static field H_o. The r.f. driving field is actually a linearly oscillating field, however it can be considered to be a superposition of two rotating fields; one rotating with angular velocity $+\omega$ and one at $-\omega$. The effect of the component rotating with $-\omega$ is negligible (recall that $\omega_o = -\gamma H_o$) due to the fact that this frequency is removed from the resonance value by 2ω. The value of H_o is chosen so that initially the Larmor frequency is far removed from ω. The static field is then ramped sweeping ω_o from $\omega_o \ll \omega$ to $\omega_o \gg \omega$. During the "Adiabatic Fast Passage" the "effective" field which is initially in the direction of H_o, is rotated by π radians with respect to H_o. The term adiabatic refers to the fact that the magnitude of M remains constant. This is realized if the direction of the H_e is varied slowly enough to allow the magnetization to retain its alignment with the effective field. It can be shown that the adiabatic condition is[52]

$$\frac{dH_o}{dt} \ll \gamma H_1^2 \,. \tag{2.29}$$

The motion of an ensemble of spins that interact with each other and the bulk lattice is described by a set of phenomenological equations developed by Bloch [53] in 1946. He postulated that, in a static magnetic field, any z component of the magnetization $M_z = \chi_o H_z$ of a system of interacting spins will relax toward its equilibrium value M_o with a time constant denoted as T_1 ie. $dM_z/dt = (M_z - M_o)/T_1$. This is referred to as the longitudinal relaxation time of the sample. Furthermore, if the sample were

to be given some magnetization in the x or y directions then this would approach 0 with a time constant of T_2 called the transverse relaxation time (assuming there is no constant field in the $x-y$ plane). The primary source of this type of relaxation in the ^{3}He system is the magnetic field inhomogeneity. It is further proposed that, in the presence of a static magnetic field and a much smaller r.f. field, these two motions can be superimposed on the equation of motion for an ensemble of free spins yielding

$$\frac{d\vec{M}}{dt} = -\gamma(\vec{M} \times \vec{H}) - \frac{M_x\mathbf{i} + M_y\mathbf{j}}{T_2} - \frac{M_z - M_o}{T_1}\mathbf{k} \tag{2.30}$$

where $\mathbf{i}, \mathbf{j}, \mathbf{k}$ are unit vectors in the laboratory frame of reference. It can then be shown using these equations[52] that an additional constraint must be imposed on the flipping procedure in order for it to remain adiabatic. This condition is simply that the flip be performed sufficiently quickly that there is no appreciable spin relaxation during this time. The full adiabatic fast passage requirement can then be summarized

$$\frac{1}{T_2} \ll \frac{1}{H_1}\left|\frac{dH_o}{dt}\right| \ll |\gamma H_1| \tag{2.31}$$

since in practice T_2 is usually smaller than T_1.

As the spin is being rotated (the resonance is approached) the magnetization component along the x axis increases until resonance is reached at which point it is approximately equal to the original component in the z direction. In the lab frame the magnetization is then rotating at an angular velocity ω=2π(100 KHz) which will create a changing magnetic flux in an appropriately oriented coil. The voltage induced in this coil will be proportional to the size of the magnetic moment (polarization). This is the basic principle behind the AFP measurement technique.

The AFP setup is displayed in Fig. 2.4. The vertical holding field is provided by the large diameter Helmholtz coils. During an AFP scan the ramping of the D. C. field is controlled by the triangle wave generator which ensures that dH_o/dt is constant throughout the scan. The frequency of the triangular wave is $\sim$ .1 Hz and

a typical NMR scan takes about 10 seconds. The r.f. driving field is provided by a smaller set of coils oriented as shown and powered by a Hewlett Packard function generator. A third coil oriented perpendicularly to the first two sets detects the rotating ^{3}He or proton magnetic moment during passage through resonance. This signal is amplified and fed into an SRS lock-in amplifier. Since the drive coils and the "pick-up" coil are not exactly at 90 degrees with respect to each other, there is a small voltage induced in the pick-up coil by the drive field itself. This signal is compensated using the output from a second channel (labelled "comp") of the function generator. The "sync" output of the function generator is used to provide a phase reference for the Lock-in amplifier. This phase setting determines the phase of the sinusoid at which the SRS actually samples the NMR signal. The true NMR signal is obtained by subtracting the compensation signal (B) from the pick-up coil signal (A).

Calibration of the AFP Signal

Instead of trying to determine the magnitude of the ^{3}He polarization directly from the ^{3}He AFP signal, which requires accurate knowledge of the pickup coil circuit, we instead calibrate the ^{3}He signal by comparing it to a proton AFP signal from a similarly sized sample of water. Since it is critical that the parameters of the measurement circuit do not change between the ^{3}He and the water measurements, they are both performed at the same frequency of r.f. driver field, 100 KHz. The polarization of protons in a magnetic field whose Larmor frequency is 100 KHz ($\sim$ 24 gauss) as a function of temperature is given by the equation

$$P_p = n_p^+ - n_p^- = \frac{e^{\beta\mu H} - e^{-\beta\mu H}}{e^{\beta\mu H} + e^{-\beta\mu H}} = tanh(\beta\mu H) \approx \beta\mu H \qquad (2.32)$$

[54] where $n_p^{\pm}$ is the occupation number of the spin $\pm$ state and $\beta = (k_B T)^{-1}$. At room temperature $\sim 298K$ the equilibrium value of the polarization is 8.2x10^{-9}. If the voltage induced in the pickup coil by the water sample is V_{H_2O} and that of the

Table 2.2: Light Absorption Parameters for Rb D1 Line

^{3}He press. (atm.)	x (cm)	$\nu_o(p) - \nu_o(0)$ (GHz)	Γ (GHz)	Γ_a (GHz)	b (10^{-12} s)	$\Gamma_{SD}/[Rb]$ (10^{-12} cm^{3}s^{-1})
2.94	1.68	14.3 ± 1.9	54 ± 3	154 ± 11	0.20 ± 0.04	0.93 ± 0.08
6.44	1.68	34.7 ± 4.8	126 ± 5	146 ± 11	1.0 ± 0.2	1.37 ± 0.12
8.97	1.68	53.7 ± 3.8	184 ± 6	184 ± 11	1.5 ± 0.2	2.02 ± 0.17
12.1	2.00	73.2 ± 1.9	244 ± 7	225 ± 12	1.5 ± 0.2	2.82 ± 0.24

^{3}He sample is $V_{^3He}$ then the ^{3}He polarization is given by

$$P(^3He) = \frac{1}{P_p}\frac{V_3}{V_{H_2O}}\frac{\rho_p}{\rho_3}\frac{\mu_p}{\mu_3} \tag{2.33}$$

for the case where the two samples have the same cross sectional area. ρ_p and ρ_3 are the proton and ^{3}He densities with μ_p and μ_3 being the corresponding magnetic moments.

2.3 Results

2.3.1 Transmission Data and Average Rb Polarization

Transmission scans performed with linearly polarized (σ_o) light at temperatures near 393 K and 452 K are shown in Fig. 2.5. At T= 393 K the Rb number density, $[Rb]$, is sufficiently low that the transmitted intensity is measurable even on resonance. The data were fitted with the expression 2.2. From these scans the pressure shifts, pressure broadened widths, and asymmetry parameters were obtained for each of the four cells.

The fits to the data shown in Fig. 2.5 were obtained with parameters Γ, Γ_a and b given in Table 2.2 and with Rb number densities calculated from the vapour pressure formula of Killian[55]

$$log_{10}[Rb] = 26.41 - 4132/T - log_{10}T\ . \tag{2.34}$$

When $[Rb]$ is fitted as a free parameter, the values obtained agree with the calculated ones to better than 10%. The pressure shifts for the Rb D1 line are shown in Fig. 2.6 (top panel) together with an empirical fit, $\nu_o(p) - \nu_o(0) = (4.8\ p\ +\ 0.106\ p^2)$ GHz. Our values are systematically lower than the shifts measured for ^{4}He gas in earlier work by Ch'en[56]. This is to be expected since the shifts, in general, decrease with decreasing molecular weight[57]. The line width Γ (see Fig. 2.6, bottom panel) is found to increase linearly with ^{3}He pressure, i.e. $\Gamma = 20.0 \times p$ GHz. This implies that the absorption length, $\kappa_{\nu_o}^{-1}(p) \approx 88\ p\ \ \mu$m, on resonance and for $[Rb] = 4 \times 10^{14}$ atoms/cm^3, increases linearly with pressure. Our results are in approximate agreement with the measurements of Ch'en[56]. The linewidth does not seem to depend on molecular weight so our ^{3}He results should be directly comparable to the ^{4}He results of Ch'en.

Transmission scans performed with circularly polarized light are displayed in Fig. 2.7. The solid curves represent fits to the data with the use of equations (2.5) – (2.11) to calculate the transmitted light intensity and the average Rb polarization. The frequency dependence of the absorption cross section is given by equation (2.2) where the asymmetry parameters, pressure shifts and widths are determined from the fits to the data obtained with linearly polarized light. The lineshape data obtained with circularly polarized light display a pronounced absorption spike near $\nu_0(p)$ which may be caused by the presence of unpolarized Rb at the glass surface. The effective thickness of the layer of unpolarized Rb, ℓ, is given approximately by $\ell = \sqrt{D/(\gamma_\nu^+ + \Gamma_{SD})}$ (see equation 2.11) where D is the effective diffusion constant for Rb in ^{3}He gas. We have fitted D with our one-dimensional model assuming that D varies inversely with ^{3}He pressure, i.e. $D = D_o/p$. We find that a fixed value $D_o = 3.5$ cm^{2}s^{-1} gives acceptable fits for the range of pressures and light intensities used in our work. It should be noted that the fitted value is larger by about a factor of 6 than that quoted by Bernheim[58] for ^{4}He and Rb. The source of this discrepancy is unclear and may arise from the simplifying assumptions made

in describing the physics of Rb depolarization near the cell wall or from the neglect of bulk effects, e.g. scattered flourescent light ($\approx$ 2% of the incident light) which is expected to be unpolarized. We have shown previously[59] that an elliptical polarization component of the light cannot produce such a sharp absorption spike and, furthermore, the ellipticity of the incident light was measured to be less than 5%. The necessity to include diffusion in equation 2.5 is less compelling at higher pressures which is expected because of decreased diffusion at higher pressure.

Apart from the diffusion constant D_o, the spin destruction rate Γ_{SD} is the only adjustable parameter needed to describe the transmission data. The fitted spin destruction rates per Rb number density, $\Gamma_{SD}/[Rb]$ in Table 2.2, include the effect of unpolarized layers at the cell walls described by equation 2.11. The dependence of the ratio $\Gamma_{SD}/[Rb]$ on ^{3}He pressure is shown in Fig. 2.8 (top panel) together with an unpublished value determined by Knize and Happer[60] who used the time-dependent method. We assume that the spin destruction rate can be described by

$$\Gamma_{SD} = < \sigma_{SD} v > \ [Rb] + \ < \sigma_{SE}\ v > \ [^3He] \ + \ k\ [^3He]^2 \ . \qquad (2.35)$$

Spin destruction due to the presence of N_2 gas is ignored because the N_2 pressure is low (120 Torr) and constant. Fitting the data using the ^{3}He relative density p in place of the number density we obtain

$$\Gamma_{SD} = (325.0 + 1.64\ p + 5.44\ p^2)\ \mathrm{s}^{-1} \qquad (2.36)$$

at $[Rb] = 4 \times 10^{14}$ cm^{-3}. The constant term probably arises from spin destruction during Rb-Rb collisions as has been assumed previously (see ref. [17]). We have confirmed this by additional measurements shown in Fig. 2.8 (bottom panel) in which [Rb] was varied at a ^{3}He buffer gas pressure $p = 12.1$ atmospheres. The data have been fitted with the expression $\Gamma_{SD} = a \times [Rb] + b$. The parameter a represents the velocity averaged rate constant for spin destruction in Rb–Rb collisions. We find that this value is $(8.3 \pm 0.6) \times 10^{-13}$ cm^{3}s^{-1} in good agreement with earlier

measurements by Knize and Happer[60] at lower ^{3}He densities. The parameter b represents Rb spin destruction induced by ^{3}He and N_2.

The linear term in equations 2.35 and 2.36 represents mainly Rb spin relaxation due to spin exchange with ^{3}He nuclei. The multiplier is calculated using the measured Rb–^{3}He spin exchange rate (see below). At high ^{3}He densities the spin destruction rate per Rb atom due to Rb–^{3}He spin exchange becomes significant but not large. The Rb–Rb and the Rb–^{3}He spin destruction rates are shown as the dashed lines in the top panel of Fig. 2.8.

The quadratic term in equations 2.35 and 2.36 might indicate polarization losses initiated by 3–body collisions of a Rb atom with two ^{3}He atoms. For heavier noble gases (Ar, Kr, Xe) at low pressures ($\approx 1 - 100$ Torr) such collisions have been shown[15,16,61] to result in the formation of van der Waals molecules, with the third collision partner required to carry away the binding energy of the molecule. Destruction of the Rb spin in the molecule is caused by the spin-rotation interaction between the electron spin of the Rb and the rotational angular momentum of the molecule, as was first shown by Bernheim[58]. The molecular formation rate, $T_F^{-1} = \delta \times p^2$, is expected to be proportional to the square of the noble gas pressure, where δ is some constant. However, the spin destruction rate is expected[15][16] to level off at high pressure as

$$\Gamma_{SD}^{mol} = \delta \, \frac{2}{3} \, \frac{p^2}{1 + (p/p_o)^2} \tag{2.37}$$

where p_o is a characteristic pressure (typically 10-100 Torr) at which the mean spin rotation angle is 1 radian. In previous work such molecules have typical lifetimes of 10^{-8} s, limited by the binary collision rate, thus allowing a large spin rotation angle. In the present work the very short time between binary collisions (1–10 ps) implies rapid breakup of any Rb-^{3}He molecules. In the absence of molecular formation we have no plausible explanation for spin rotation in Rb-^{3}He-^{3}He collisions.

Our success in quantitatively describing the transmission data of Figs. 2.4 and 2.6 implies that we obtain estimates of the average Rb polarization in the cell.

volume. As an example Fig. 2.9 shows P_{Rb} for a 2 cm long cell at $p = 3$ atmospheres, $[Rb] = 4\times10^{14}$ cm^{-3}, and four different laser powers. For the lowest laser power P_{Rb} exhibits a dip on resonance ($\nu_o(p)$) which is caused by enhanced light absorption represented by the diffusion term. At higher laser powers it is most efficient to pump at the resonance frequency. Modulation of the laser frequency, a method commonly used in laser spectroscopy to overcome 'hole-burning', is not applicable in the high-pressure regime. The high frequency of Rb–^{3}He collisions, estimated to be $\tau_{coll}^{-1} \approx 1.9\ p\ \times 10^{10}$ Hz, ensures that the absorption profile is fully re-established in the time interval between absorption of subsequent photons.

Finally we discuss the question of laser power required to optically pump Rb at various ^{3}He pressures. The strong increase of the spin destruction rate versus p makes it unfavorable to optically pump Rb at high pressures. We have calculated the laser power required at the resonance frequency $\nu_o(p)$ to pump a typical number density $[Rb] = 4 \times 10^{14}$ cm^{-3} to an average polarization of 96%. The calculations include the effects of the enhanced light absorption represented by the diffusion term. Results for various cell thicknesses x (in cm) are shown in Fig. 2.10 together with an empirical fit

$$I(\nu_o(p)) = (\ 39.6 + 0.551\ (p-3)\ p\ )\ \left(\ x\ + 0.27\ \frac{p}{x^{1/2}}\right)\ \text{mW cm}^{-2}\ . \qquad (2.38)$$

This estimate, which is supported by our transmission results for $x = 1.68$ cm and 2.0 cm, and for $p = 3$–12 atmospheres, has to be considered a *lower limit* because additional power is required in practice to compensate for nonuniformity of irradiation, frequency detuning, and losses incurred in the expansion and transport of the laser beam.

2.3.2 Rb–^{3}He Spin Exchange Measurements and ^{3}He Polarization

The rate of Rb–^{3}He spin exchange has been determined from the decay of the ^{3}He polarization following laser irradiation for at least 12 hours. For each cell the

Table 2.3: Characteristic Rb – ^{3}He Spin Exchange Times γ_{SE}^{-1} for $[Rb] = 4 \times 10^{14}$ cm^{-3} and Wall Relaxation Times Γ_w^{-1}

^{3}He pressure (atm.)	γ_{SE}^{-1} (hr)	Γ_w^{-1} (hr)
2.94	10.8 ± 0.5	28.4 ± 0.3
6.44	10.6 ± 0.5	46.0 ± 2.2
7.03	9.8 ± 0.5	63.5 ± 7.6
8.97	10.7 ± 0.5	48.6 ± 1.5
12.1	11.1 ± 0.6	25.0 ± 0.3

polarization decay measurements were repeated at various cell temperatures, from T≈ 453 K ($[Rb]\sim 4.3\times10^{14}$cm^{-3}) to room temperature (293 K). A typical set of decay measurements is presented in Fig. 2.11. The relative polarization is the AFP NMR signal normalized to the value at the start of the decay measurement. The ^{3}He pressure in this cell was $p = 8.97$ atmospheres.

Values for γ_{SE} are shown in Table 2.3 for five cells containing ^{3}He densities $p = 3$–12 atmospheres. They are fitted well with a constant value for the velocity averaged spin exchange cross section, $< \sigma_{SE} v > = (6.1\pm0.2) \times10^{-20}$ cm^{3}s^{-1} corresponding to a decay rate of (10.6 hr)$^{-1}$ at T = 453 K. This value is almost a factor of two smaller than that of Chupp *et al.*[17]. We note that extraction of $< \sigma_{SE} v >$ from the data requires an accurate knowledge of the Rb number density. As already mentioned in section 2.2 we have paid special attention to the hot air flow around our cells to keep temperature gradients to typically ± 1.5 K. Furthermore, we have obtained good consistency of $[Rb]$ deduced from the transmission data (see Fig. 2.5) with those calculated by Killian's formula[55]. The cell wall relaxation rates, also shown in Table 2.3, were determined at room temperature. A possible temperature dependence of Γ_w would modify the values of γ_{SE} extracted from the total decay rate, $(\gamma_{SE} + \Gamma_w)$, although the systematic error in γ_{SE} is likely to be small since the

condition $\gamma_{SE} \gg \Gamma_w$ was generally fulfilled. Typical wall relaxation rates of cells used for in-beam experiments at TRIUMF are $\sim$ (50 hr)$^{-1}$.

From equation 2.15, the maximum ^{3}He polarization obtainable with $P_{Rb} \approx 1$,

$$\tilde{P}_{max} = \frac{\gamma_{SE}}{\gamma_{SE} + \Gamma_w} \tag{2.39}$$

is then $\approx$0.83. Using 8–9 Watts of laser light on cells of 17 cm^3 volume we have observed polarizations of 0.79 at $p = 6.44$ atmospheres (calculated $\tilde{P}_{max} = 0.86$), and 0.73 at $p = 8.97$ atmospheres (calculated $\tilde{P}_{max} = 0.82$). The difference between observed and calculated polarizations can probably be attributed to partial shadowing of the incident laser beam (VESPEL fingers used to hold the glass, solid Rb droplets on the glass walls), and to diffraction effects of the incident light on the curved glass walls. With a cell of larger volume (35 cm^3) and at $p = 10.5$ atmospheres we have observed ^{3}He polarizations of $\approx$ 0.65. We attribute this considerably smaller value to the difficulty of expanding the laser light uniformly over a large rectangular area (3 cm $\times$ 8.5 cm).

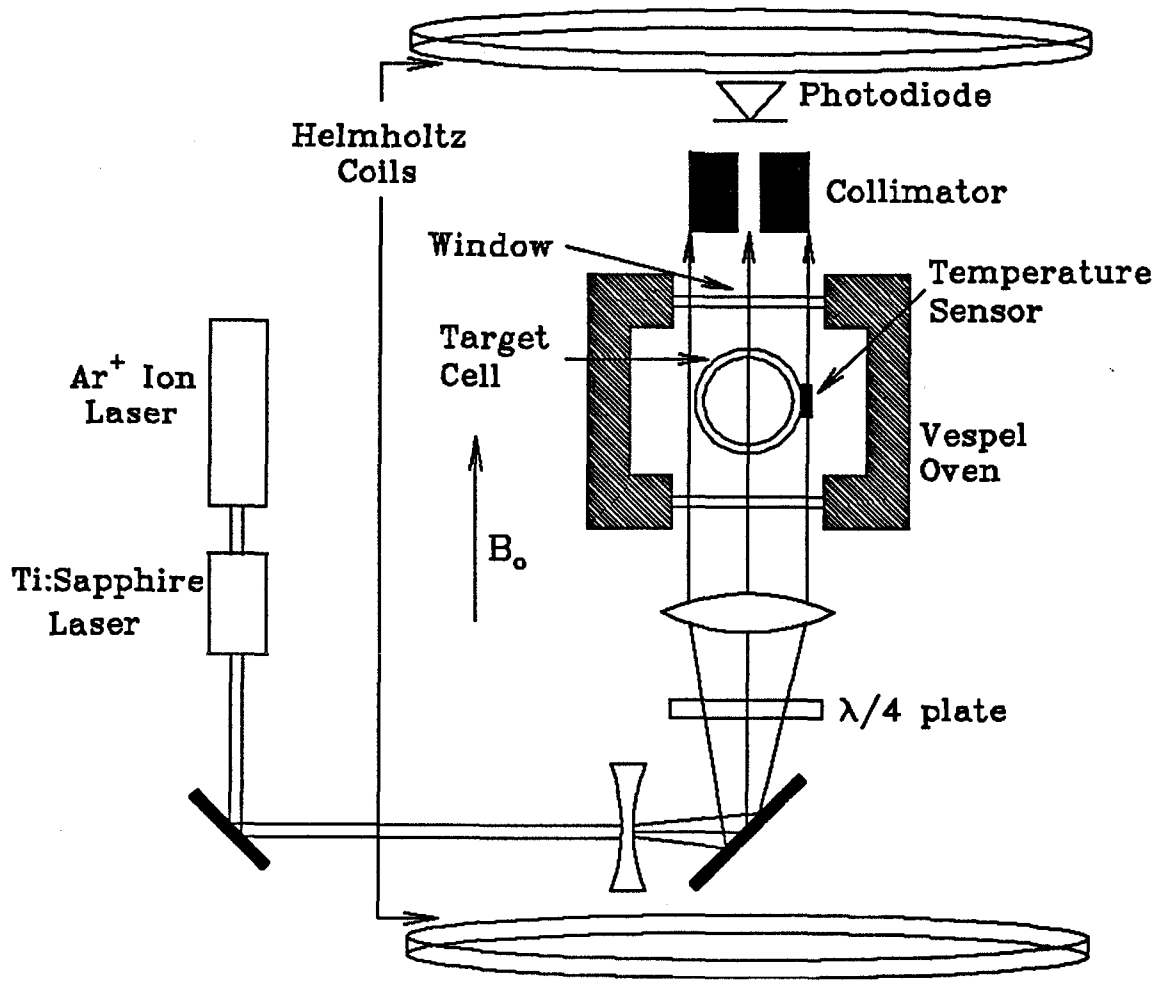

Figure 2.3: Experimental setup for measurements of light transmission through ^{3}He target cells.

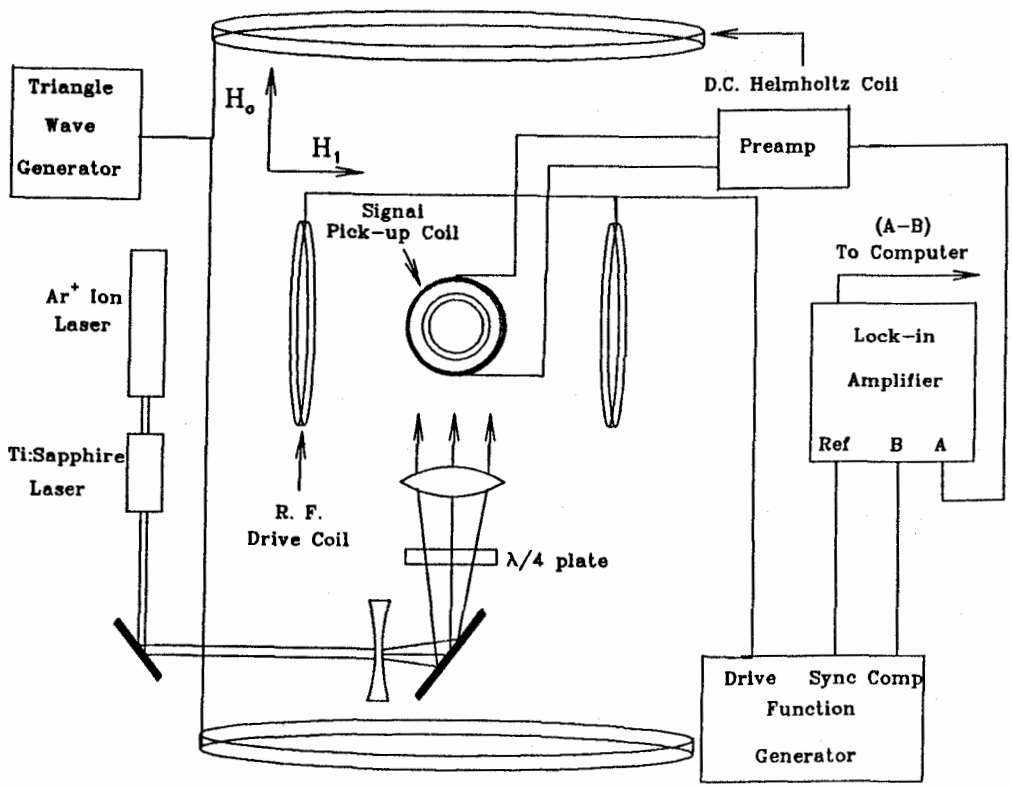

Figure 2.4: Experimental setup for AFP measurements of the ^{3}He polarization

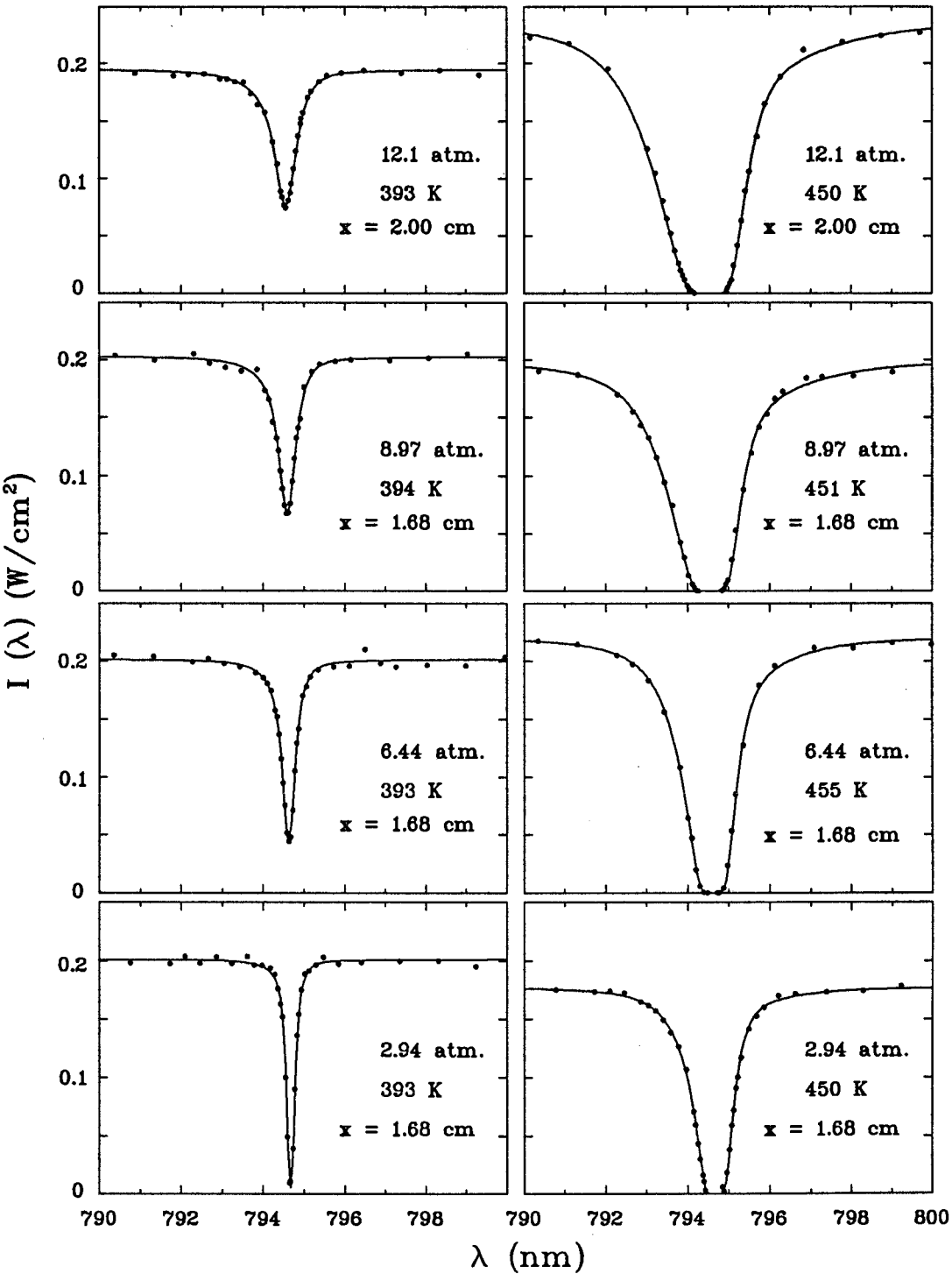

Figure 2.5: Transmission of linearly polarized light through different cells at temperatures near 393 K (left) and 450 K (right). The solid curves are fits with Γ, Γ_a and b from Table 2.2.

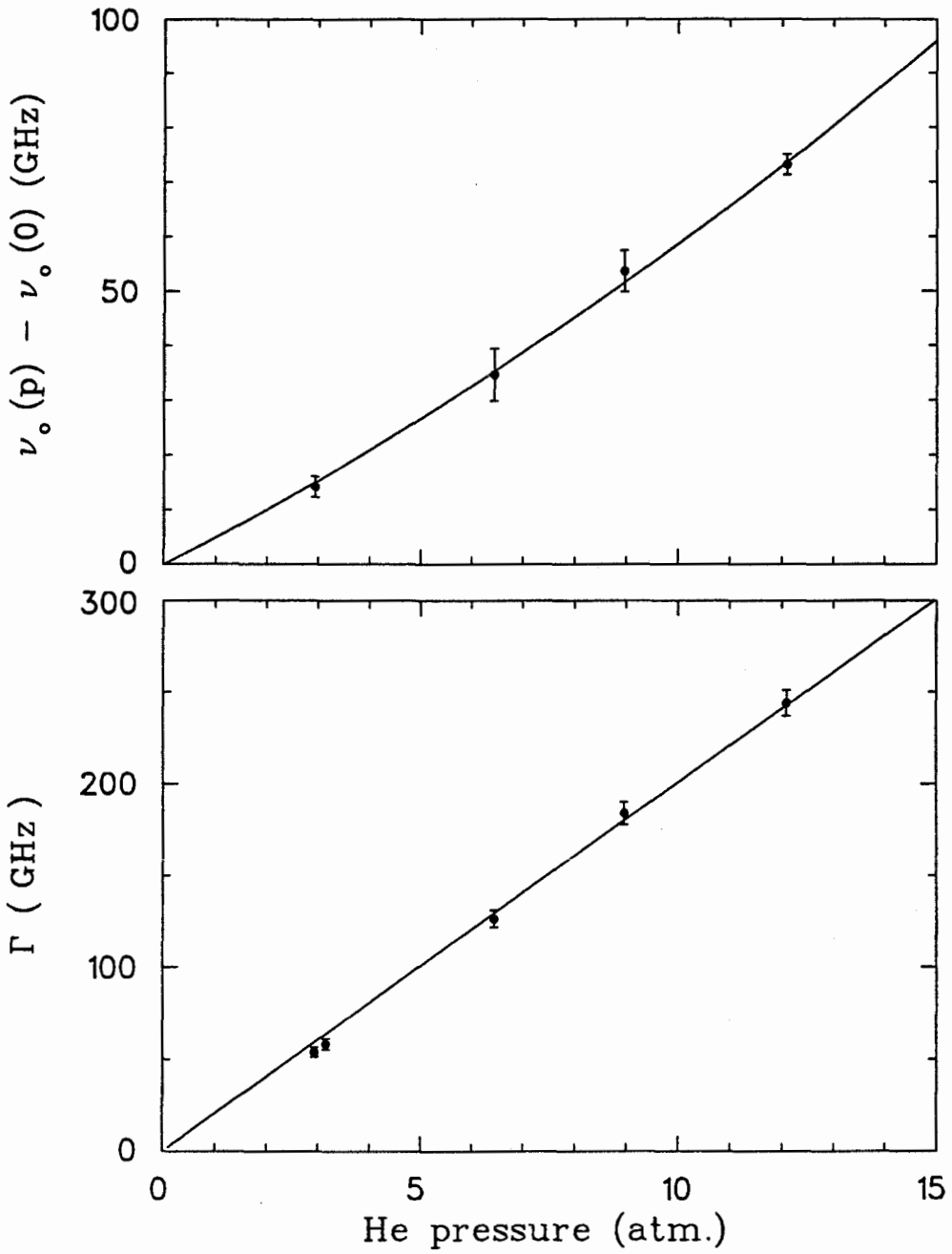

Figure 2.6: Pressure shift of the Rb D1 line (top), and pressure broadening of the D1 line width Γ (bottom).

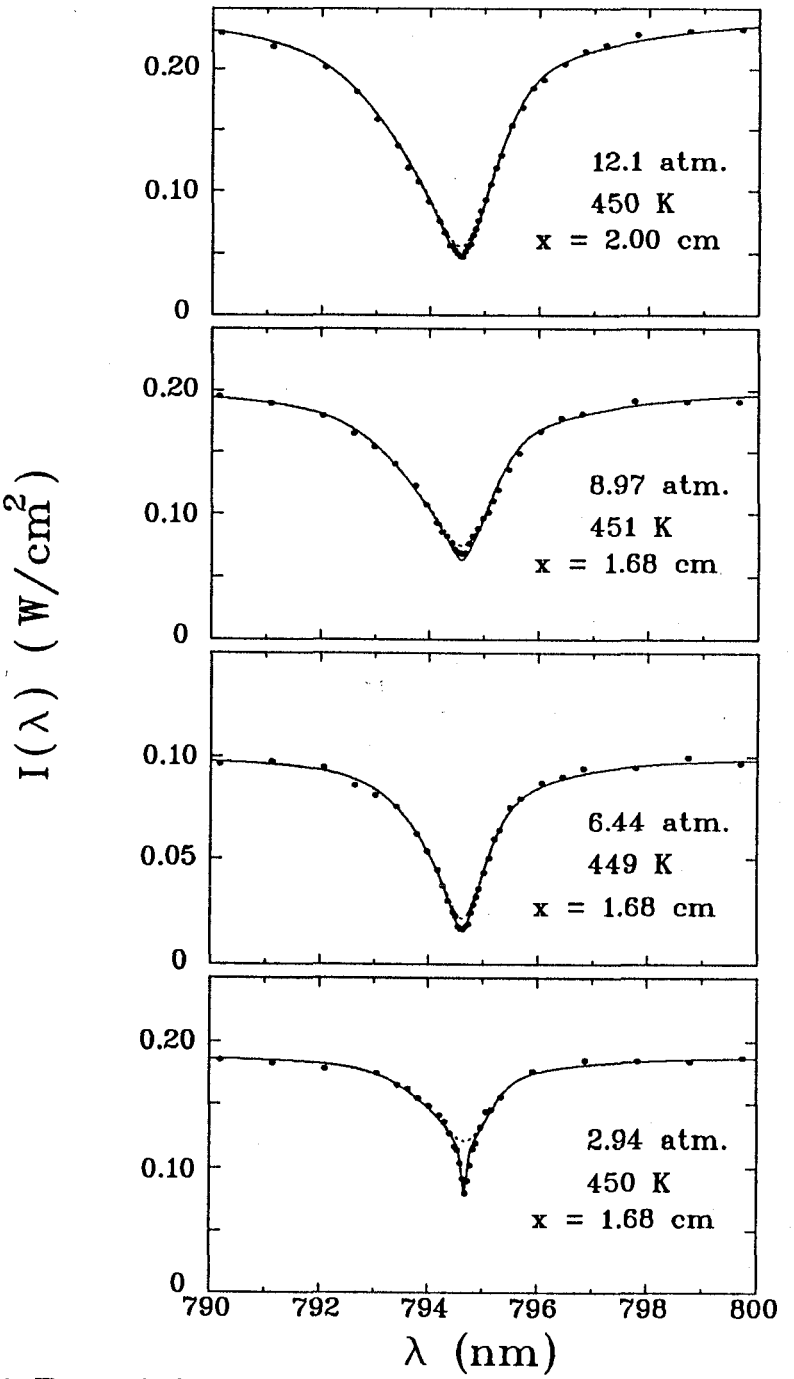

Figure 2.7: Transmission scans at T≈450 K for circularly polarized light. The solid curves include a ≈40 μm thick unpolarized Rb layer at the glass surface, whereas the dotted curves were calculated without such a layer. The calculations use spin destruction parameters shown in Table 2.2.

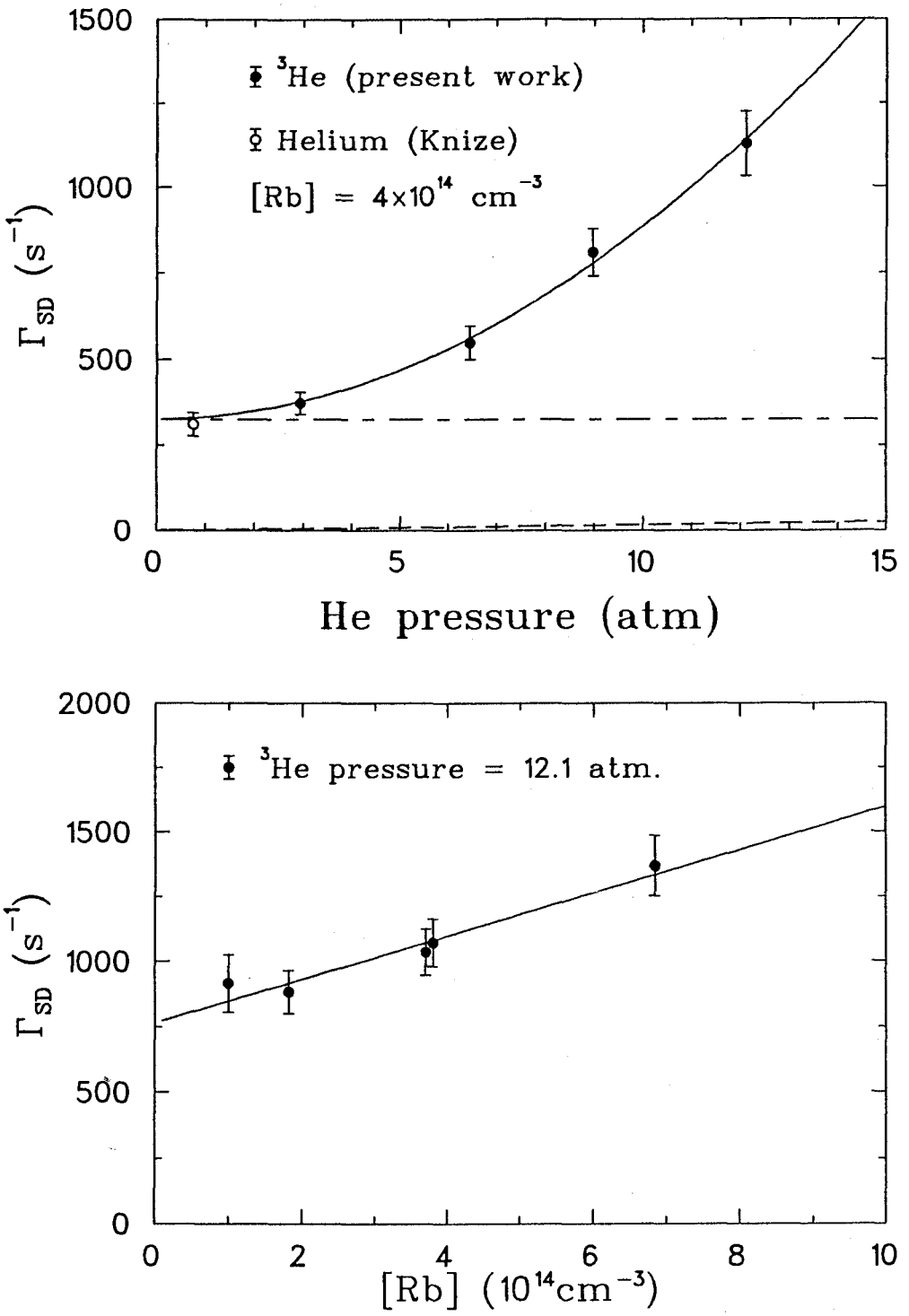

Figure 2.8: The dependence of Γ_{SD} on ^{3}He pressure (top panel). The solid curve represents the total measured spin destruction rate, the dot-dashed curve is the constant Rb–Rb contribution and the dashed curve is the contribution from spin exchange between Rb and ^{3}He. The dependence of Γ_{SD} on Rb density is shown below.

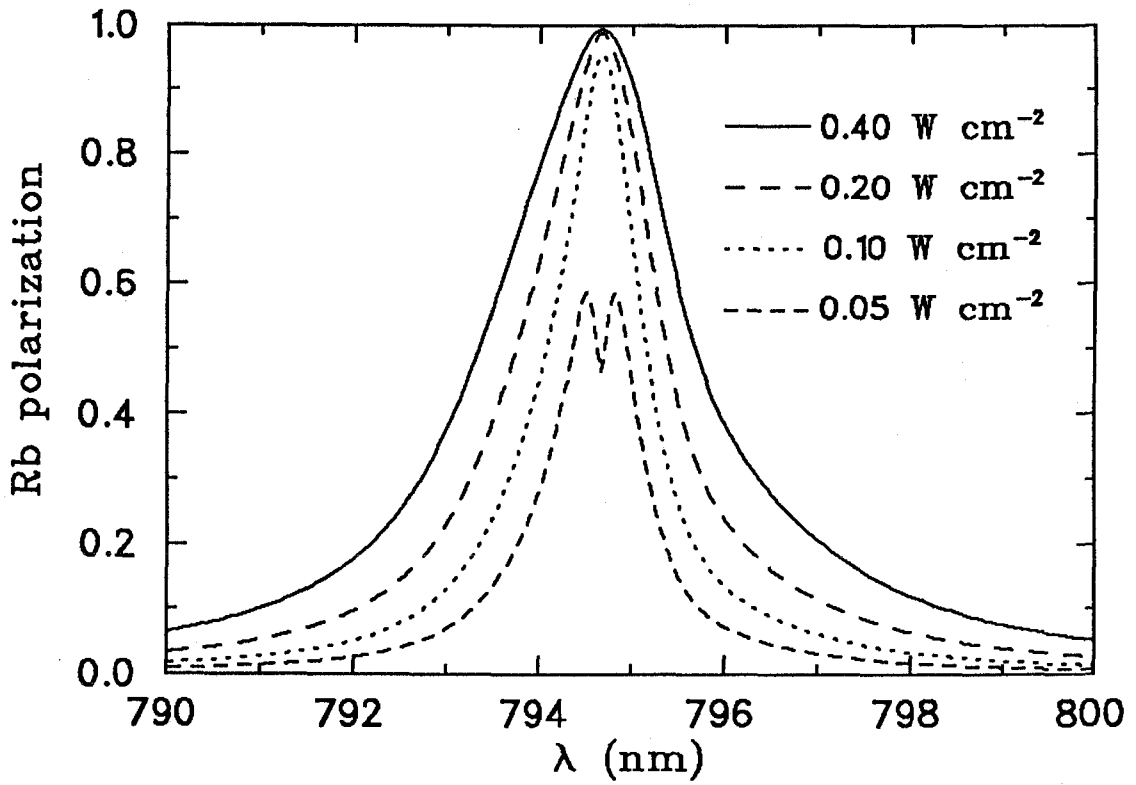

Figure 2.9: Rb polarization in a 2 cm long cell predicted for various light intensities. The Rb density was assumed to be 4×10^{14} cm^{-3}.

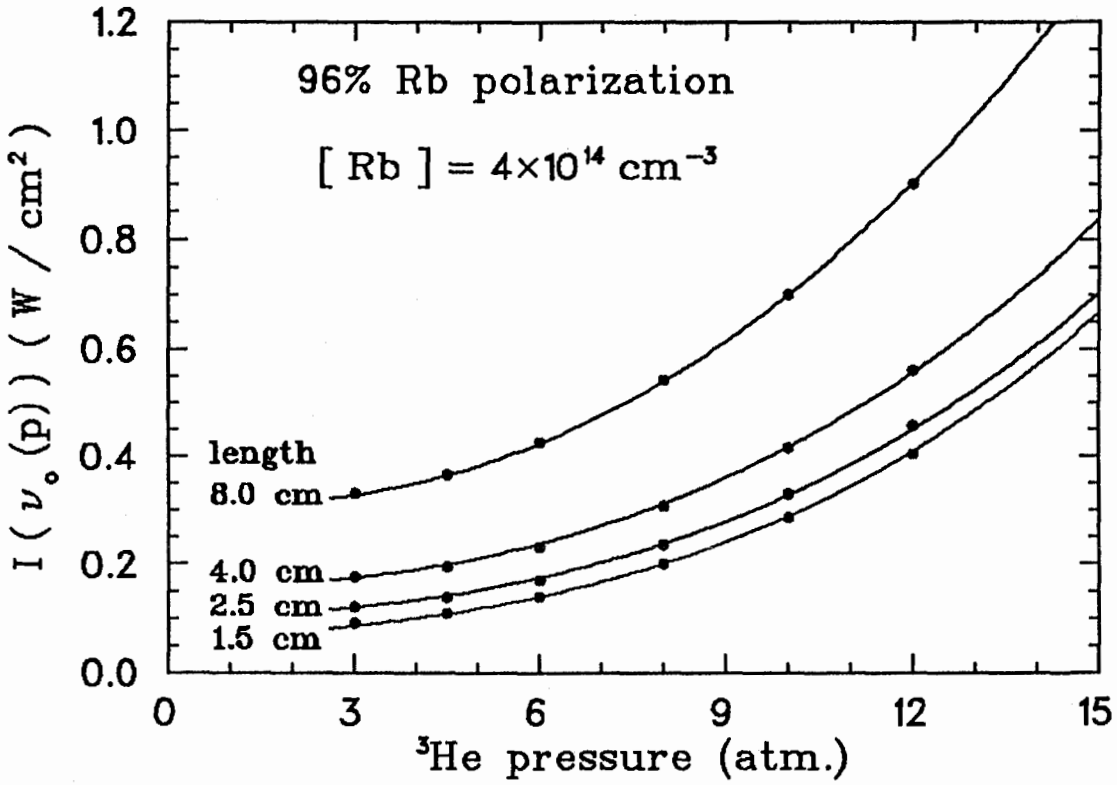

Figure 2.10: Calculations of the laser power required to obtain 96% average Rb polarization in cells of various thicknesses. The curves represent an empirical fit described in the text.

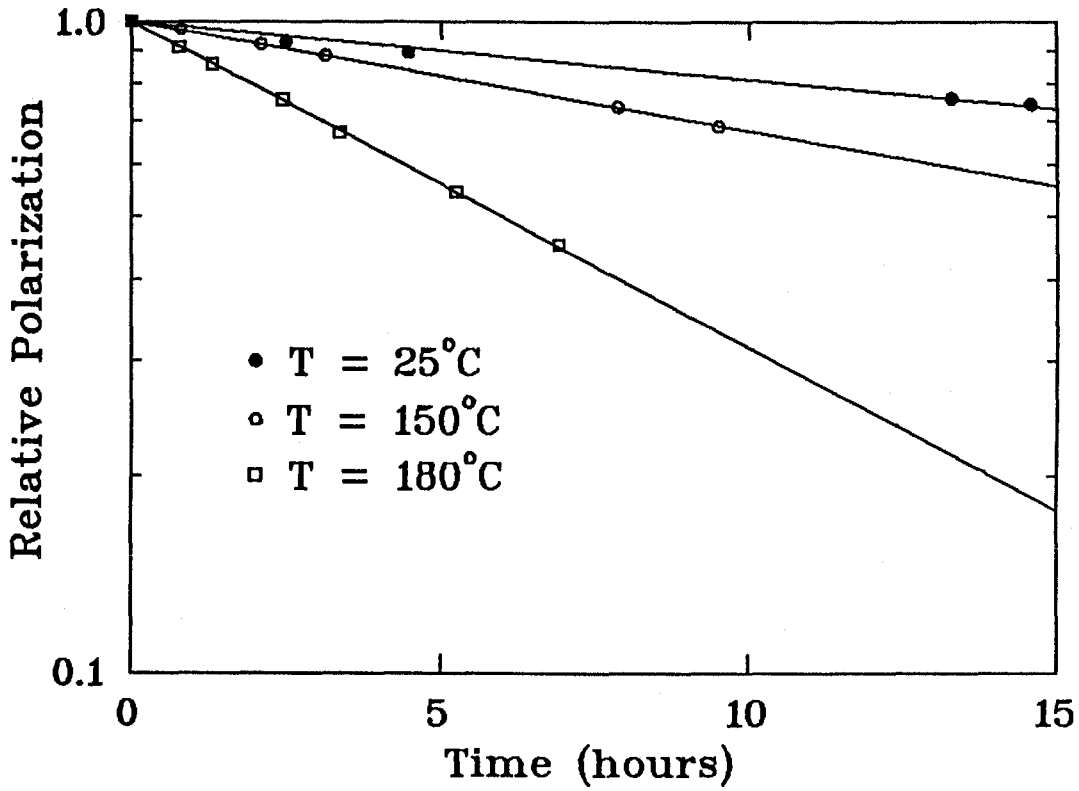

Figure 2.11: Polarization decay curves for ^{3}He in the presence of various amounts of unpolarized Rb vapour.

Chapter 3

Elastic Scattering of Polarized Protons from $^3\vec{\mathrm{H}}\mathrm{e}$

3.1 The Experiment

There are three basic components involved in the measurements described in this chapter. The first is the polarized ^{3}He target which was the subject of chapter 2. The second is the production and measurement of the polarized proton beam. The third is the MRS spectrometer system which is used to analyse the momentum of the scattered protons and provide trace back to the target.

3.1.1 The Polarized Proton Beam

The first element of the TRIUMF I2 ion source is a duoplasmatron which is the source of H^+ ions. The H^+ ions are extracted from the duoplasmatron and accelerated up to an energy of 500 eV using an electrostatic accelerating lens. The H^+ beam then enters a cesium charge exchange cell where about 30% of the ions acquire an electron which populates the $2S_{1/2}$ metastable state. The rest of the ions pick up either an electron which falls into the ground state, two electrons creating H^- ions or they remain positively charged. A small electric field is used to remove the charged species from the sample.

Following the cesium cell, the neutral beam enters a SONA cavity which utilizes the Lamb Shift to produce the actual polarized beam. The Lamb Shift is the

splitting of the hydrogen $2S_{1/2}$ and $2P_{1/2}$ states which is predicted only by relativistic quantum mechanics. Due to relativistic effects the $2S_{1/2}$ level is higher in energy than the $2P_{1/2}$ level by an amount corresponding to a frequency of 1.059 GHz. The SONA cavity contains an axial magnetic field which starts at 0 ($z = 0$) and increases to 575 gauss at $z = a$. At this field the two hyperfine states in which the electron polarization is opposite to the field direction become degenerate with the $2P_{1/2}$ states. This is illustrated in Fig. 3.1.

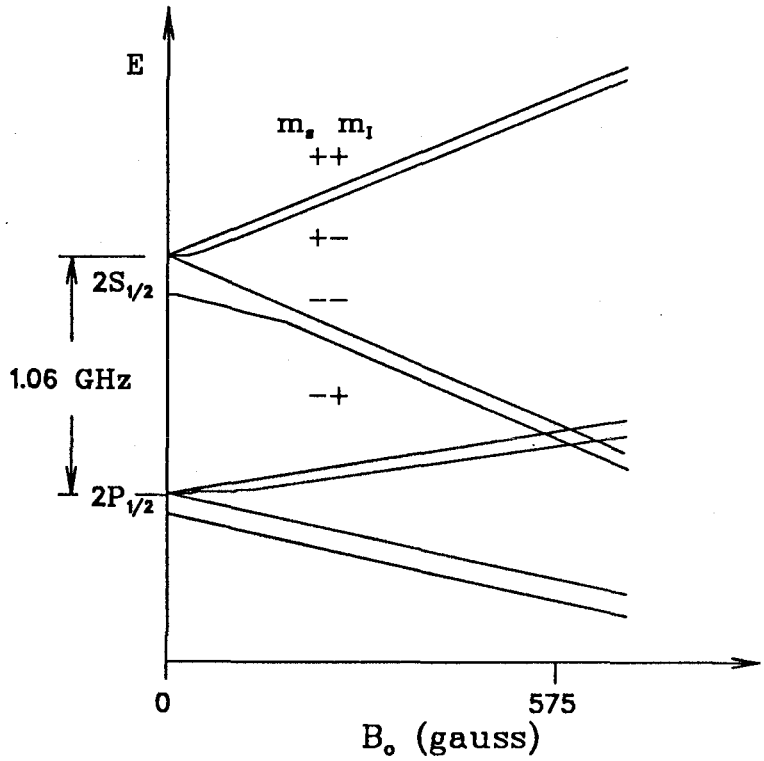

Figure 3.1: The hyperfine structure of the $H(2S_{1/2})$ and $H(2P_{1/2})$ levels.

The application of a small d.c. electric field mixes these $2S_{1/2}$ substates with the $2P_{1/2}$ states (this is the Stark effect) allowing them to decay rapidly to the ground

state.

At this point ($z = a$) the metastable sample contains only two components of the hyperfine multiplet which are electronically polarized along the direction of the field but have opposite nuclear spin orientations. After the point $z = a$, the magnetic field in the cavity decreases as a function of z eventually crossing zero and reversing. The zero crossing causes the electron spin of the $m_F = 0$ hyperfine component to reverse its polarization while having no effect on the $m_F = 1$ component. m_F refers to the z projection of the total spin $F = I + S$ where I is the proton spin and S is the electron spin. Since there is no transfer of angular momentum, the z component of the nuclear spin in the $m_F = 0$ component must also change sign. The sample now contains polarized nuclei and unpolarized electrons. This technique is called diabatic field reversal in contrast to the adiabatic spin reversal technique used in NMR measurements. Reversal of the magnetic fields in all solenoids of the ion source reverses the polarization of the beam. In a typical mode of operation the spin is reversed every 3 minutes.

The sample which contains only ground state atoms and nuclear polarized metastable atoms is passed through an argon cell which acts as a preferential electron donor for the metastable atoms. A certain percentage of ground state atoms will also gain an electron thus limiting the maximum polarization attainable with such a source. The resulting beam of polarized H^- ions have their nuclear spins aligned (or anti-aligned) with the beam momentum. The nuclear polarization is subsequently precessed into the vertical direction (normal polarization) before injection into the cyclotron. The beam polarization is then aligned with the vertical magnetic field of the cyclotron thus minimizing any polarization loss during acceleration.

The resulting polarized H^- beam is accelerated in the TRIUMF cyclotron up to a maximum energy of 515 MeV. The proton beam is created when the H^- ions pass through a carbon foil, stripping the two electrons from the proton. The positively

charged protons are no longer constrained by the magnetic field and are deflected out of the cyclotron. The energy of the incident beam is determined by the radial distance of the carbon foil from the center of the cyclotron. The beam is delivered to the interaction point by beamline 4B (BL4B). A description of the beamline can be found in ref. [62]. The main beamline elements are displayed in Fig. 3.2. A

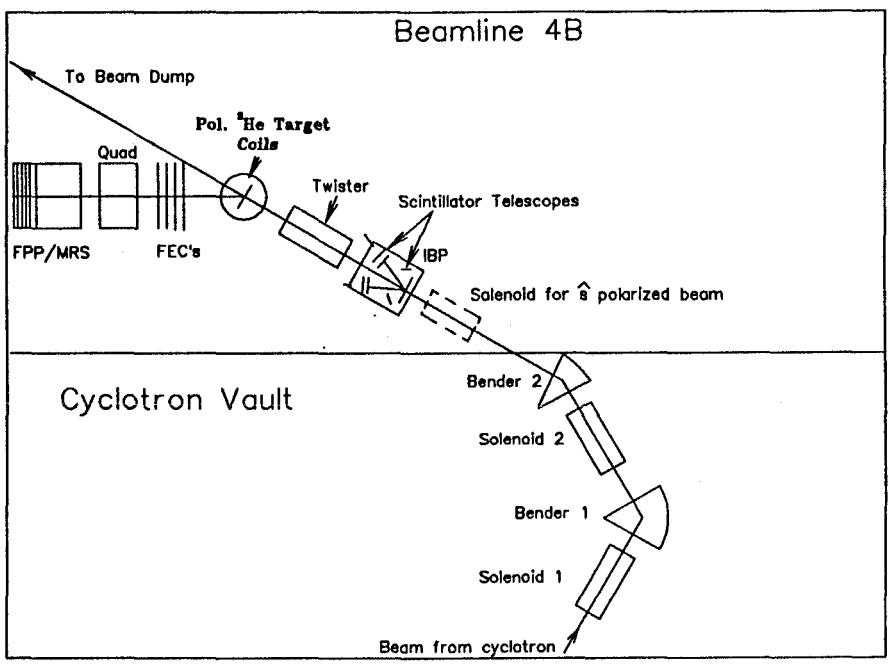

Figure 3.2: Schematic view of the experimental layout including beamline 4B.

crucial element of BL4B is the In Beam Polarimeter (IBP)[63]. The IBP provides the measurement of the transverse polarization components of the incident beam

polarization ($\hat{\mathbf{n}}$ and $\hat{\mathbf{s}}$). Only $\hat{\mathbf{n}}$ type beam was used during this phase of the experiment. The IBP consists of a thin CH_2 target and four scintillator telescopes; one on either side and above and below the CH_2 target. The telescopes measure the number of protons scattered to the left (N_{left}), to the right (N_{right}), to the top (N_{top}) and to the bottom (N_{bot}) at a 17° lab angle in coincidence with the corresponding recoil proton scattered to the opposite side of the beam at a large angle. Accidental coincidences are determined and subtracted from N_{left} etc. to obtain the true number of scattered protons. The analyzing power of CH_2 is large at this angle but varies with energy from 0.28 at 200 MeV to 0.47 at 500 MeV. The beam polarization is then determined from the expression

$$P = \epsilon / A_y$$

where

$$\epsilon = \frac{N_{left} - N_{right}}{N_{left} + N_{right}}$$

is the measured asymmetry in the horizontal plane. Hence P, defined in this way is the the normal component of the beam polarization.

The IBP has been calibrated against a Faraday cup and serves as an accurate beam current monitor. At 400 MeV for instance, the beam current can be calculated from the following expression

$$I_{beam}(nA) = (59.49 * T_{IBP})^{-1} * (N_{left} + N_{right})/t$$

where 59.49 is determined empirically, T_{IBP} is the polarimeter target thickness in mg/cm^2 and t is the length of time over which IBP counts are collected. We also use the IBP signal in coincidence with a pulse generator signal to provide random pulser events in proportion to the beam current. We then use the number of pulser events processed divided by the total number of pulser events as the value for the computer and electronics deadtime.

3.1.2 The Medium Resolution Spectrometer

The Medium Resolution Spectrometer (MRS) is depicted schematically in Fig. 3.3. The MRS consists of a quadrupole and dipole magnet combination. The dipole

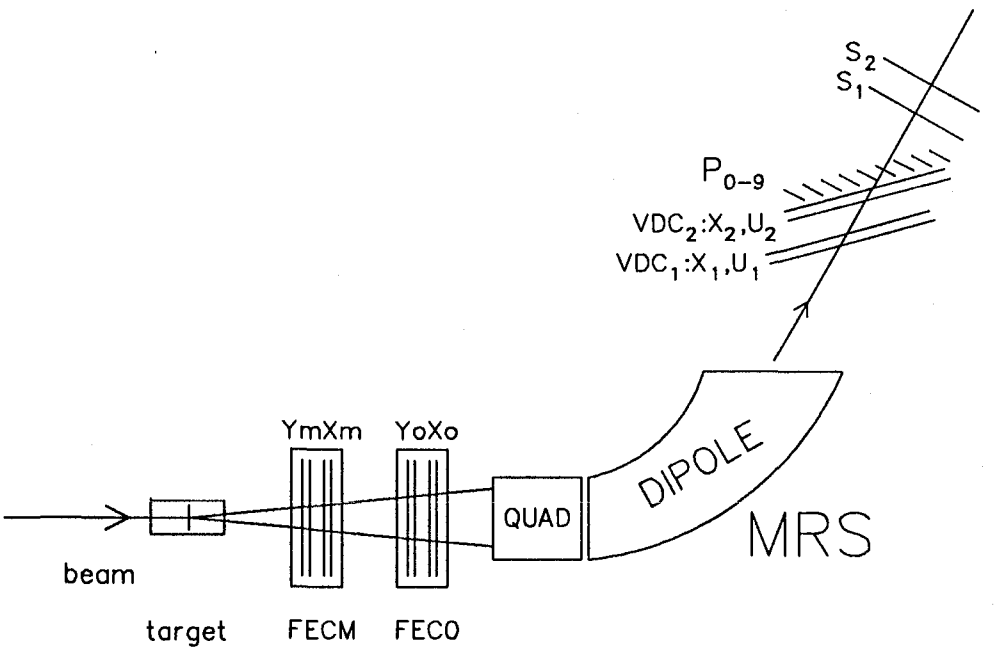

Figure 3.3: The Medium Resolution Spectrometer (MRS) system.

magnet has a central bend angle of 60° in the vertical direction and a momentum acceptance of $\Delta P/P \approx \pm$ 7% for particle momenta up to about 1.5 GeV/c. The total scattering angle range is $-12°$ to $+135°$. Two distinct modes of operation are needed to exploit the full angular range of the MRS. For angles less than 16° small

angle configuration or "SAC" is used and for angles larger than this, large angle configuration or "LAC" is used. The important differences between the two are: 1) the quadrupole position, 2) the distance from the target to the front end chambers (FEC's), and 3) the method of stopping the main beam. In LAC mode the main beam continues past the MRS and is stopped in a heavily shielded beam dump. At small angles the MRS platform crosses the beamline so the main beam dump cannot be used. Instead, the beam is stopped in a copper block which is immersed in a tank of borated water located on the MRS platform. Further details regarding the various features of a particular mode can be found in reference [64]. We used the LAC mode and the high-current shielded beam dump.

Ray tracing through the spectrometer is provided by two sets of drift chambers containing two orthogonal sets of two wire planes each located in front of the MRS quadrupole (FEC's) and two sets of vertical drift chambers (VDC's) with two wire planes each located just above the focal plane of the MRS. A schematic of the MRS spectrometer system is shown in fig. 3.3. The FEC coordinates are used to: 1) define the angular acceptance of the MRS, 2) correct for aberrations in the spectrometer and 3) provide traceback to the target to eliminate events which originated in the endcaps of the target cell. Each FEC plane consists of 16 alternating anode and cathode wire pairs spanning 8 cm. There are two wire planes in each direction labelled XM,XM′,YM and YM′ for the first chamber and X0, Y0 etc. for the second. The primed planes are offset from the unprimed planes by one half of an anode spacing to remove the "left - right" ambiguity. The position of the struck wire in the primed plane indicates whether the proton passed to the left or to the right of the struck wire in the unprimed plane. This arrangement also allows interpolation using drift times (with an accuracy of $\sim \pm 0.5$mm) that would otherwise not be possible. The FEC's may also constitute part of the MRS trigger. The trigger condition will be described later.

Each VDC chamber contains two crossed wire planes, one in the X(bend) direc-

tion and one at 30° to X. These are later transformed into X and Y. The VDC's contain a large number of wires (176/plane), therefore it is most economical to read out the drift time and wire number only for the wires that were struck (the same is done for the FEC's). Readout of the wire chamber data is handled by a Lecroy 4290 drift chamber control system. For a particular VDC track at least three wires are required for a valid hit. From these data the X and Y coordinates are calculated with a resolution of 150 μm.

MRS Trigger

The MRS has, in addition to the wire chamber instrumentation described above, a number of scintillators which can be used to provide a clean event trigger and time of flight and energy loss information for particle identification. The dipole entrance aperture is defined by 4 veto scintillators that eliminate events which might otherwise have scattered from the interior of the dipole. A signal in any of these (this condition will be denoted EV) nullifies the event. At the top of the MRS located just above the VDC's is a series of 10 scintillator paddles, $P_0 \cdots P_9$, which together span the focal plane. Any number of these can be included in the trigger thus limiting the extent of the focal plane considered and reducing the amount of unwanted data written to tape. This is especially useful for elastic scattering measurements since the elastic peak usually extends over a small region of the focal plane only. In many experiments the elastic scattering is not of interest yet it is often the dominant source of events. A veto scintillator which is located immediatly after VDC-2 can be used to prescale events over a narrow, well defined region of the focal plane.

A piece of apparatus known as the Focal Plane Polarimeter (FPP) is located above the MRS and has associated with it another pair of scintillators, S1 and S2. Including at least one of these in the trigger together with the paddles, significantly reduces the number of random coincidence triggers. The final trigger requirement

is that there is also a signal from either the X0 or Y0 FEC plane. A trigger is then defined by the logical expression

$$TRIG = (P_0 + P_1 + \cdots) \cdot S1 \cdot (X0 + Y0) \cdot \overline{EV} \tag{3.1}$$

3.2 Data Analysis

Data analysis for this experiment was carried out on the VAX cluster at TRIUMF. A set of user routines running within a command environment called LISA were used to analyse event-by-event data stored on magnetic tape. A real proton event consists of a fixed number of TDC and ADC values for the scintillators followed by a variable number of TDC values for all wires that were struck in the MRS. In the course of analysing an event the first user routine to be called is the DRIFT routine which converts TDC values and wire numbers from the VDC's and FEC's into position values for the corresponding wire plane. A second user routine, INSERT, uses the raw wire plane coordinates and calculates a set of secondary variables.

The target related coordinates are displayed in Figure 3.4. Secondary coordinates calculated using the raw FEC positions are: the traced back target positions XI, YI and ZI, the scattering angle in the horizontal plane (ϕ_{FEC}) measured relative to the central MRS angle, and the scattering angle in the vertical (bend) plane (θ_{FEC}). Variables calculated using the VDC positions are: the focal plane position XF which is proportional to the momentum of the scattered proton and θ_{pc} which is the angle of the proton trajectory relative to the central ray at the dipole exit corrected to be independent of XF. LISA allows the user to view histograms of both the raw wire plane coordinates and the secondary coordinates. Software gates can then be applied to the coordinates based on the information in the histograms.

A scattering plane projection of a typical event is depicted in Fig. 3.4. The coordinate ZI represents the image of the target cell projected onto the beam axis. Gates are placed on ZI to eliminate events which scattered in the end caps of the target cell. The true scattering angle in the horizontal plane is given by $\phi = \alpha - \phi_{FEC}$

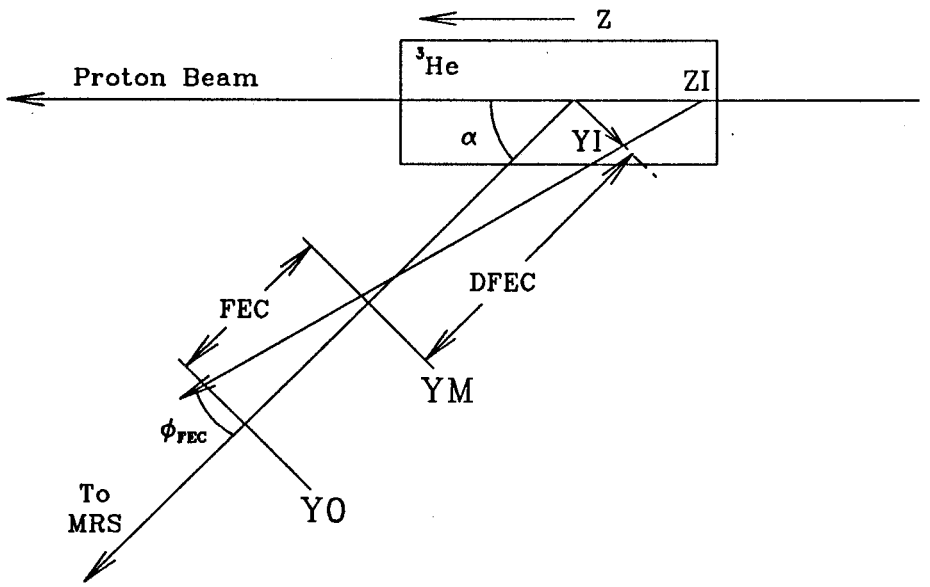

Figure 3.4: Target reconstruction for E566

where

$$\phi_{FEC} = \tan^{-1}[(Y0 - YM)/FEC] \; . \tag{3.2}$$

The variable YI is calculated from the equation $YI = YM - DFEC * \tan(\phi_{FEC})$ and is just the target image projected onto a line at an angle of (90 - α) to the beam axis. YI is then projected onto the beam axis via the transformation

$$ZI = YI * \frac{cos(\phi_{FEC})}{sin(\phi)}. \tag{3.3}$$

A typical histogram of ZI is shown in figure 3.5. Also shown in figure 3.5 is the ZI spectrum which results from placing very narrow gates on the coordinates ϕ_{FEC} and θ_{FEC}. This proved to be necessary for the determination of absolute cross sections.

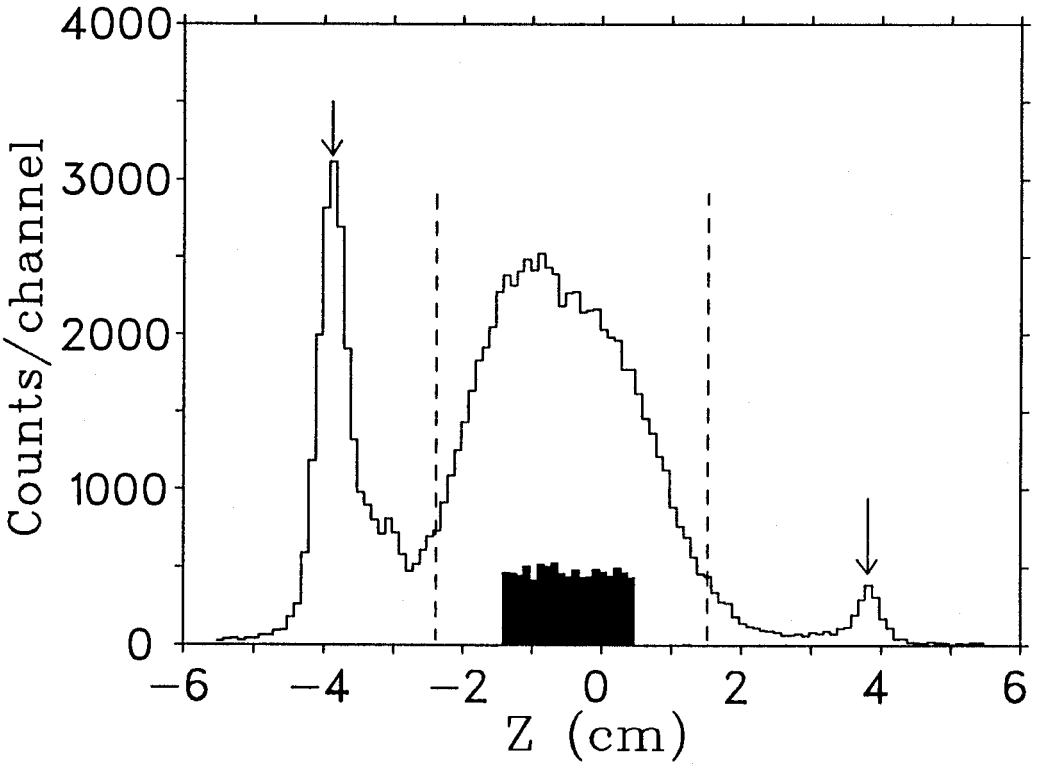

Figure 3.5: Histogram of the target image projected onto the beam axis.

For a point target the MRS has a finite angular acceptance which is ≈ 2.5 msr. With an extended target the region of constant angular acceptance is greatly reduced as can be seen from the ZI spectrum. The ^{3}He region of the spectrum is peaked because the MRS angular acceptance decreases with distance from the target center. This is fortunate since the number events from the glass endcaps would be about 100 times as large if the MRS acceptance were constant over the full range of ZI. In order for the ZI gates to be an accurate measure of the target length, we required that the angular gates be narrow enough that all target positions had a constant value of the acceptance. When this is achieved the ZI spectrum appears flat. In the current experiment the resulting solid angle was reduced to ~ 0.6 msr.

Variables calculated using the VDC positions are explicitly described in ref.[64] and are only be described briefly here. The focal plane of the MRS lies slightly in front (~ 5 cm) of the first VDC plane X1 and although it exhibits a slight curvature, it is usually a sufficiently good approximation to assume that it is flat. A number of corrections are generally applied to the raw XF position to remove spectrometer aberrations and hence optimize the intrinsic resolution of the spectrometer. In general, XF can depend on the target position and the entrance and exit angles of the particle. A new coordinate, XFPC, is defined as

$$XFPC = XF + a\phi_{FEC} + b\phi_{FEC}^2 + c\theta_{PC} + d\theta_{PC}^2 + e\theta_{PC}^4 + f\mathrm{ZI} \qquad (3.4)$$

where the parameters $a, b \cdots f$ are determined empirically. A missing energy spectrum is displayed in fig. 3.6.

The missing energy, ω, is obtained from XFPC through the equation

$$\omega = A(XFPC - B) + C \qquad (3.5)$$

where, A is the spectrometer dispersion in MeV/channel, B is the channel in which the elastic scattering peak occurs and C is the missing energy (in MeV) corresponding to a proton elastically scattered by a ^{3}He nucleus at 48°. The resolution of the ^{3}He elastic peak is several hundred keV FWHM.

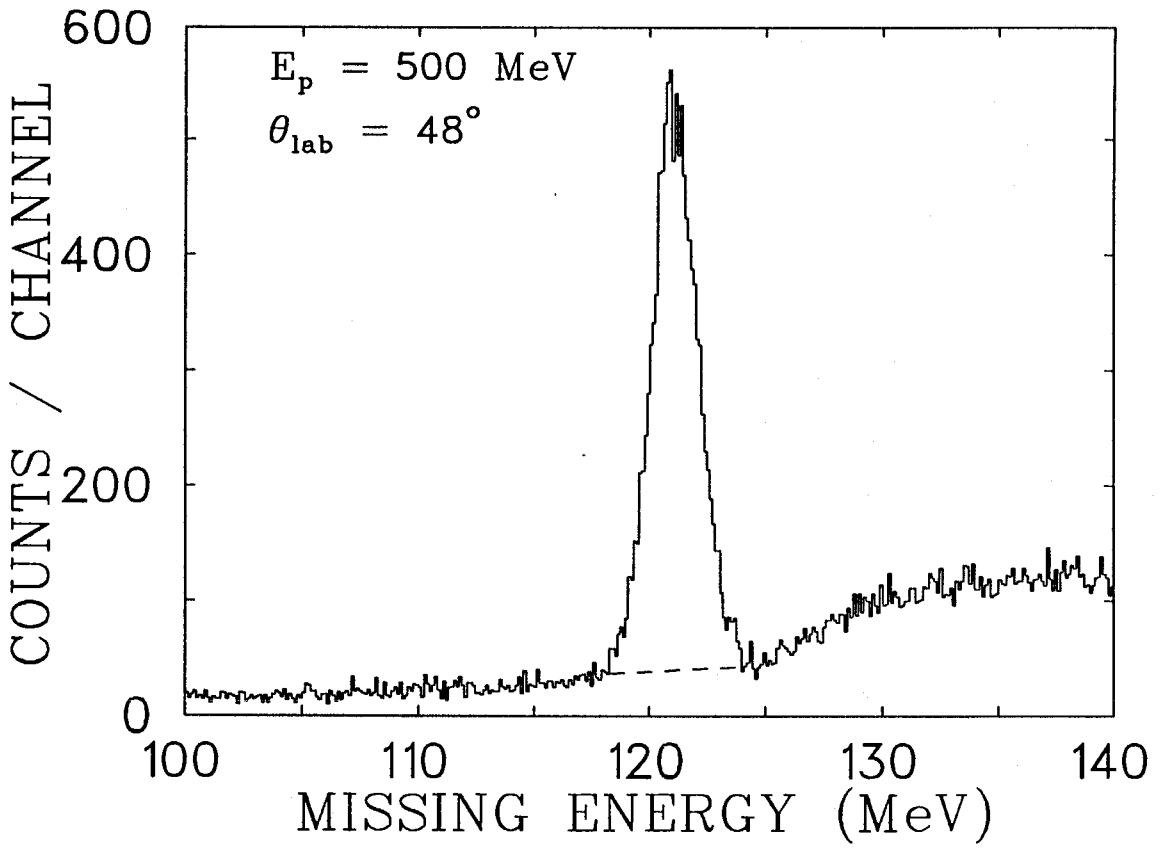

Figure 3.6: Histogram of missing energy for protons scattered from ^{3}He at 500 MeV incident energy.

3.2.1 The MRS Efficiency

The probability that a particle traversing the MRS will be detected is called the efficiency (ϵ). The scintillators of the MRS are assumed to have unit efficiency. Hence it is only the overall wire chamber efficiency which is required. The DRIFT routine gives, in addition to the raw wire plane coordinates the number of hits in a given plane. If the number of hits is 0 in any plane (this condition is denoted as MISS) then the event is rejected. If the number of hits is >1 (this condition is denoted as a multiple or MULT) then the event is also rejected because there is, at present, no algorithm for deciding which hit is actually the valid one. There is also a provision for setting software limits on the portion of the wire chamber in which valid hits can occur. This reduces the number of multiple hits. Portions of the chambers can also be "masked" in hardware. If a particle passes through the area which has been masked in software the DRIFT routine counts the hit as being outside (OUT) of the allowable area. If passing through the area which has been hardware masked the event would be counted simply as a MISS. Each wire plane is assigned a bit in a MISS, a MULT and an OUT variable and the bit is set equal to 1 if a MISS, a MULT or an OUT occurs in that particular plane.

Calculating wire chamber efficiencies (or inefficiencies) for this experiment was complicated by two factors: 1) a large fraction of missing events were caused by the use of an extended target and 2) a large number of MISS, MULT and OUT conditions which were shown to be highly correlated among several chambers, primarily in the FEC's. The latter condition arose primarily because of the high beam rates used during the experiment. The efficiency for a particular plane, X0 for example, was given by

$$\epsilon_{X0} = \frac{XM \cdot YM \cdot X0 \cdot Y0 \cdot X1 \cdot X2 \cdot PROT}{XM \cdot YM \cdot Y0 \cdot X1 \cdot X2 \cdot PROT} \tag{3.6}$$

where the $PROT$ condition implies that the event satisfied time-of-flight and energy loss constraints appropriate to a proton travelling through the MRS. The overall efficiency assuming no correlations would then be $\epsilon = \epsilon_{XM}\epsilon_{YM}\epsilon_{X0}\epsilon_{Y0}\epsilon_{X1}\epsilon_{X2}$. It was

found to be necessary to treat correlations among the FEC wire planes and among the VDC planes. However there were very few MISS or MULT events occuring in both the FEC's and VDC's.

The first problem mentioned above was solved by narrowing the YM software mask relative to the Y0 one. This eliminated many of the Y0 missing events which were largely due to protons being scattered from the cell end caps. The next step was to calculate separate efficiencies for the VDC's and the FEC's. This was done by defining a representative sample of events (RS) for either the FEC's or VDC's where one first considers all types of physically occuring events to determine whether or not they should have appeared in the final momentum spectrum from which the yields are obtained. If they should not have, then the event was omitted from the sample. An example of such an event is a MISS generated because the proton was OUT in that particular plane as well. If this was the case then the condition $\mathrm{MISS}_{XM}\cdot\mathrm{OUT}_{XM}$ would be true. When considering the VDC efficiency the RS was defined by

$$RS_{VDC} = PROT \cdot FEC \cdot \overline{(OUT_{X1} \cdot MISS_{X1}) + (OUT_{X2} \cdot MISS_{X2})} \qquad (3.7)$$

where FEC denotes an event which satisfied the condition $XM \cdot YM \cdot X0 \cdot Y0$. If the event should have appeared in the momentum spectrum, but was rejected, then a correction counter defined by

$$\begin{aligned} COR_{VDC} \;=\; & PROT \cdot FEC \cdot (MISS_{X1} \cdot \overline{OUT_{X1}} + MISS_{X2} \cdot \overline{OUT_{X2}} \\ & + MULT_{X1} + MULT_{X2}) \end{aligned} \qquad (3.8)$$

was incremented.

The efficiency for either the FEC or VDC portion is then

$$\epsilon_{FEC,VDC} = 1 - (COR_{FEC,VDC}/RS_{FEC,VDC}) \; . \qquad (3.9)$$

The total MRS efficiency is then the simple product of the two. Correlations among the wire planes are properly treated by using an OR (+) of the MISS/MULT

conditions for all of the planes in a certain group. For example, $MULT_{FEC} = MULT_{X0} + MULT_{Y0} + MULT_{XM} + MULT_{YM}$ determines the total number of multiples in the FEC's without double counting.

3.2.2 Calculation of cross sections and spin observables

The differential cross section for a scattering process can be written

$$\frac{d\sigma}{d\Omega} = \frac{N_{scat}A}{N_{inc}N_o\tau}\frac{1}{\Delta\Omega} \tag{3.10}$$

where N_{inc} is the number of incident particles, A is the atomic weight of the target nuclei, N_o is Avogadro's number, τ is the areal density of the target and $\Delta\Omega$ is the allowed solid angle for scattering which was determined by gates applied to the FEC coordinates. The areal density of the target is given by ρ/Δ_{ZI} where ρ is the ^{3}He density and Δ_{ZI} is the target length as defined by the ZI gates. The true number of scattered particles N_{scat} is determined from the measured yields N_{meas} by

$$N_{scat} = \frac{N_{meas}}{lt \cdot \epsilon \cdot Acc} \tag{3.11}$$

where lt is the electronics live time, ϵ is the total detector efficiency and Acc is an MRS acceptance correction. The acceptance correction was determined during a previous MRS experiment and is necessary because the probability of a particle successfully being transmitted through the MRS is dependent on the focal plane position. As previously mentioned in section 3.1.1 the electronics livetime is given by the ratio of the number of random pulser events accepted by the acquisition system to the total number submitted.

The cross section, $d\sigma/d\Omega$, which will be abreviated to σ in the following discussion, was measured for the four possible beam and target polarization combinations. The spin observables A_{OOON}, A_{OONO} and A_{OONN}, which were defined in the introduction, are related to the measured spin dependent cross section and the calculated unpolarized cross section (σ_o) by the equation [25,26]

$$\sigma = \sigma_o(1 + P_t A_{OOON} + P_b A_{OONO} + P_t P_b A_{OONN}) \tag{3.12}$$

where P_t and P_b are the target and beam polarization, respectively. Several data sets were acquired at each angle and for each beam and target polarization state. This resulted in an overdetermined set of equations from which the cross section and spin observables were extracted by a least squares minimization of the function

$$\chi^2 = \sum_i \frac{(\sigma_i - \sigma_o(1 + P_{b_i} A_{ooNo} + P_{t_i} A_{oooN} + P_{t_i} P_{b_i} A_{ooNN}))^2}{(\Delta\sigma_i)^2} . \tag{3.13}$$

The sum is over individual data sets i at a given angle.

3.3 Optical Model Calculations of $\vec{p}$-^{3}He Elastic Scattering

The elastic scattering results from this experiment are compared to two optical model reaction theories. Both calculations utilize the Distorted Wave Impulse Approximation or DWIA which is described briefly in appendix A. The microscopic formalism by which an average N-nucleus optical potential and scattering amplitude can be constructed from the free NN interaction (the "impulse" approximation), was first presented by Kerman, McManus and Thaler[20]. A very brief outline of the KMT version of multiple scattering theory is presented in Appendix A.

3.3.1 The Nonrelativistic Optical Potential Calculation

At intermediate energies it is expected to be a good approximation to use a simple product or "factorized" form for the momentum space optical potential[23] wherein the NN t-matrix is simply multiplied by the appropriate nuclear density function. In configuration space this optical potential would have a shape similar to the shape of the nuclear matter distribution. The first order optical potential used in [23] is

$$\begin{aligned} U(\vec{k}'|\vec{k}) \simeq U^1(\vec{k}'|\vec{k}) = \langle\psi_A| t^{pN} |\psi_A\rangle \approx \\ N\{t^{pn}_{A+B}\rho^n_{mt}(q) + [t^{pn}_{A-B}\vec{\sigma}_p \cdot \hat{\mathbf{n}}\vec{\sigma}_n \cdot \hat{\mathbf{n}} + t^{pn}_E \vec{\sigma}_n \cdot \hat{\mathbf{n}} + t^{pn}_{C+D}\vec{\sigma}_p \cdot \hat{\mathbf{m}}\vec{\sigma}_n \cdot \hat{\mathbf{m}} + \\ t^{pn}_{C-D}\vec{\sigma}_p \cdot \hat{\mathbf{l}}\vec{\sigma}_n \cdot \hat{\mathbf{l}} + t^{pn}_{CD}(\vec{\sigma}_p \cdot \hat{\mathbf{m}}\vec{\sigma}_n \cdot \hat{\mathbf{l}} + \vec{\sigma}_p \cdot \hat{\mathbf{l}}\vec{\sigma}_n \cdot \hat{\mathbf{m}})]\rho^n_{sp}(q) + \\ t^{pn}_E \vec{\sigma}_p \cdot \hat{\mathbf{n}}\rho^n_{mt}(q)\} + \left\{\frac{N \to Z}{n \to p}\right\} \end{aligned} \tag{3.14}$$

where ρ^n_{mt} and ρ^n_{sp} are the matter and spin densities for neutrons in ^{3}He. The directions $\hat{\mathbf{n}}$, $\hat{\mathbf{m}}$ and $\hat{\mathbf{l}}$ are defined in terms of the momentum vectors of the incident proton ($\mathbf{k}$) and the scattered proton ($\mathbf{k}$) by

$$\hat{\mathbf{n}} = \frac{\mathbf{k} \times \mathbf{k}'}{|\mathbf{k} \times \mathbf{k}'|}, \quad \hat{\mathbf{m}} = \frac{\mathbf{k} - \mathbf{k}'}{|\mathbf{k} - \mathbf{k}'|}, \quad \hat{\mathbf{l}} = \frac{\mathbf{k} + \mathbf{k}'}{|\mathbf{k} + \mathbf{k}'|} \tag{3.15}$$

so that $\hat{\mathbf{n}}$ is normal to the scattering plane. The t-matrices $t^{pn}_{A+B} \cdots$ differ from the scattering amplitudes of equation 1.4[23] by kinematic factors only. The spin and matter densities for protons and neutrons in ^{3}He are derived from the electromagnetic form factors $F_m(q)$ and $F_{ch}(q)$ measured in electron scattering experiments. Specifically, the required densities are constructed using the following relationships,

$$\rho^p_{mt}(q) = F_{ch}(^3He)/f^p_{ch} \tag{3.16}$$

$$\rho^n_{mt}(q) = F_{ch}(^3H)/f^p_{ch} \tag{3.17}$$

$$\rho^n_{sp}(q) = [\mu_p^2 F_m(^3H) - \mu_n^2 F_m(^3He)]/[f^p_{ch}(\mu_p^2 - \mu_n^2)] \tag{3.18}$$

$$\rho^p_{sp}(q) = \mu_p \mu_n [F_m(^3H) - F_m(^3He)]/[2 f^p_{ch}(\mu_p^2 - \mu_n^2)] \tag{3.19}$$

where f^p_{ch} (f^p_m) is the charge (magnetic) form factor of the proton and $\mu_{p,n} = 2.793$, -1.913 is the magnetic moment of the proton or neutron in nuclear magnetons. While not evident from the form of equation 3.14, both the e and f amplitudes of equation 1.4 are contained in it. A slight restructuring of the t_E terms yields the e and f parts of the optical potential

$$U_e = \frac{1}{2}\left[N t^{pn}_E(\rho^n_{mt} + \rho^n_{sp}) + Z t^{pp}_E(\rho^p_{mt} + \rho^p_{sp})\right](\sigma^p + \sigma^2) \tag{3.20}$$

and

$$U_f = \frac{1}{2}\left[N t^{pn}_E(\rho^n_{mt} - \rho^n_{sp}) + Z t^{pp}_E(\rho^p_{mt} - \rho^p_{sp})\right](\sigma^p - \sigma^2)\,. \tag{3.21}$$

Since the spin and matter densities are not equal for both neutrons and protons in ^{3}He, one expects a nonvanishing f amplitude.

The Lippmann-Schwinger equation to be solved using the above potential is

$$T^{JS}_{ll'}(k', k) = U^{JS}_{ll'}(k', k) + \frac{2}{\pi}\sum_L \int_0^\infty p^2 dp \frac{U^{JS}_{lL}(k', p) T^{JS}_{Ll'}(p, k)}{E(k_o) - E(p) + i\epsilon} \tag{3.22}$$

where $E(k_o) = E_p(k_o) + E_A(k_o)$ is the total relativistic energy of the projectile (p) and target (A) with c.m. momentum k_o. A proper development of the f-term in the optical potential requires coupling of the singlet and triplet ($J = 0$ and $J = 1$) NN partial waves [23] which is forbidden in the NN system because of the generalized Pauli exclusion principle. A proper treatment of this is not included in the numerical computations at present. Instead Landau *et al.* assume that the f amplitude will be of comparable size to the e amplitude and that the constant of proportionality between them will be the ratio of the forward angle optical potentials from which the amplitudes are generated, i.e.

$$f^A(\theta) = NU_f(k', k; E) \tag{3.23}$$

where

$$N = \frac{e^A(0°)}{U_e(0°)} \,. \tag{3.24}$$

The model of Ray *et al.* uses the nonrelativistic Distorted Wave Born Approximation (DWBA) in cojunction with the impulse approximation of ref.[20]. The formalism was developed for relativistic calculations which utilize 4 component Dirac spinors. The Relativistic Impulse Approximation (RIA) formalism is given in ref.[24] and is briefly outlined in the following.

The relativistic approach to N-Nucleus scattering begins with the Dirac equation

$$[\alpha \cdot \mathbf{p} + \beta(m + \sum_{i=1}^{N} v_{pi}) + H_A]\psi_{g.s.} = E\psi_{g.s.} \tag{3.25}$$

where the projectile-target product wavefunction $\psi_{g.s.} = \phi_p(r)\Phi_{g.s.}$ consisting of a Dirac 4-component wavefunction for the projectile $\phi_p(r)$ and target $\Phi_{g.s.}$ where $\Phi_{g.s.}$ is a solution of

$$H_A\Phi_{g.s.} = \epsilon_o\Phi_{g.s.}. \tag{3.26}$$

The optical potential is given by

$$U^1_{opt} = \sum_{i=1}^{A} \langle \Phi_{g.s.} | \, t_{pi} \, | \Phi_{g.s.} \rangle \tag{3.27}$$

where t_{pi} the NN t-matrix for scattering of the incident proton by the target nucleon i. The NN t-matrix is cast into a Lorentz invariant form involving the five terms: scalar, vector, pseudoscalar, axial vector and tensor is

$$t_{pi} = F_S + F_P\gamma_p^5\gamma_i^5 + F_V\gamma_p^\mu\gamma_{i\mu} + F_A\gamma_p^5\gamma_p^\mu\gamma_i^5\gamma_{i\mu} + F_T\sigma_p^{\mu\nu}\sigma_{i\mu\nu} \ . \tag{3.28}$$

For a spin 0 nucleus only three terms survive in the Optical potential, the scalar, U_S timelike vector $\gamma_o^0 U_V$ and small tensor term. The individual potentials are given by [24]

$$U_S(r) = (2\pi)^{-3} \sum_{i=p,n} \int d^3q e^{-iq\cdot r} F_S^i(q)\tilde{\rho}_S^i(q) \tag{3.29}$$

$$U_V(r) = (2\pi)^{-3} \sum_{i=p,n} \int d^3q e^{-iq\cdot r} F_V^i(q)\tilde{\rho}_V^i(q) \tag{3.30}$$

$$U_T(r) = (2\pi)^{-3} \sum_{i=p,n} r \int d^3q e^{-iq\cdot r} F_T^i(q)\tilde{\rho}_T^i(q) \tag{3.31}$$

$$\tag{3.32}$$

where the $\tilde{\rho}$ terms are Fourier transforms of the appropriate density ie.

$$\tilde{\rho}_S(q) = \int d^3r e^{-q\cdot r}\rho_S(r) \ . \tag{3.33}$$

The tensor term is usually small and is often omitted. For non spin-0 nuclei all terms in the NN interaction can contribute to the optical potential.

For DWBA calculations, the Born scattering amplitude and the distorted waves are generated using only the scalar and timelike vector parts of the optical potential. The densities used in constructing these optical potentials are parameterized using Woods-Saxon forms i.e.

$$\rho_V = \rho_{theory} + \frac{\rho_o'}{1 + exp[(r-c)/z]} \tag{3.34}$$

where the parameters c and z are adjusted to optimize fits of the cross section and analyzing power data at 500 MeV. The full scattering amplitude f is then given as

$$f = f_{core} - \frac{m}{2\pi(\hbar c)^2} \left\langle \chi^- \right| \left\langle \phi_{g.s.} \right| t_{oi}' \left| \phi_{g.s.} \right\rangle \left| \chi^+ \right\rangle \tag{3.35}$$

where χ are relativistic distorted waves and f_{core} is the exact elastic scattering amplitude for the simplified potential. The spin dependent terms of the NN interaction that allow for a ^{3}He spin flip, (t'_{oi}) are contained in the second term.

The ^{3}He ground state wave function used in these calculations is that of 3 nucleons in the $1s_{1/2}$ orbital. The wave functions are adjusted to fit the total ^{3}He magnetic form factor of ref. [65]. Compatability with the relativistic formalism of ref.[24] is maintained by setting the lower components of both the distorted waves and the $2S_{1/2}$ ^{3}He wave function equal to their free particle values i.e.

$$\psi_L = \frac{\sigma \cdot k}{E + m} \psi_U \ . \tag{3.36}$$

The proton mass is replaced with the reduced total energy in the p - ^{3}He c.m. system.

3.4 Experimental Results and Comparison with Theory

Cross sections and the spin observables A_{OONO}, A_{OOON} and A_{OONN} for proton elastic scattering have been measured at incident energies of 200, 290, 400 and 500 MeV. The measured differential cross sections are shown in Fig. 3.7. and are in excellent agreement with the previous data of Hasell *et al.* [27] at all energies. The slight discrepancies at the lowest scattered proton energies (largest q), for the 200 and 290 MeV data, are probably due to differences in the corrections for straggling and multiple scattering. The results of these comparisons are very encouraging however, if one considers that the cross sections range over three orders of magnitude and that Hasell *et al.* used a liquid target which was 100 times thicker than the ^{3}He target described in chapter 2. The theoretical calculations of Landau[23] are in qualitative agreement with these data.

The beam related analyzing powers at all 4 energies are shown in Figure 3.8 together with the microscopic optical model prediction of Landau[23]. The rapid

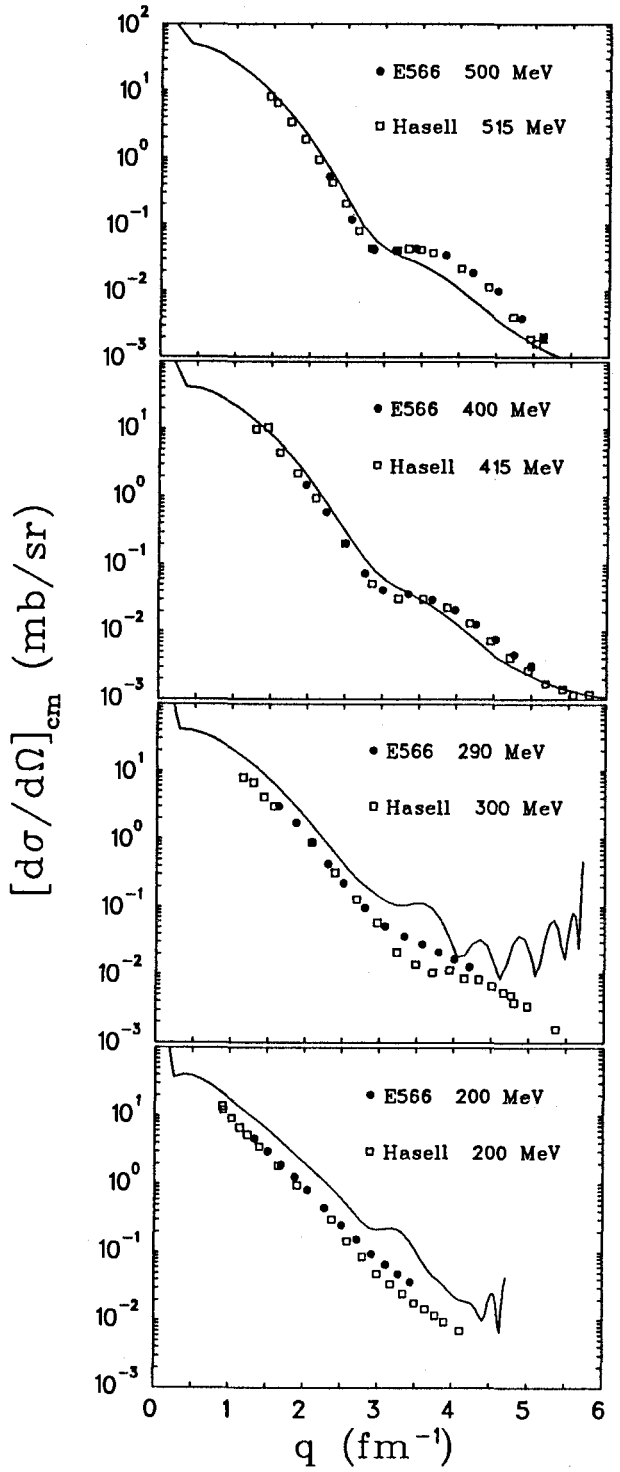

Figure 3.7: Cross sections for p–^{3}He elastic scattering The calculations are from ref.[23]

variation of A_{OONO} with q or θ arises from cancellations among the large amplitudes a, b, e and f which vary in sign, particularly those induced by Im(a) which also varies rapidly with q. The overall agreement between theory and data is fair. The importance of the f term in the nuclear amplitude, which vanishes for the NN system, is evident from the difference between A_{OONO} and A_{OOON} in the data of Figs. 3.8 and 3.9. Recalling that $A_{OONO} = Re(a^*e + b^*f)/\sigma$ and $A_{OOON} = Re(a^*e - b^*f)/\sigma$ it is observed that a substantial difference in these two observables implies that the f amplitude must be sizeable. The theoretical calculations of Landau[23] clearly fail to treat the dependence of these observables on the b^*f term correctly.

Preliminary DWBA calculations by L. Ray[24] who used the nonrelativistic DWBA are shown as dashed lines in Fig. 3.10. Parameters in this calculation were adjusted to reproduce cross sections and analyzing powers. Although this calculation is in better agreement with the data, especially at low momentum transfer, it appears that the new spin observables are sensitive to parts of the scattering amplitude not tested by σ and A_y measurements and that these parts are not calculated well enough.

For A_{OONN} (shown in Fig. 3.11) the calculations bear little resemblance to the data. Recalling that $A_{OONN} = (|a|^2 - |b|^2 - |c|^2 + |d|^2 + |e|^2 - |f|^2)/2\sigma$, small measured values imply that the large amplitudes a, b, e, and f are cancelling. This observation is also consistent with the existence of a large f amplitude. The observation of a small A_{OONN} implies that an accurate theory would have to successfully provide for cancellation among at least 4 large amplitudes a, b, e and f to create a small observable. These data therefore provide a very sensitive test of current microscopic optical model theories.

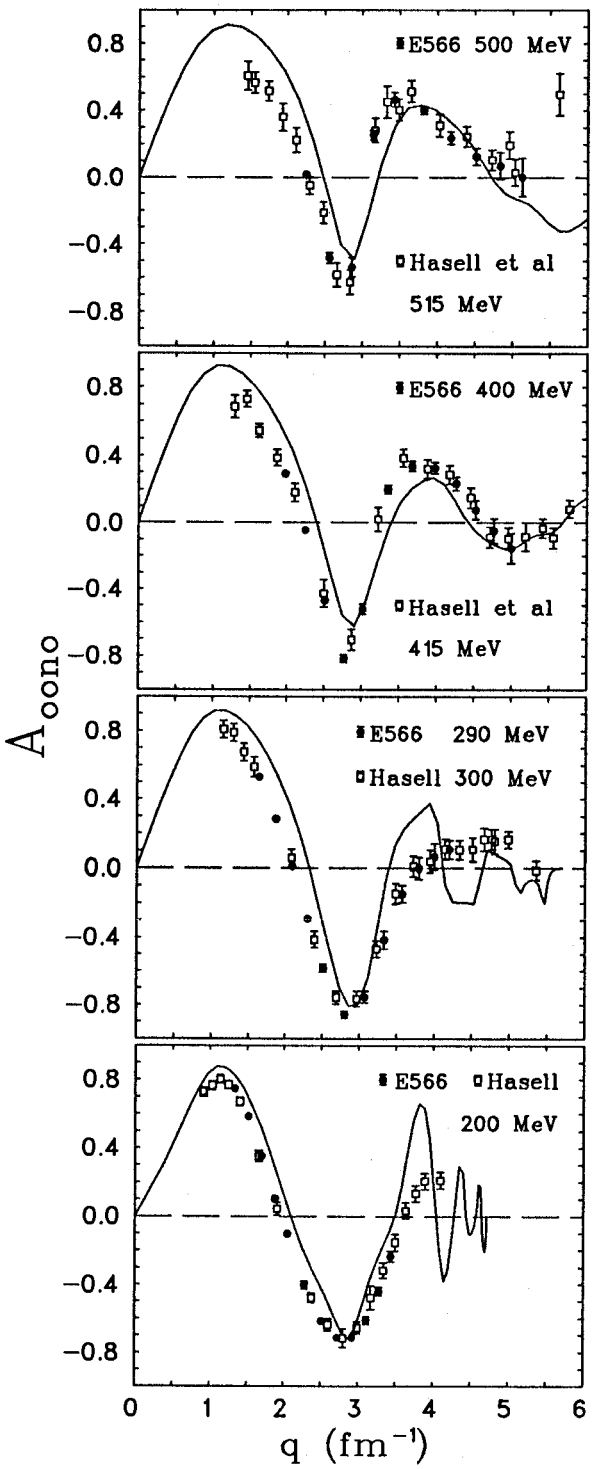

Figure 3.8: Beam related analyzing power for $\vec{p}-^3\vec{H}e$ scattering. The calculations are from ref.[23]

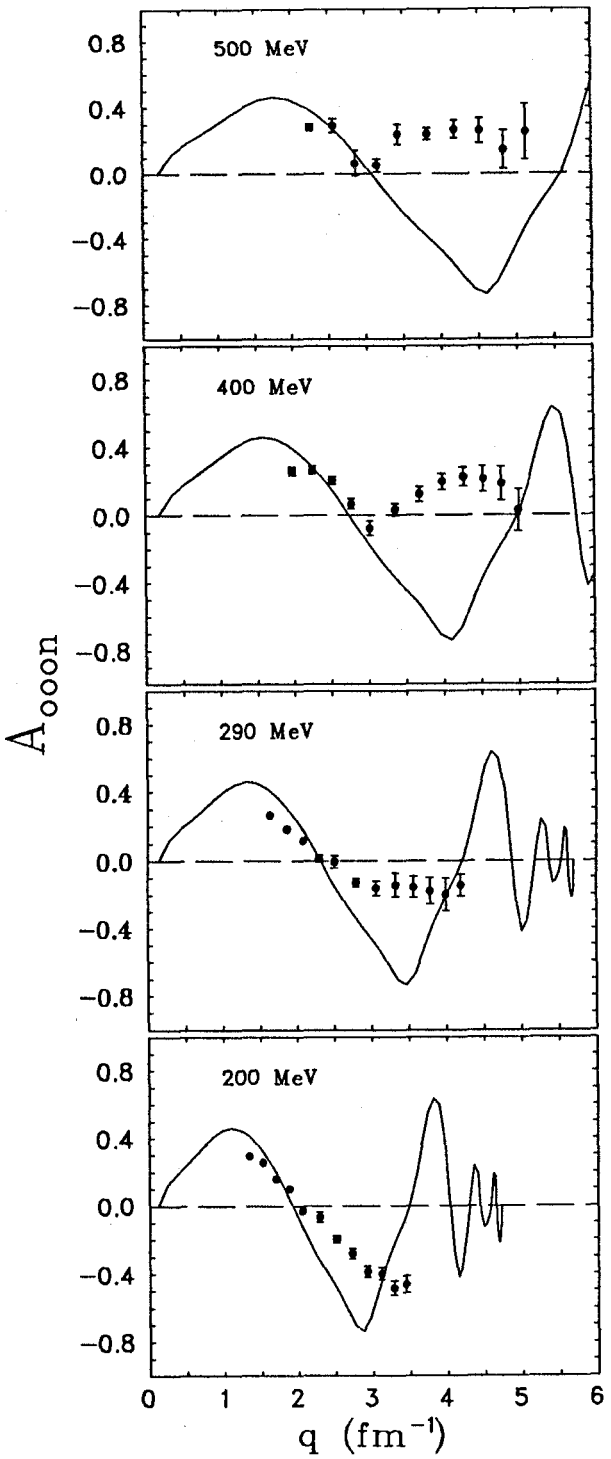

Figure 3.9: Target related asymmetry for $\vec{p}-^3\vec{H}e$ scattering. The calculations are from ref.[23]

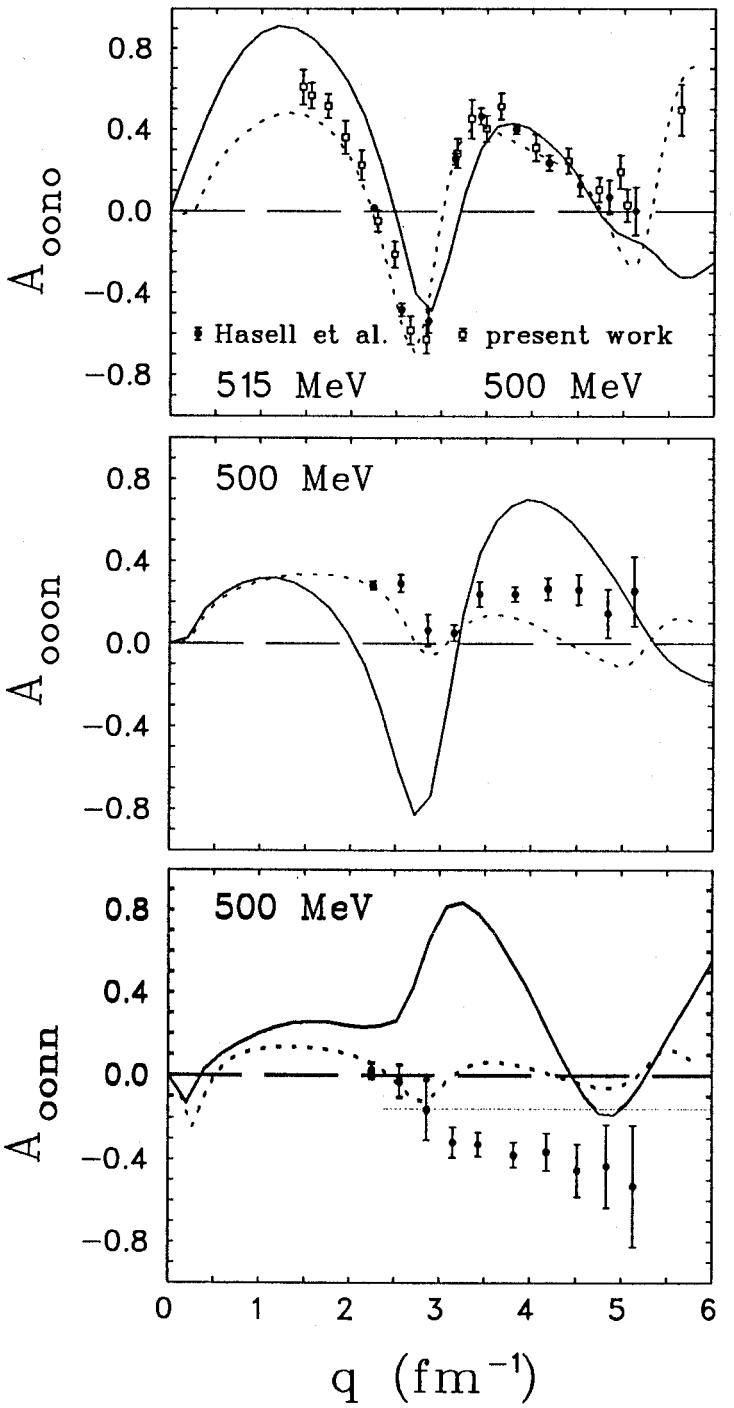

Figure 3.10: Target related asymmetry for $\vec{p}-^3\vec{H}e$ scattering. The calculations are from ref.[23] (solid line) and ref. [24] (dashed line)

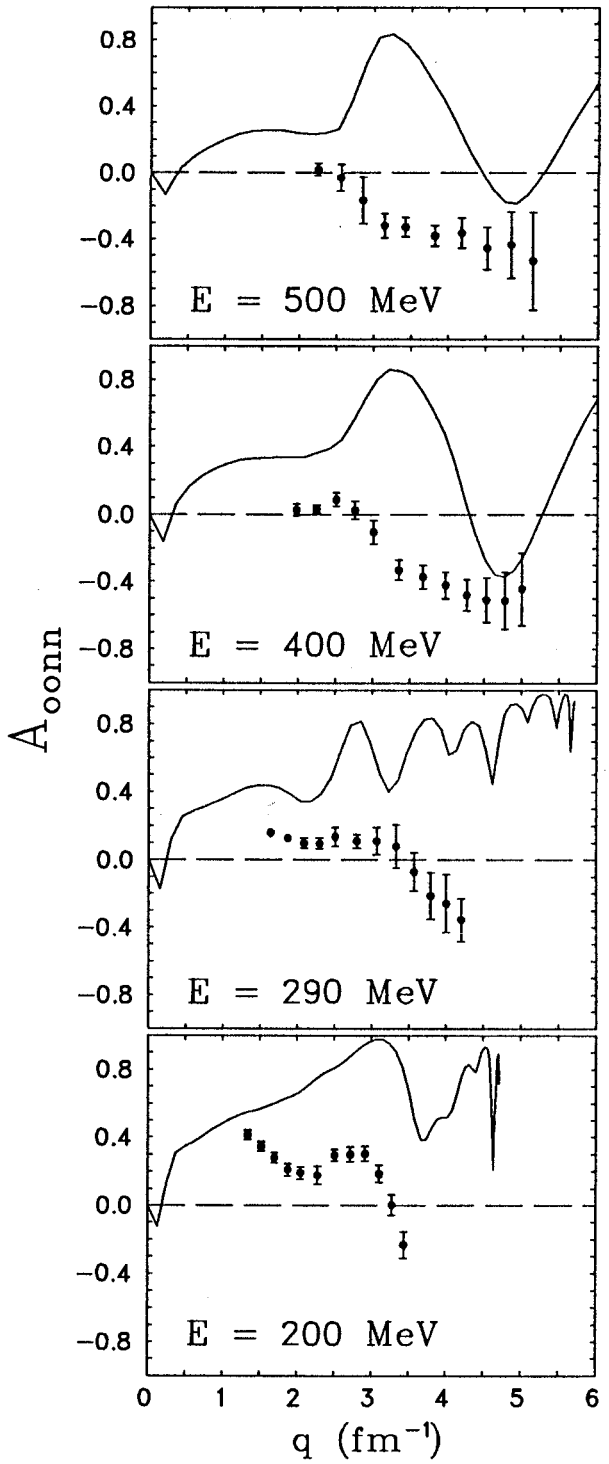

Figure 3.11: The spin correlation parameter A_{OONN} for $\vec{p}-^3\vec{H}e$ scattering at various energies. The calculations are from ref. [23]

Chapter 4

Elastic Scattering of Pions from Polarized ^{3}He

This chapter is divided into four sections. The first two sections describe the experimental measurement and the associated data analysis of pion elastic scattering cross sections and asymmetries. The third section deals with the theoretical motivation for such measurements and outlines two reaction models which are compared to the data in section four.

4.1 The Experiment

The experiment was carried out at the M11 pion channel of the TRI-University Meson Facility (TRIUMF) using an optically pumped polarized ^{3}He gas target of 7.03 standard atm pressure and a typical polarization of 45–55%. A detailed discussion of the polarized ^{3}He target was given in chapter 2. The objectives of TRIUMF experiment 557 were cross section and asymmetry measurements for the reaction $^3\vec{\text{He}}(\pi^+,\pi^+)^3\text{He}$ at T_π = 100 MeV. Momentum analysis of the scattered pions was performed with a modified Quadrupole-Quadrupole-Dipole (QQD) magnetic spectrometer[66]. A total of 12 wire chamber planes were necessary to provide both the pion scattering vertex and the momentum of the scattered pion. The data were analysed on the TRIUMF VAX cluster using the NOVA analysis software package.

4.1.1 Beamline M11

A schematic drawing of the M11 pion channel[62] is shown in Fig. 4.1. The low intensity (1-10 MHz) pion beam is generated by the interaction of an intense 140μA proton beam of 500 MeV incident energy supplied by beamline 1A with a fixed ^{9}Be or ^{12}C target of 1.2cm thickness. This target, denoted as 1AT1, marks the beginning of the M11 beamline. Pions emitted at an angle of about 2.9° are deflected by an additional 1.2° by the quadrupole magnet, 1AQ9. Final separation of the proton and pion beams is achieved by the septum magnet S1.

A series of focusing and horizontal bending magnets (B1 and B2) serve to sweep unwanted particles from the beam and steer the beam to the interaction point in the M11 experimental area. In general, muons, protons and electrons which are also produced in 1AT1, will not have the same momentum as the pions and hence are not transmitted through the bending magnet combination of B1 and B2. Some contamination of the pion beam by these unwanted particles is present, although it is mostly due to pions that decay in flight upstream of the interaction region. The beam spot size on target is about 1cm FWHM. The momentum dispersion of the pion beam is determined by the width of the vertical slit located just after bending magnet B1. For this experiment the aperture setting was chosen to limit the momentum dispersion of the pion beam to $\Delta p/p < 2.0\%$ ($\Delta E \sim 3$ MeV at $E_{\pi+}$ = 100 MeV.

4.1.2 Experimental Setup

A schematic of the experimental setup is shown in Fig. 4.2. The pion beam encountered 2 sets of Multi-Wire Proportional Chambers (MWPC's) and a small scintillator before entering the ^{3}He target. The MWPC's are specifically designed to operate efficiently at the 1-10 MHz rates realized for chambers located directly in the beam. The wire arrangement in these chambers consists of a plane of anode wires with a cathode foil plane on either side which is maintained at a negative

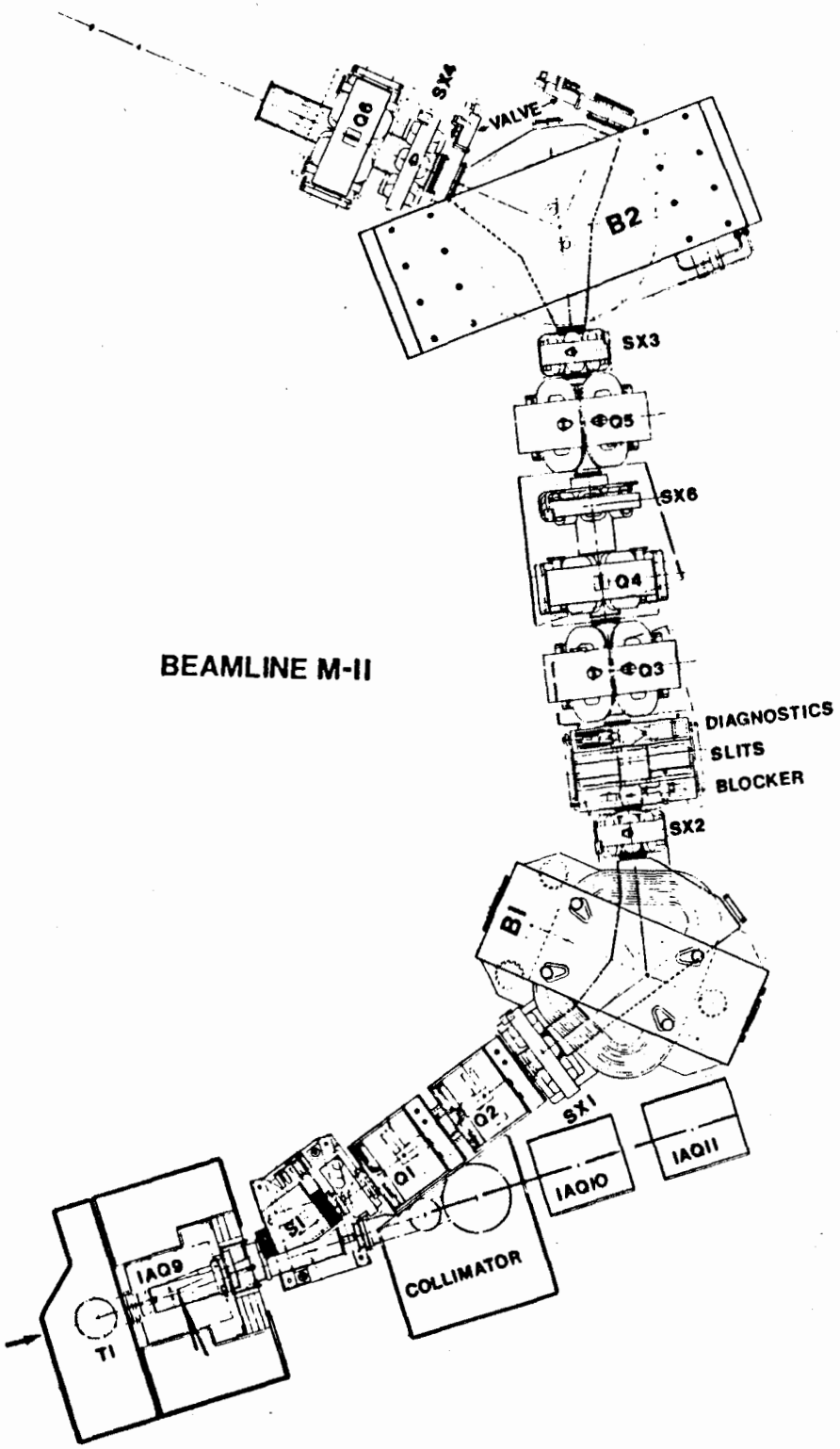

Figure 4.1: The TRIUMF M11 beamline.

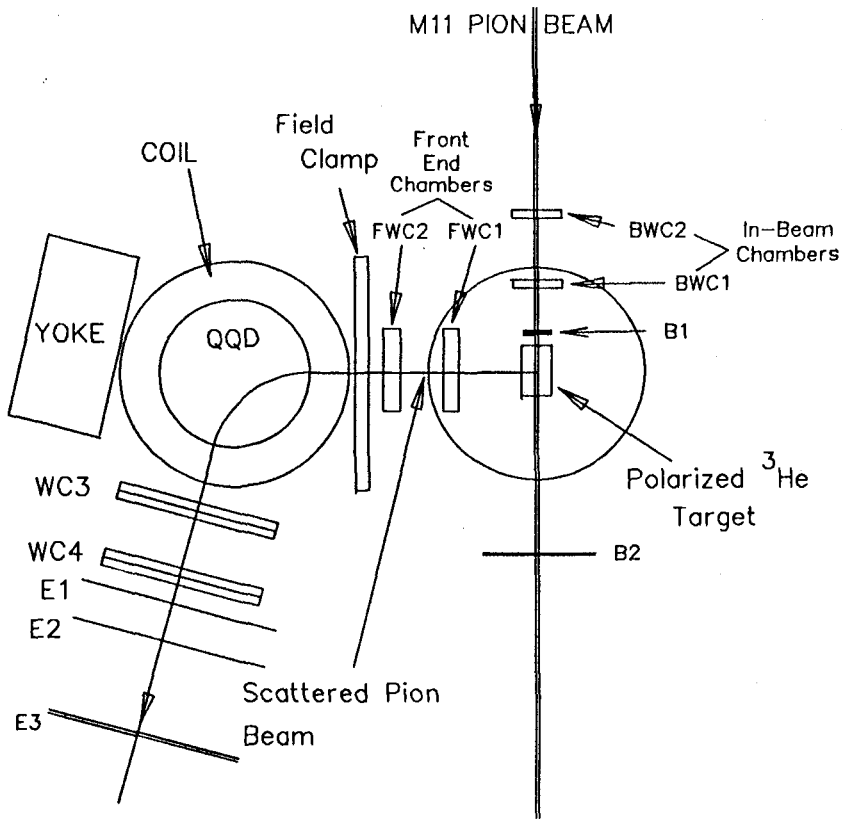

Figure 4.2: Experimental layout for E557.

high voltage. The free electrons, created when an ionizing particle passes through the chamber, drift to the anode wires. Every anode wire is instrumented with a preamplifier mounted directly on the wire chamber. The preamplifier signals are discriminated and read out individually by the LeCroy Proportional Chamber Operating System (PCOS) III readout system. Since there is no drift time interpolation with this system, spatial resolution is limited to the 0.76mm wire spacing. The first

beam chamber (BWC1 in Fig. 3.2) is located 341mm from the target center with the separation between the chambers being about 230mm. The corresponding resolution for traceback to the target is about 1mm in both the horizontal and vertical directions.

The small 17mm diameter scintillator (B1) placed directly upstream of the target cell defined the active area of the target, and in coincidence with a larger scintillator located downstream of the target (B2), measured the total beam charge incident on the target cell. The signal from B1 was used as the common start signal for all other electronics. It also formed part of the trigger system which will be discussed in the following section.

Another two sets of MWPC's were located after the target. Like the in-beam chambers each set has one wire plane in the horizontal and one in the vertical direction. These chambers are virtually identical to the in-beam chambers in construction and readout. They are, however, much larger (25.6cm x 25.6cm) and have a 1mm wire spacing. The first Front-End Chamber (FEC) was located 362mm from the target center with the separation between the chambers being 300mm. The tracking resolution from this side of the target was also about 1mm in both the horizontal and vertical directions. Only the detector areas which were compatible with the spectrometer acceptance were instrumented. The traceback from the FEC's in conjunction with that from the in-beam chambers was used to construct a three dimensional image of the target and subsequently exclude events which were observed to come from the glass vessel which contained the ^{3}He.

In addition to providing traceback to the target, the FEC's also constitute the instrumentation for the entrance to the QQD. The QQD is a quadrupole-quadrupole-dipole spectrometer capable of analyzing pions of up to 100 MeV kinetic energy. Due to the spatial extent of our target and the need to limit magnetic field gradients at the target to $<3\ \mu T\ cm^{-1}$, it was necessary to remove both quadrupoles. A field clamp was also installed to further reduce magnetic field gradients at the

target. These modifications reduced the QQD angular acceptance in the vertical (non-bend) plane to $\approx 3.5°$ whereas the spectrometer angular acceptance in the horizontal (bend) plane was as large as 12°. Two sets of delay line wire chambers were located at the exit of the QQD. These chambers were used to calculate the focal plane coordinate for the scattered pions. The final elements of the setup are the three scintillators E1, E2 and E3. In principle they are used to provide particle identification through energy loss and time of flight discrimination. They also form an integral part of the trigger system which is discussed next.

4.1.3 Data Acquisition and Electronics

A schematic of the QQD electronics is shown in Fig. 4.3. The trigger system for this experiment is depicted in the top part of the figure. The scintillator signals are combined in coincidence creating the preliminary trigger condition defined as QQD = B1•E1•E2•E3. The condition QQD was used as the final trigger condition in a test run but it was found that most of the events were due to random coincidences. The event rate did not depend significantly on whether the QQD was on or off. An OR'd signal from the Y-planes of both FEC's was added in order to ensure that the triggering particle actually passed through the QQD. The final trigger condition was defined as TRIG = QQD•(Y1+Y2)•$\overline{BUSY}$ where $\overline{BUSY}$ means that the computer is ready to read the event. This causes CAMAC to generate a LAM (Look At Me) signal which prompts the computer to read the event. The LAM's accepted by the computer, are counted by a CAMAC scaler as are the events satisfying the coincidence QQD•(Y1+Y2). The ratio of these two scaler values is the computer livetime fraction.

4.2 Data Analysis

Data were acquired and written to magnetic tape using the VDACS data acquisition system running on a VAX 3100 computer. The NOVA data analysis software

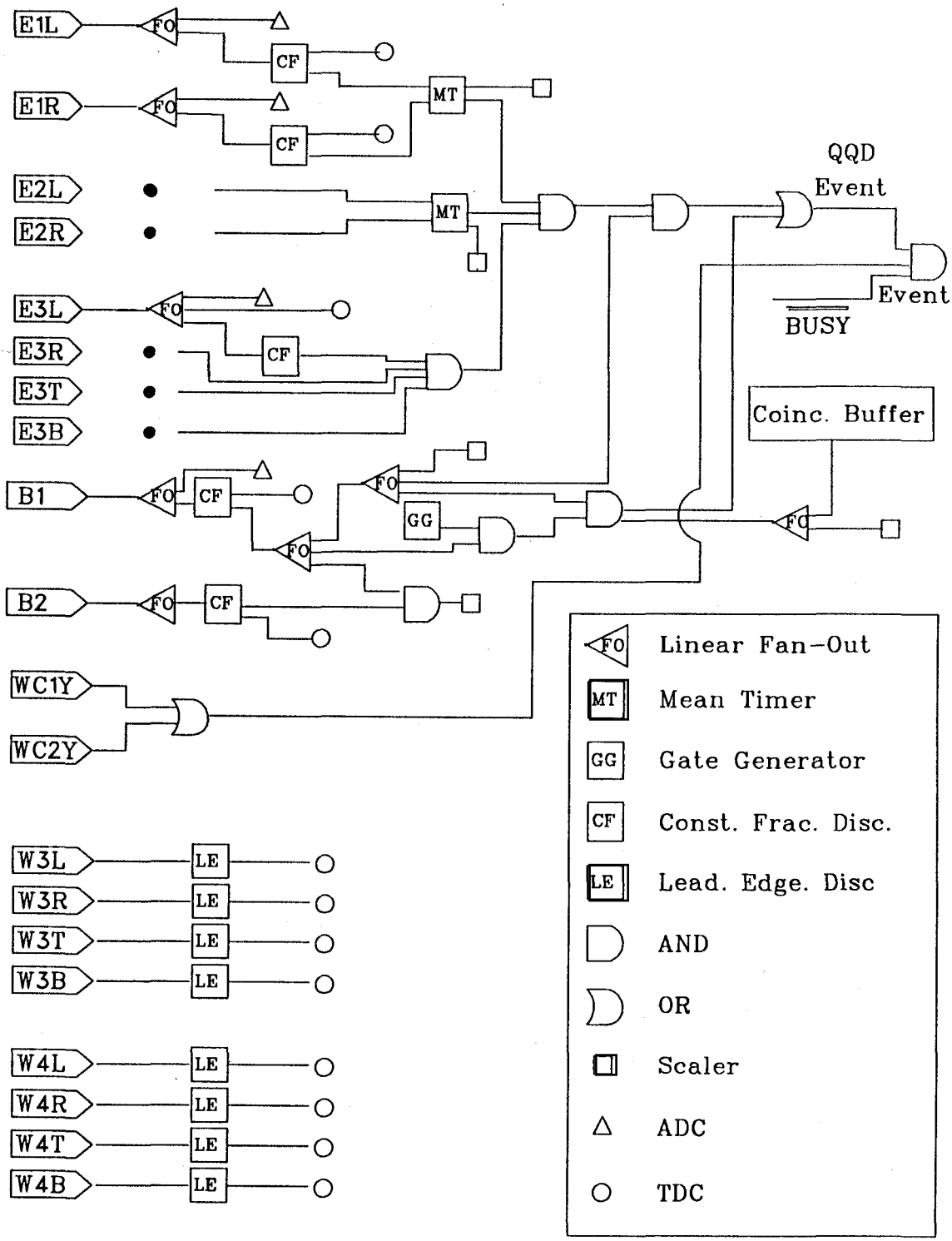

Figure 4.3: Schematic of the QQD electronics configuration.

package was used for both the online and offline analysis of the data and will be described in the following section.

4.2.1 The NOVA Program

Nova is used to read and analyse nuclear physics data on an event by event basis. The data source may be either the VDACS (the TRIUMF site standard data acquisition system) data buffer, if the analysis is being done online, or a magnetic tape or disk which contains data written by VDACS. The data, in the form of ADC and TDC values, MWPC wire addresses for all wires that were struck, and a single word from the Digital Coincidence Register (a CR212 unit) are copied into a predefined NOVA array and subsequently analysed. The primary function of the analysis program is to update histograms based on a set of user defined variables and conditions. The exact order in which this is done is determined by a user specified "Operation Sequence" or OPSEQ. The OPSEQ contains explicit statements instructing NOVA to update histograms or groups of histograms or evaluate conditions. Variables are only calculated if it is required in a histogram or condition evaluation. For lengthy calculations separate user defined FORTRAN subroutines which have been previously compiled can be called by NOVA. In this analysis such a routine was used to convert MWPC wire addresses into actual wire plane positions using a lookup table. The same routine also performed the vertex calculation which is discussed next.

4.2.2 Target Traceback and Vertex Reconstruction

Accurate determination of the pion scattering vertex within the target was essential for rejection of events which originated in the glass end caps and side walls of the target cell. A full 3-dimensional vertex reconstruction was used in order to optimize the traceback resolution. An outline of the vertex calculation follows.

The wire plane position variables for the vertex calculation are defined according to Fig. 4.4 with the directions $\hat{x}$, $\hat{y}$ and $\hat{z}$ defining the global coordinate sys-

tem. Since the coordinate system of the in-beam chambers is coincident with the global coordinate system, the direction of the incoming pion is given by its direction cosines, x_{in}, y_{in} and z_{in}, as follows,

$$dx = x_{b2} - x_{b1} \tag{4.1}$$

$$dy = (y_{b2} - y_{b1}) * db12x/db12y \tag{4.2}$$

$$r_{in} = (dx * dx + dy * dy + db12x * db12x)^{1/2} \tag{4.3}$$

$$x_{in} = \frac{dx}{r_{in}} \tag{4.4}$$

$$y_{in} = \frac{dy}{r_{in}} \tag{4.5}$$

$$z_{in} = \frac{db12x}{r_{in}} \tag{4.6}$$

where $db12x$ is the distance between the x planes of the in-beam chambers and similarly for $db12y$. This is depicted in Fig. 4.4. A similar calculation yields the direction cosines for the trajectory of the scattered pions, x_{out}, y_{out} and z_{out}. These have to be transformed from the FEC coordinate system which is rotated by an angle α with respect to the global coordinate system. One can then define the vertex position for the incoming and outgoing rays as

$$\vec{v}_{in} = \vec{P}_{b1} + \lambda \vec{r}_{in} \tag{4.7}$$

$$\vec{v}_{out} = \vec{P}_{f1} + \mu \vec{r}_{out} \tag{4.8}$$

where $\vec{P_{b1}}$ is the pion position as measured at z corresponding to the position of the x-plane of the first beam chamber (BWC1) and P_{f1} is the scattered pion position measured at the y-plane of the first FEC chamber. Ideally these two vectors should be identical, however misalignment of the incident and scattered trajectories can have several causes: misalignment of the chambers themselves, the finite intrinsic resolution of the detectors and multiple scattering in the target cell, front end scintillator or wire chamber windows. The Lagrange multipliers, λ and μ are consequently chosen to minimize the difference in the two vertices. Therefore one

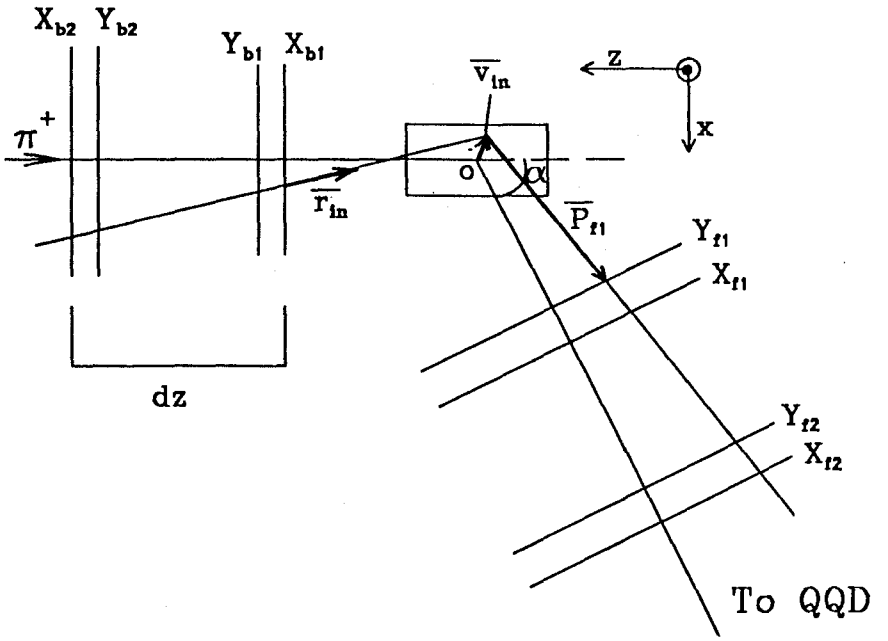

Figure 4.4: Coordinates used for the pion vertex reconstruction

chooses the multiplier values to satisfy the set of linear equations :

$$\frac{\partial \left|\vec{v}_{in} - \vec{v}_{out}\right|^2}{\partial \lambda} = 0 \tag{4.9}$$

$$\frac{\partial \left|\vec{v}_{in} - \vec{v}_{out}\right|^2}{\partial \mu} = 0. \tag{4.10}$$

$$\tag{4.11}$$

Upon solving for λ and μ one simply defines the "vertex" as $\vec{v} = (\vec{v}_{in} + \vec{v}_{out})/2$.

It is also useful to calculate the residual vector defined as $\Delta v = |v_{in} - v_{out}|$ which is used to reject events whose incident and scattered trajectories did not coincide within some reasonable distance. In this analysis the maximum allowed value of Δv was 3mm. With this constraint the fraction of events rejected due to multiple scattering was about 10%. The value 3mm was chosen to eliminate as few events as possible while still maintaining adequate traceback resolution. The final cross sections are corrected for these multiple scattering losses.

Two different projections of the target image, a one dimensional projection of the target cell onto the pion beam axis (z-coordinate) and a two dimensional projection of the cell onto the plane perpendicular to the beam axis (x-y plane) were used to identify the ^{3}He events. These spectra are displayed in Fig. 4.5. Software cuts on v_z eliminated events from the end caps while cuts on the cell radius coordinate ($r = \sqrt{x^2 + y^2}$) eliminated events from the cell walls. With the cuts from the tracking chambers the useable ^{3}He target length was 4.5 cm which corresponds to an areal density of 8.5x10^{20} atoms cm^{-2} (4.26 mg cm^{-2}).

Since events were only accepted for a limited value of the radius, which is smaller than the radius constraint of scintillator B1, the total number of beam particles measured by B1 had to be adjusted. This was done using data taken with the CH_2 target since the scattering probability does not vary with radius. Using this method it was found that at least 85% of the beam incident on B1 was within an acceptable radius of the beam axis.

4.2.3 Momentum Analysis

The two MWPC's (FWC1 and FWC2) located between the target and the spectrometer together with two additional chambers (WC3 and WC4) located at the back plane of the spectrometer allowed the focal plane of the dipole to be determined. The backplane wire chambers employ a delay line readout in contrast to the MWPC's. Each chamber contains two wire planes, one with vertical wires which

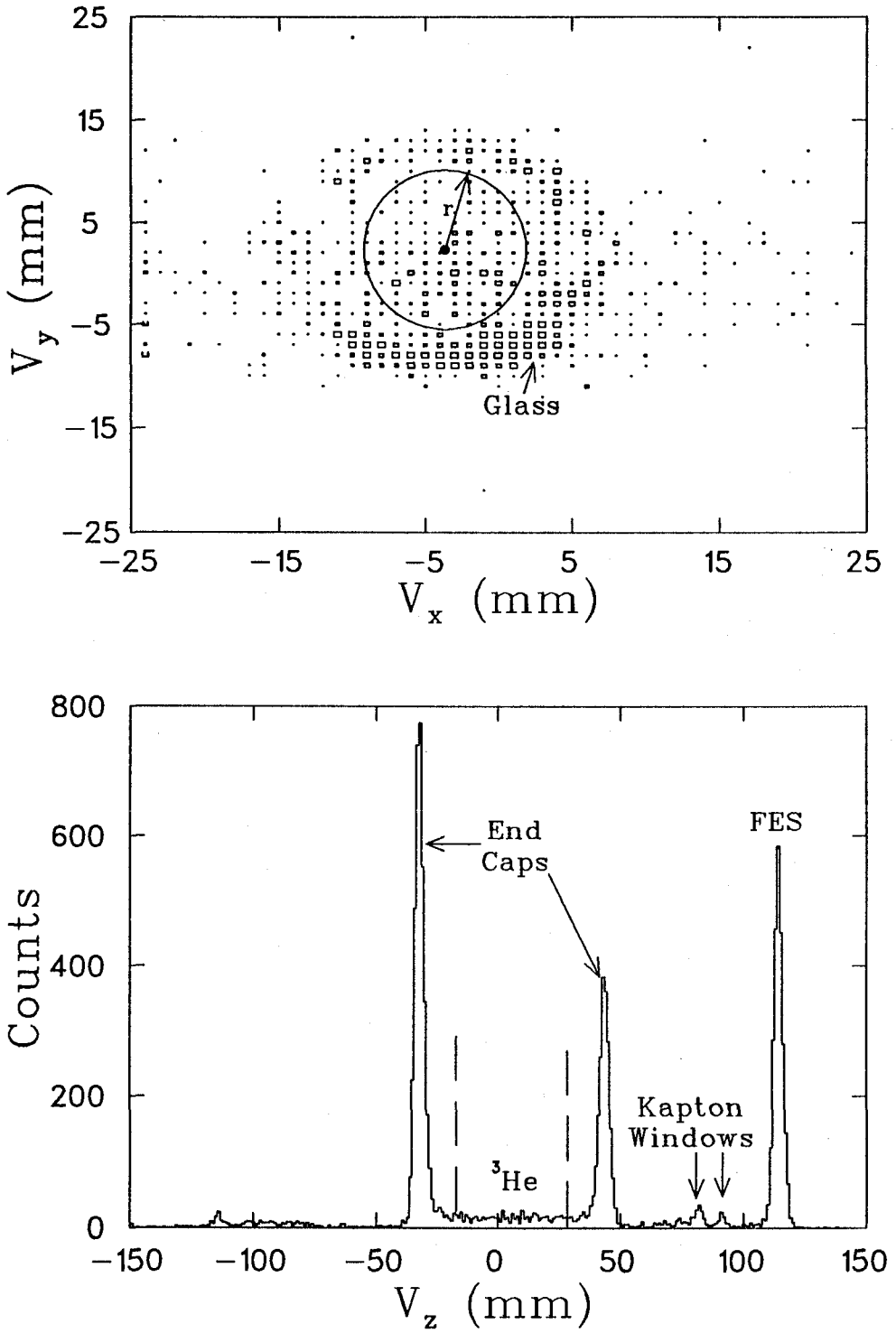

Figure 4.5: Cross section of ^{3}He traget cell looking along the beam axis (top). The target cell projected onto the beam axis (bottom).

gives the X coordinate and one with horizontal wires which gives the Y coordinate. All wires in a given plane are connected to a common delay line. A preamplifier mounted on each end of the delay line shapes the pulse and sends it to a TDC. The wires of the Y-plane are the anodes and therefore receive the electron avalanche. Events in the Y-planes are observed to occur only on individual wires resulting in a spacial resolution of one wire spacing or 2mm in this direction. The cathode signal is produced by induction from the anode signal.

For each wire plane, two TDC values are measured, one at each end of the delay line. The TDC value is the sum of the drift time and the time taken for the pulse to propagate to the end of the delay line. The position of the event in a given plane is proportional to the difference in the TDC values for that plane since the drift time is the same regardless of which end of the delay line one observes. The X coordinate for example is given by X=k*($T_{left} - T_{right}$) where k is the pulse propagation speed along the delay line. These constants were measured for each delay line individually. If two or more tracks occur simultaneously in a delay line wire chamber, only the time of the first pulse to arrive at either end will be recorded. These pulses may not originate from the same track but may still give a valid (although wrong) position. Another test is required to determine if the track was due to the passage of a single pion. The CHECKSUM test accomplishes this task. One uses the fact that $T_{left} + T_{right} = L/k + 2T_d$ where L is the length of the delay line. Since the anode (Y) and cathode (X) signals depend only on the drift time to the anode it is apparent that $T_{left} + T_{right} - (T_{up} + T_{down}) = L/k - L'/k'$ which should be constant. Since the signal pulses are not delta functions and are degraded significantly while propagating along the delay line, one expects the CHECKSUM variable to have a small range of values around the constant $L/k - L'/k'$. A typical CHECKSUM spectrum is displayed in Fig. 4.6.

An outline of the focal plane geometry is presented in Fig. 4.7. In terms of the

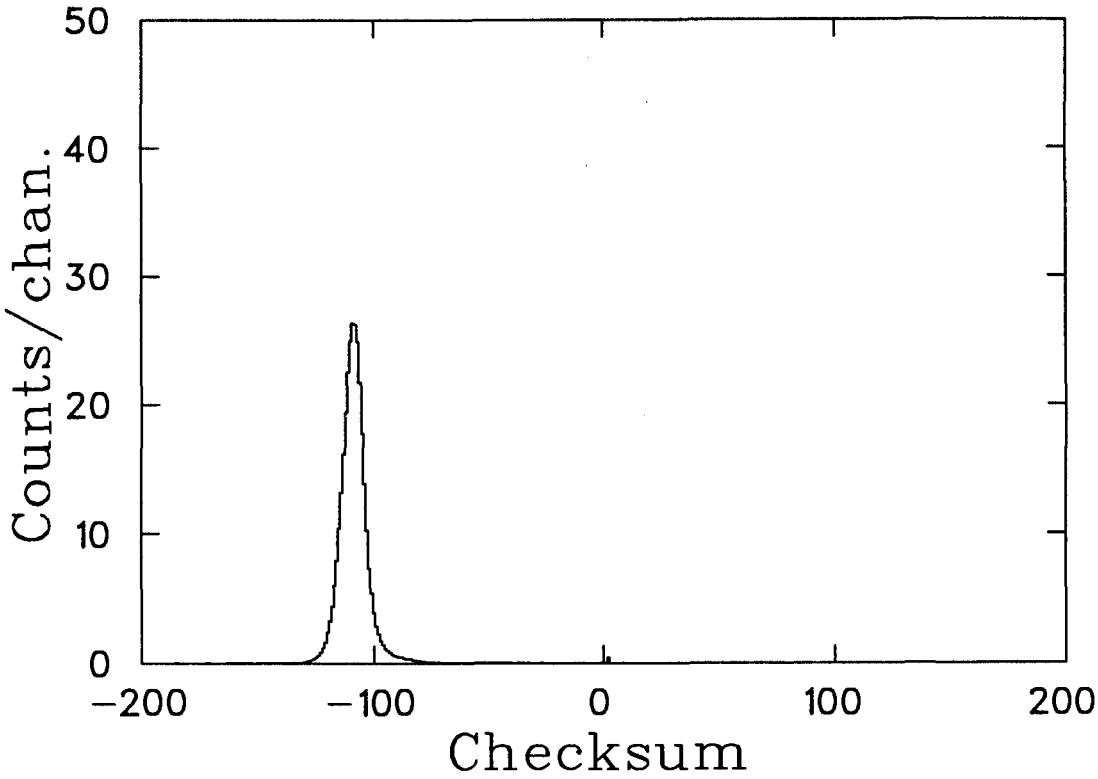

Figure 4.6: Checksum spectrum for wire chamber WC3.

wire chamber coordinates X_3 and X_4 the focal plane position X_F is defined as

$$X_F = \frac{X_4 \cdot D34 + [(D34 - F) \cdot (X_3 + H_{off} - X_4)]}{D34 - (X_3 + H_{off} - X_4) \cdot tan\delta} \tag{4.12}$$

where the parameters F and δ are determined using ^{12}C elastic scattering data taken at three magnetic field settings. Elastically scattered pions from a ^{12}C target have a momentum which does not depend significantly on the horizontal scattering angle, θ, over the $\sim 6°$ horizontal angular acceptance limit imposed by gates on the

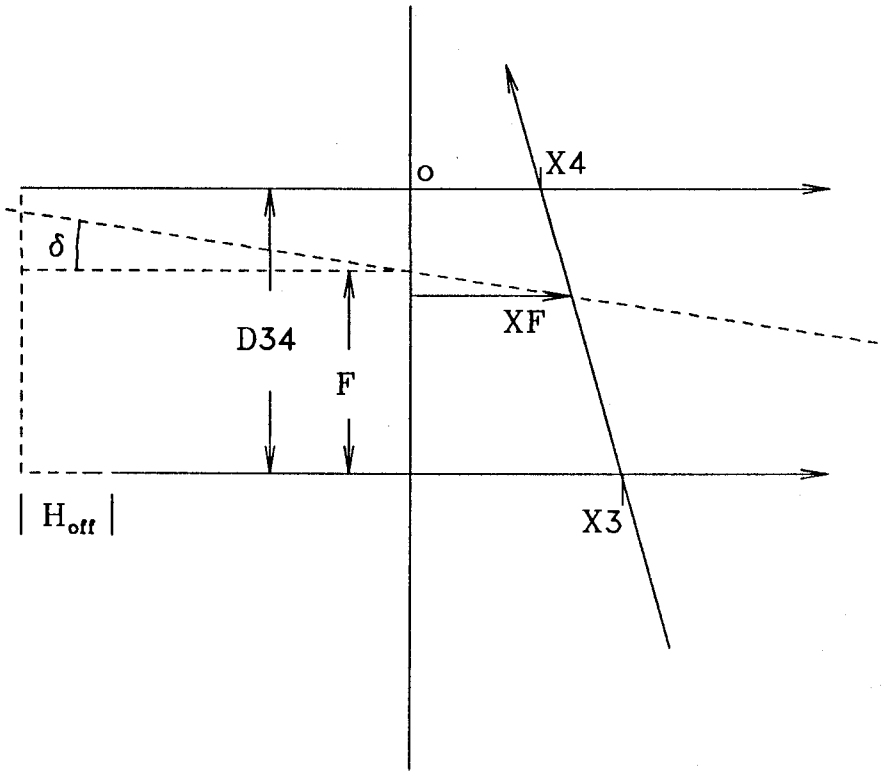

Figure 4.7: The QQD focal plane determination

θ coordinate. Since X_F is proportional to the momentum of the scattered pions, it should be angle independent also. The spectrometer focal plane is determined by first setting $\tan\delta$ to zero and then adjusting the parameter F until X_F is observed to be independent of θ. Once F has been determined for several values of X_F, the tilt angle (δ) can be calculated. It is a simple matter to then determine the value of F corresponding to $X_F = 0$. For the QQD with no quadrupoles the values of these parameters are F = 234mm and δ = -60.2°. This precise focal plane only exists for scattered pions which come from a point source (a thin target) and exhibit negligible momentum spread over the range of scattering angles accepted by the spectrometer. The pions scattered from ^{3}He have a significant momentum

spread over the horizontal scattering angle (θ) and vertical scattering angle (ϕ). This dependence is corrected for up to second order in θ and only in second order in ϕ since the range of ϕ is centered on 0. A correction was also made for the target postion V_z at which the pion originated. The corrected focal plane coordinate is given as

$$PCX_F = A \cdot \theta + B \cdot \theta^2 + C \cdot \phi^2 + D \cdot V_z$$

where the parameters A-D were determined empirically.

Elastic π-P scattering was measured at several angles from 50° to 110° to provide both a momentum calibration of the focal plane and an acceptance vs. X_F profile. The momentum calibration assumes that the focal plane coordinate is linear in momentum i.e. p = A * X_F + B. The values of the parameters are A = 0.236 and B = 178.7. The acceptance scan is used for normalization of the ^{3}He cross sections and is discussed in the following section.

4.2.4 QQD Acceptance Correction

The acceptance correction applied to our data comes from measuring π-P elastic cross sections and comparing them to previous and, hopefully, more accurate data. This is done because spectrometers in general do not have a constant angular acceptance over the full range of momentum acceptance. In this experiment the ^{3}He data were measured at a constant QQD magnetic field. As the scattering angle was increased the momentum of the scattered pions decreased and the data therefore cover a range of momentum or X_F. Several factors that go into a cross section calculation were previously discussed (see section 3.2.2); however there are some additional corrections that need to be applied some of which have been previously alluded to. The πP cross sections used for comparison come from the Arndt phase shift solution SM89. Table 4.1 lists the measured cross section values, the interpolated phase shift cross sections (σ_{said}) and the corresponding acceptance factors.

Since the focal plane positions of the ^{3}He elastic peaks do not coincide with

Table 4.1: QQD π-P cross sections and acceptance factors

θ_{lab} (deg.)	X_F (mm)	Momentum (MeV/c)	$\sigma_{exp.}$ (lab) (mb/sr)	$\Delta\sigma$ (mb/sr)	σ_{said} (lab) (mb/sr)	A. Factor	ΔA
50	65.	193.31	11.34	1.0	14.6	.777	0.062
50	-5	178.22	3.19	.38	3.43	.93	.11
70	-56	165.91	3.11	.37	2.94	1.06	.12
90	-103	153.45	3.33	.40	3.69	.902	.11
106	-145	144.4	3.68	.44	4.64	.793	.10

those for πP scattering, a quadratic function was fit to the acceptance data from πP scattering. This function was used to get the acceptance correction for an arbitrary focal plane postion XF. A plot of the data and the fitted function are shown in Fig. 4.8. The function used to fit the data points was $Acc = A + B(XF + C)^2$ where the parameter values are A = 1.004 $\pm$ 0.04, B = (-2.0 $\pm$ 0.5) $\times$ 10^{-5} and C = 42 $\pm$ 7.0.

4.2.5 QQD Efficiency

The efficiency calculation for particles travelling through the QQD is very similar to the calculations presented in chapter 3, section 3.2.1 for protons going through the MRS. As for the MRS, it is assumed that chambers in close proximity may have correlated missing or multiple events. However, the beam chambers, the front end chambers (FEC's) and the focal plane chambers are assumed to be independent groups. The overall efficiency ϵ is then $\epsilon = \epsilon_{BEAM} \cdot \epsilon_{FEC} \cdot \epsilon_{BACK}$ where ϵ_{BACK} is the combined efficiency of wire chambers WC3 and WC4.

Since the number of hits in a given wire plane is recorded for the FEC and BEAM chambers, the efficiency calculation for these groups of chambers proceeds as given in chapter 3. Currently there is no software masking enabled for these chambers so the OUT condition (a valid hit outside a specified region of the wire plane) does

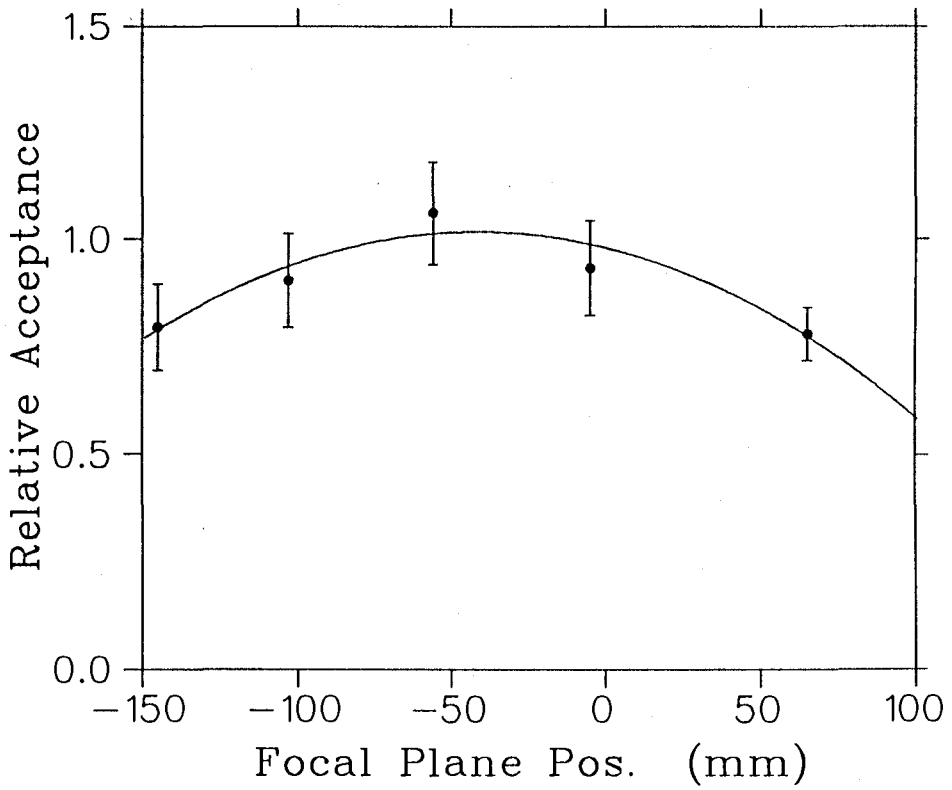

Figure 4.8: The QQD acceptance as a function of focal plane position.

not exist. The focal plane chambers, WC3 and WC4, are of different construction than the FEC and BEAM chambers as explained in section 4.2.3. Since one does not know the number of hits that occured in each chamber, a slightly different procedure is used to obtain this component of the efficiency.

The representative sample for all efficiency calulations is based on the minimal condition PION = E1 · E2 · E3 · (Y1 + Y2) · B1 which is similar to the basic trigger

condition with the addition of software gates on the time of flight and energy loss in scintillators E1, E2 and E3. These cuts ensure that the particles being considered are pions although there was very little background from other particles (pions decaying into muons etc.). Other conditions which will be used to illustrate the efficiency calculation are FEC, BEAM and BACK which indicate that the event provided a valid single track in all FEC planes, beam wire planes or back end wire planes, respectively.

The total efficiency for WC3 and WC4 is obtained by observing how many events satisfy the condition PION · FEC · BEAM and then observing how many events are lost when the back end wire chambers are also included. The efficiency is given by

$$\epsilon_{BACK} = \frac{\text{PION} \cdot \text{FEC} \cdot \text{BEAM} \cdot \text{BACK}}{\text{PION} \cdot \text{FEC} \cdot \text{BEAM}} \tag{4.13}$$

For the FEC and in-beam chambers we first determine the ineffeciency of the chamber and then subtract it from 1 to get the efficiency. A calculation of ϵ_{FEC} will provide an example. A representative sample is defined as $NOFEC = PION \cdot BEAM \cdot BKWC$ which contains a good event in all chambers *except* the FEC chambers. Another condition is defined which represents the subset of events that gave missing or multiple hits in any of the FEC planes, i.e. $MMFEC = (MISFEC + MULFEC) \cdot NOFEC$. Here MISFEC and MULFEC indicate a missing and multiple event, respectively, in any FEC plane. The efficiency is then $\epsilon_{FEC} = 1 - MMFEC/NOFEC$. It should be noted that missing events in the FEC-X planes were not included in either the representative sample or the subset. Multiple events in these planes were included however. The wires of the FEC-Y planes span the full range of X, overlapping with uninstrumented portions of the X planes. Since it was the Y planes that were in the trigger, a significant number of good event triggers register as missing in X1 or X2. This can occur because the QQD horizontal angular acceptance was larger than that defined by the instrumented portion of the X-planes. Since these missing events are due simply to the geometry and choice of trigger condition they do not represent the actual probabil-

ity of detection for a particle passing through the active area. This would lead to an underestimate of the true efficiency. The true inefficiency of the X planes due strictly to missing events is probably well approximated by the value measured for the Y planes however. For a given plane this value is ~2%.

The general difficulties associated with calculating wire chamber efficiencies where extended targets are used were discussed is chapter 3. In this experiment there is an additional problem due to the fact that the large size of the pion beam creates a large background from pions scattered by the cell walls. Although the intensity of the beam is down by at least a factor of ten where the radial distance from the beam axis coincides with the walls of the cell, the cell walls contain ~ 1000 times as many atoms/cm^2. Therefore most of the triggers come from events originating in the endcaps and walls of the cell rather than in the ^{3}He. It may be impossible to calculate an accurate wire chamber efficiency using data taken with the ^{3}He target in the current configuration. At the beam rates used during E557 one expects about 5% of the beam pulses to contain 2 pions or more. This should show up as an inefficiency of about 10% since two pions are twice as likely to cause a trigger. In a typical ^{3}He run however, the beam chamber inefficiency due to multiple hits is about 50%. Furthermore, these multiple events show a high degree of correlation in the beam chambers, indicating that they originate from beam bursts which actually contain two pions.

The size of the scintillator B1 was chosen to limit the active cell area to that of the helium and thus exclude most pions that would have scattered in the glass side walls. The number of triggers is biased by beam pulses in which one pion hits the scintillator and one passes by it, striking the glass wall. Most of the triggers resulting from these events come from scattering in the glass wall since the pion incident on the glass wall is a factor of ~ 1000 more probable to scatter assuming that the glass and ^{3}He cross sections are about equal. The inefficiency generated from these multiple events is thus not an accurate measure of the probability of

detecting a single particle that has passed through the system.

The above hypothesis comes from comparing the efficiencies realized during runs with a CH_2 target to those with the ^{3}He target. Although the beam rates, wire chamber rates, and event rates were comparable in the two cases, the efficiency (as calculated above) was about a factor of 1.8 lower for the ^{3}He data. Since the elementary $\pi - p$ cross sections, extracted from the CH_2 data using the above efficiency calculation, were accurate to within $\pm$ 10% when compared to previous measurements, one may conclude that the CH_2 target efficiencies are better representative of the true values even for the ^{3}He data. Further evidence is the reasonable agreement between the ^{3}He cross sections measured here and the accurate cross sections of Källne *et al.*[67].

The absolute efficiencies are only important for the cross section measurements The asymmetry measurements are only sensitive to efficiency differences between data sets. The efficiencies for the ^{3}He data remained essentially constant (although wrong in magnitude) for all of the runs. This is expected since the running conditions (beam rate and beam steering) were stable. An error in the overall magnitude of the efficiency would have little effect on these results.

4.2.6 Calculation of the Cross Section and Spin Observables

The expression used to calculate the cross section for elastic proton scattering was given in section 3.2.2. One must make several corrections to raw yields to obtain the number of scattered pions however. The number of scattered pions N_{scat} is determined from the number that were measured by

$$N_{scat} = \frac{N_{meas}}{lt \cdot Acc \cdot \epsilon \cdot ms \cdot sf \cdot cor_{beam}} \tag{4.14}$$

where lt is the computer livetime which was typically about 0.85, Acc is the acceptance correction and ϵ is the total wire chamber efficiency (typically $\sim$ 0.4 - 0.5). ms is a correction for events lost due to multiple scattering. This is the fraction of events whose vertex could be located to within 3 mm with the additional constraint

that the vertical scattering angles for pions entering the QQD and those exiting the QQD be approximately the same. The pion survival fraction over the 1.6 meter flight path from FWC2 to WC4 is sf. For pions scattered from hydrogen at an angle of 50° the time of flight over this distance is about 5×10^{-9} s. The pion mean lifetime $\tau = 26$ ns implies a pion survival fraction $e^{-5/26} = 0.83$. It is assumed that all pions which decay prior to FWC2 will be eliminated by the traceback and those which decay after WC4 will still be detected in the scintillators. Obviously some pion decays will be accounted for in the multiple scattering corrections. Since this experiment was not intended to determine accurate absolute cross sections, we rely on the normalization provided by previous cross section measurements to indicate whether the above assumptions are reasonable. The final correction was the beam charge correction cor_{beam} which was discussed in section 4.2.1.

Only statistical uncertainties are assumed for the above corrections. They are typically small and amount to $\sim$ 1%. A systematic uncertainty of $\pm$8% is assumed for the pion survival fraction however, which corresponds to the difference between the flight time from WC2 to WC4 and that from the target to WC4 although this is probably a generous upper limit. The uncertainty in the CH_2 areal density which is included in the error estimate of the acceptance correction is about 2%. The statistical uncertainties for the CH_2 measurements are typically about 5%. The overall uncertainty in the acceptance correction, including a 4% uncertainty in the solid angle Ω, is then typically 10 - 11%. The uncertainty in the ^{3}He cross section measurements would then be identical to this. However, in this case there is a larger error contribution from counting statistics. A small background under the ^{3}He elastic peak combined with fewer overall events results in the increased statistical uncertainty. Due to the problems with the efficiency calculation when using the ^{3}He target, an overall systematic uncertainty of 25% is applied to the ^{3}He cross sections.

The target polarization produced by the Fermi contact hyperfine interaction

during Rb–^{3}He spin exchange collisions could be reversed and analyzed by adiabatic fast passage NMR. The NMR signal induced by the rotating ^{3}He magnetic moment was compared to that from a water sample of similar geometry to obtain an absolute value of the polarization. Because of the weakness of water signal (it is smaller than the ^{3}He signal by a factor of $(3.71 \times 10^4)\ p\ \mathrm{P}$ where p and P are the ^{3}He pressure and polarization, respectively). Corrections for a significant temperature dependence in the induced NMR signal ($\sim$ 8%) were applied. A systematic uncertainty of $\Delta P_t/P_t$=0.07 has therefore been adopted for the absolute ^{3}He polarization. This uncertainty is included in the overall systematic uncertainties for A_y quoted in Table 4.3.

Normalized yield spectra for target spins up ($\sigma_\uparrow$) and down ($\sigma_\downarrow$) taken at $\theta_{lab} = 80°$ are shown in the upper two frames of Fig. 4.9. The ^{3}He elastic peak has a width of about 3 MeV FWHM which arises mostly from the energy spread of the incident beam, with a small contribution from multiple scattering in the various detector and target elements. The target polarization labels ($\uparrow$ and $\downarrow$) refer to a coordinate system in which the scattered pions are detected on the left side of the beam. The difference spectrum is shown in the bottom frame of Fig. 4.9. Since this difference is proportional to the analyzing power

$$A_y \approx \frac{1}{P_t}\frac{\sigma_\uparrow - \sigma_\downarrow}{\sigma_\uparrow + \sigma_\downarrow} \tag{4.15}$$

one can conclude that the background is either unpolarized or has an analyzing power close to zero. The systematic uncertainties quoted in Table 4.3 include the uncertainty from subtraction of this small background. To reduce systematic uncertainties due to long term fluctuations of the target polarization, data were obtained in 3 hour sets with polarization measurements between each set. The polarization was reversed every 12 hours. Therefore several data sets were obtained for each angle and polarization state. This results in an overdetermined set of equations from which the asymmetry and cross section were extracted by a least squares

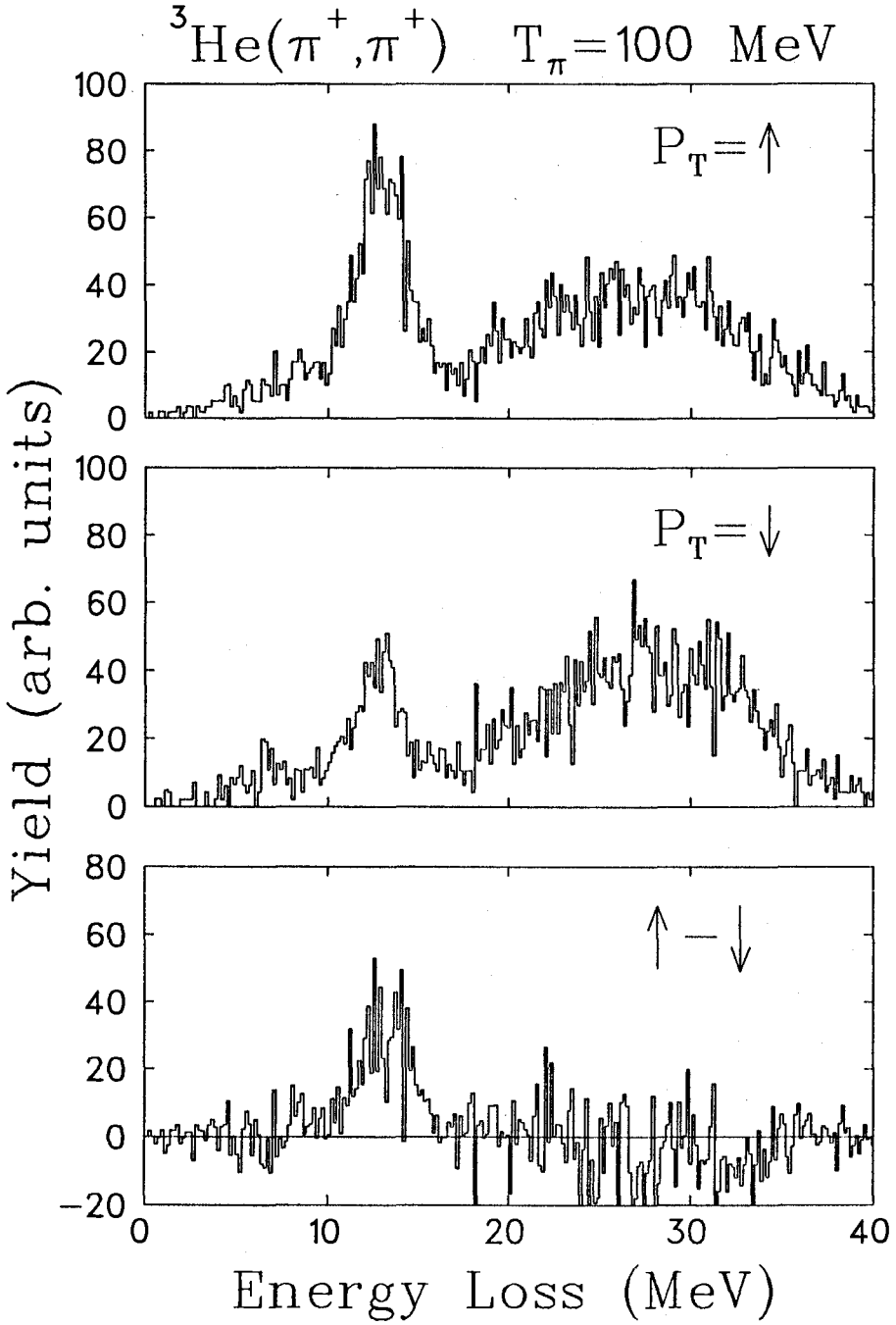

Figure 4.9: Normalized yields vs. energy loss for the two target spin projections. The difference of the two is shown in the bottom frame.

minimization of the function

$$\chi^2 = \sum_i \frac{(\sigma_i - \sigma_o(1 + A_y P_{t_i}))^2}{(\Delta\sigma_i)^2} \ . \tag{4.16}$$

Here, σ and σ_o are the measured polarized and unpolarized cross sections, respectively, P_t is the target polarization, A_y is the analyzing power, and the sum is over individual data sets i. The results are presented in Table 4.2 with the first error arising from counting statistics and the second from systematic uncertainties.

4.3 Theoretical Description of π-^{3}He Scattering

The measured experimental cross sections and asymmetries are compared to two different models. The full DWIA calculation employs realistic three-body wave functions for the initial and final states. This nuclear wave function has been obtained by solving the Faddeev equations with the Reid potential as the NN interaction[43]. Pion nucleus scattering is then treated in the framework of multiple scattering theory (see Appendix A) in which the π-^{3}He scattering matrix $T(E)$ is given as a solution of the Lippmann–Schwinger equation [68]

$$T(E) = V(E) + V(E)G(E)T(E) \tag{4.17}$$

where $G(E)$ is the pion-nucleus Green's function or propagator. This equation is solved in momentum space where dependence on the target nucleon momenta is retained. It therefore takes the Fermi motion of nucleons inside the ^{3}He nucleus into account and treats nonlocalities exactly[41]. The potential matrix $V(E)$ is related to the free π-N t-matrix and represents a first order optical potential. A second order term can in principle be added to $V(E)$ which represents true pion absorption and higher order processes[68]. Such a phenomenological term was developed for heavier nuclei, however its effects are shown to be small[69] for pion scattering and charge exchange on ^{3}He.

The full DWIA calculation is compared to a schematic model[70] in which the

Table 4.2: Cross sections and analyzing powers for 100 MeV π^+-^{3}He elastic scattering.

$\theta_{c.m.}$ (degrees)	$(d\sigma/d\Omega)_{c.m.}$ (mb/sr)	A_y
64.0	1.8 ± 0.08± 0.45	0.04 ± 0.09 ± 0.02
84.6	0.7 ± 0.04± 0.18	0.89 ± 0.12 ± 0.10
104.5	2.1 ± 0.06± 0.53	0.38 ± 0.06 ± 0.04

π^+- ^{3}He non-spin-flip (J=0) and spin flip (J=1) amplitudes are given by

$$\tilde{F} = (2f_{\pi^+p} + f_{\pi^+n})F_{J=0}(Q^2) \quad (4.18)$$

$$\tilde{G} = g_{\pi^+n}F_{J=1}(Q^2) \quad (4.19)$$

where $f_{\pi^+p,n}$ are the elementary π-N amplitudes[71] and the proton spins are assumed to be coupled to zero. At the momentum transfer range sampled here it is a good approximation to assume $F_{J=0}(Q^2) = F_{J=1}(Q^2) = e^{-r_o^2Q^2/6}$ with $r_o = 1.65$ fm. Note that the elementary πN amplitudes have been transformed from the πN c.m. system to the π-^{3}He c.m. system resulting in an angular shift of about 10° lower in scattering angle.

4.4 Experimental Results and Comparison with Theory

Measured angular distributions of $d\sigma/d\Omega$ and A_y for π^+-^{3}He elastic scattering at 100 MeV are presented in table 4.2 and shown in Fig. 4.10 along with accurate cross section data[67] of Källne *et al.*

The error bars shown are the larger of either systematic or statistical errors. The data are compared to the full DWIA calculation (solid curve) and the schematic model (dashed curve). Both calculations produce similar results and, aside from an apparent angular shift, are in fair agreement with the data. The calculations

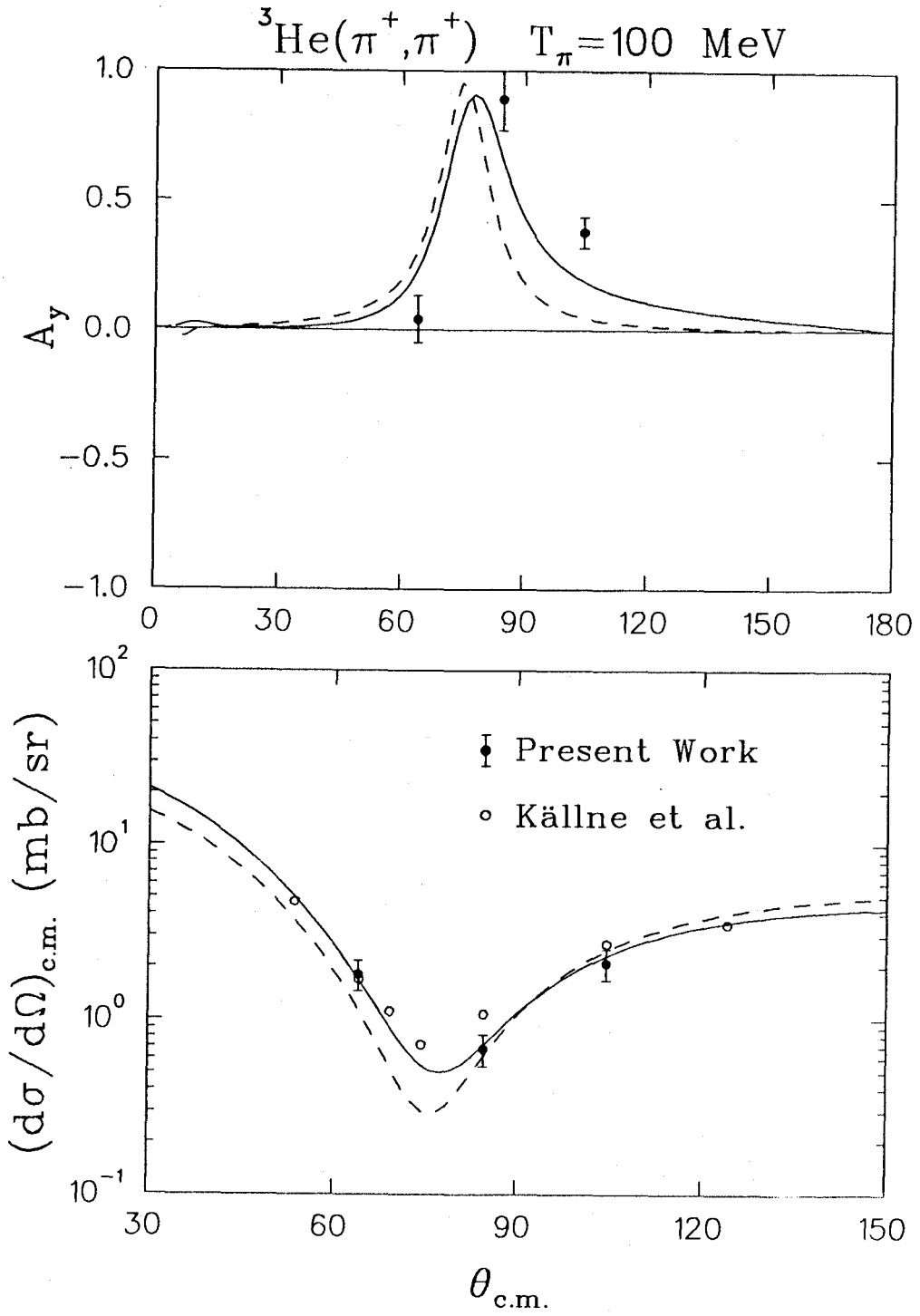

Figure 4.10: A_y (top) and cross section (bottom) angular distributions for the reaction $^3\vec{\text{He}}(\pi^+, \pi^+)^3$He at 100 MeV. The data are compared to a full DWIA calculation (solid curve) and a schematic model (dashed curve).

predict the large A_y values observed experimentally, however the schematic model fails to reproduce the cross section in the region of the minimum. In addition to the full DWIA and the schematic model, calculations were performed in the DWIA using only the S-state component of the tri-nucleon wave function. The results are nearly the same as those of the full calculation as can be seen in Fig. 4.11. A large asymmetry is also predicted by the momentum-space optical model of Landau[39] who used electromagnetic form factors to construct the required charge and spin densities in ^{3}He.

Interpretation of the measurements is straightforward within the context of the simple model presented here (Eqs. 4.17 and 4.18). The following discussion refers to the amplitudes $\tilde{F}$ and $\tilde{G}$ displayed in Fig. 4.12. Since the non-flip elementary amplitudes are p-wave dominated, both the real and imaginary parts go through zero at about 90°. They go through zero at different angles however, since they are not entirely p-wave in nature. As a result, $|f|$ is never equal to zero. Constructing the π^+-^{3}He amplitudes using Equations 5 and 6 (shown in Fig. 4.12) one finds that Re($\tilde{F}$) and Im($\tilde{F}$) cross zero near 80° and 100°, respectively. One also finds that $\tilde{F}$ and $\tilde{G}$ are of comparable magnitude over this angular region. The only other requirement for a large asymmetry is that $\tilde{F}$ and $\tilde{G}$ be $\sim$ 90° out of phase when they are of roughly equal magnitude since $A_y = 2Im\{fg^*\}/\sigma$. The data indicate that these conditions are obviously met for the π^+-^{3}He system.

Although the schematic model explains the existence of a large A_y near the cross section minimum, the full calculation is in better agreement with the data, especially at angles greater than 90°. This is a clear indication that details in the reaction model are important at this energy. The discrepancy between the two models can be traced to the imaginary part of g. It is this enhanced sensitivity of A_y to the spin-flip amplitude that makes asymmetry measurements valuable.

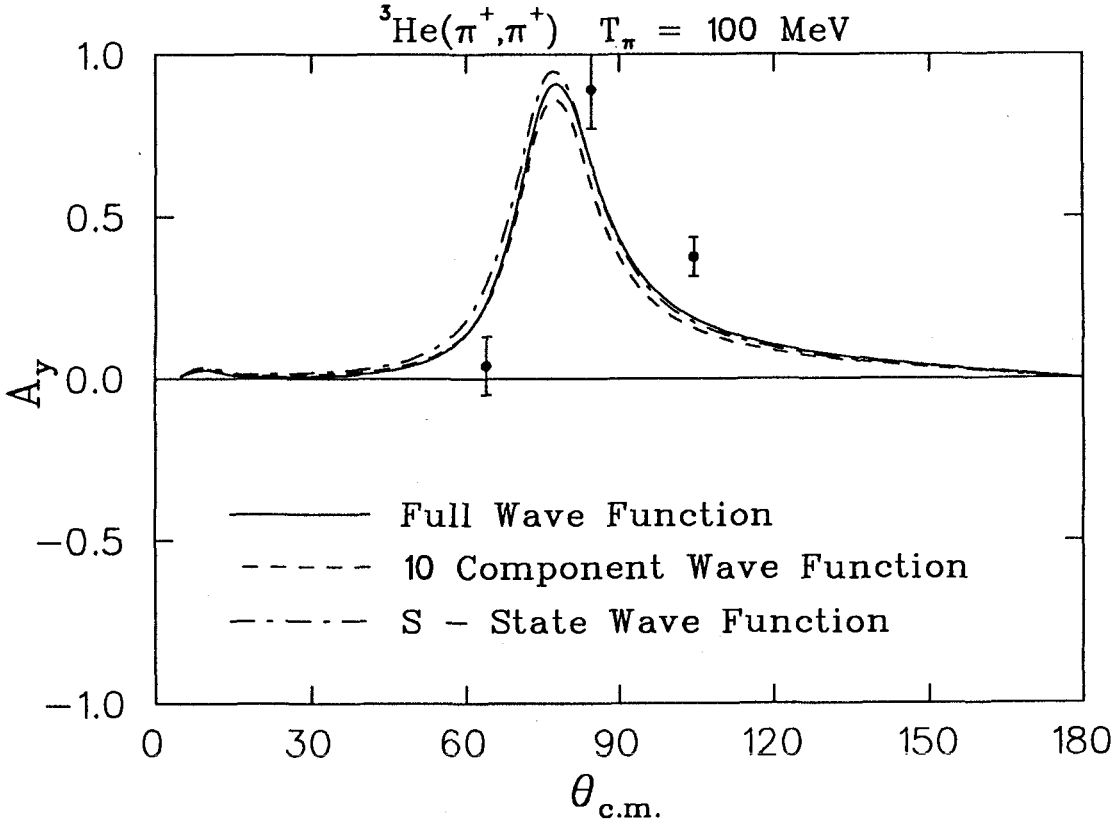

Figure 4.11: A_y compared to the full DWIA calculations outlined in the main text. The effect of including only certain components of the Faddeev wavefunction is indicated by the three curves.

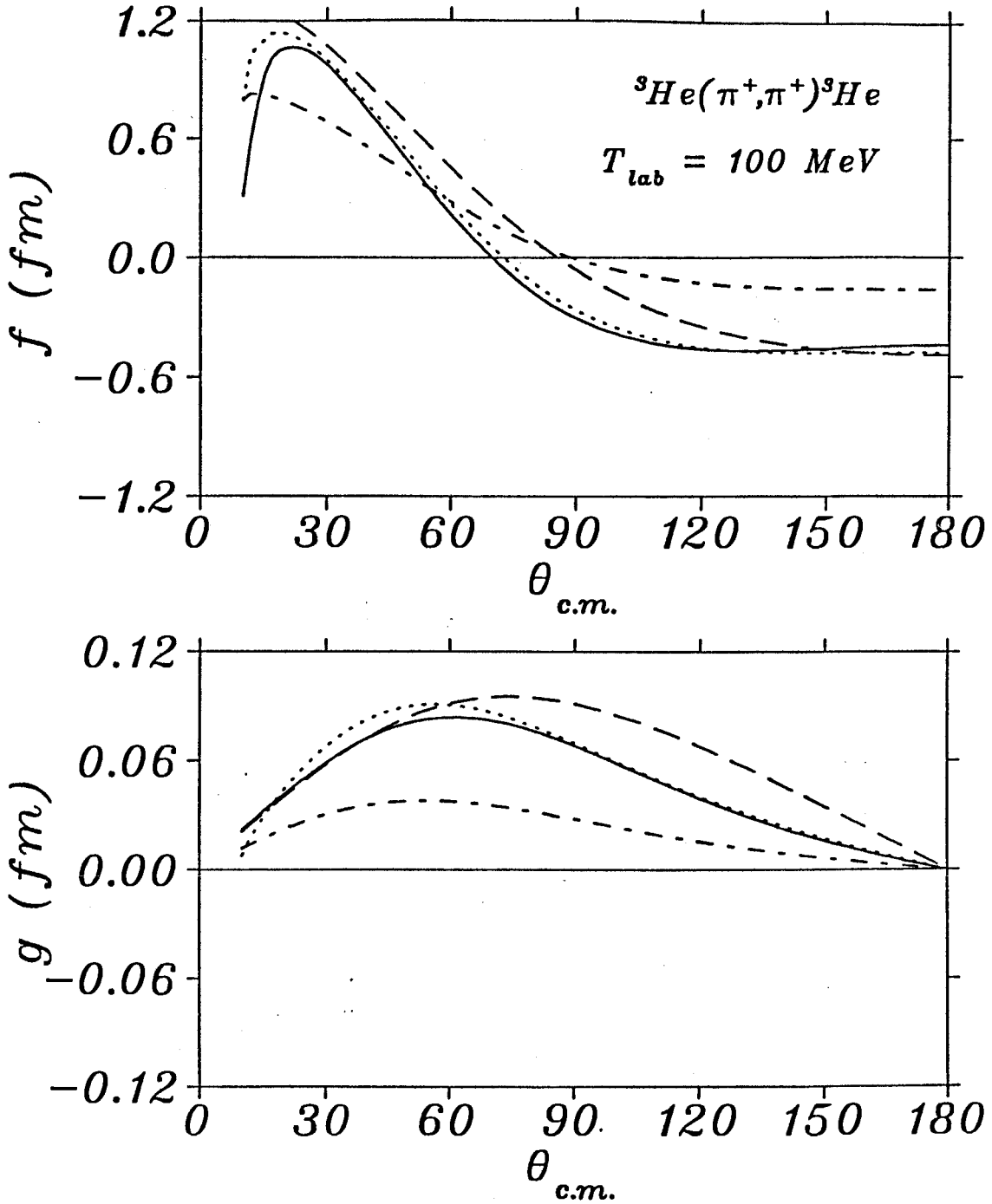

Figure 4.12: Calulations of the spin-flip (f) and non-flip (g) amplitudes. The real (imaginary) part of the amplitude in the simple model is depicted by the dotted (dashed dotted) curve. The real (imaginary) part of the amplitude in the DWIA calculation is given by the solid (dashed) curve.

Chapter 5

Summary and Conclusions

In conclusion, we have developed a high density polarized ^{3}He gas target which has been used successfully in nuclear scattering studies at TRIUMF. The high density and polarization achieved in these targets has made such experiments feasible and has also permitted a study of the optical pumping process at buffer gas pressures several times higher than were previously possible.

Polarized ^{3}He targets of relative density p = 3–12 atmospheres have been built and tested. Transmission data with linearly polarized light near the Rb D1 frequency have been analyzed to determine the pressure broadened lineshape (shift, width and asymmetry) and the Rb number density. Transmission data with circularly polarized light contain evidence for a strong increase of the Rb spin destruction rate with pressure although the mechanism which provides the quadratic dependence is highly speculative. It should be noted that the apparent spin destruction rate can be influenced by the depolarizing effect of fluorescent photons which can be substantial at high power levels. This is not included in the optical pumping model described in chapter 2. The laser power required to achieve 96% Rb polarization has been estimated for a variety of pressures and geometries. Whereas the pressure broadening has only a minor effect on the required laser power the strong increase of Γ_{SD} with ^{3}He pressure necessitates a large increase in laser power. It is thus unfavorable to optically pump Rb vapour at high ^{3}He density.

The rate for Rb–^{3}He spin exchange was measured and found to be significantly

lower than previously determined values. Maximum ^{3}He polarizations of 0.72-0.79 were observed at pressures p = 6–9 atmospheres. These polarization values are 85-90 % of the theoretical upper limits calculated for idealized conditions.

The subject of one of the first experiments to use this polarized ^{3}He target was elastic scattering of polarized protons by polarized ^{3}He at intermediate energies. Cross section and analyzing powers for which there were previously existing data, are fairly well reproduced by a momentum space microscopic optical model calculation which is free of adjustable parameters. The newly measured observable A_{OOON} differs substantially from the beam related asymmetry A_{OONO} which is unambiguous evidence of a large f amplitude even though this amplitude must vanish for the NN system. Agreement between theory and experiment is poor for both of the asymmetries A_{OOON} and A_{OONN} which are sensitive to parts of the $p-^3He$ scattering amplitude untested by previous experiments. At 500 MeV the data are compared to two models one of which has no adjustable parameters and one which has had the densities adjusted to reproduce the cross section and analyzing power data. The latter model clearly improves the agreement between theory and experiment however this is likely a result of the phenomenological adjustment of some of the relevant p-^{3}He scattering amplitudes.

The first measurement of A_y in elastic pion scattering from polarized ^{3}He has also been presented. The results are in contrast to the rather small asymmetries observed in recent measurements with polarized targets[1,2] of ^{13}C and ^{15}N. In the π-^{3}He system several different models predict large asymmetries and, furtheremore, show a distinct lack of sensitivity to nuclear structure details. The magnitude of the asymmetry has been understood in terms of a very simple model. However, inclusion of multiple scattering and absorption in the reaction model significantly improves the agreement with experiment.

Calculations for π^--^{3}He scattering yield similar agreement between the two models, however the analyzing powers are predicted to be only about half as large. An

experiment to measure the asymmetry for π^- scattering at 100 MeV is planned at TRIUMF. It will also be of interest to study the energy dependence of the π-^{3}He interaction. At energies above the Δ-resonance the full calculation predicts large negative values of A_y whereas in the schematic model this change of sign across the resonance is *not* predicted. This is an indication that multiple scattering and absorption effects are more important at the higher energies.

References

[1] M. Leduc, Coll. de Physique **51**, Suppl. C6-317 (1990).

[2] J.L. Friar, B.F. Gibson, G.L. Payne, A.M. Bernstein, and T.E. Chupp, Phys. Rev. C**42**, 2310 (1990).

[3] C.E. Woodward *et al.*, Phys. Rev. Lett. **65**, 698 (1990).

[4] K.P. Coulter, A.B. McDonald, W. Happer, T.E. Chupp, and M. Wagshul, Nucl. Instr. Meth. A**288**, 463 (1990).

[5] R.T. Johnson, D.N. Paulson, R.P. Giffard, and J.C. Wheatley, J. Low Temp. Phys. **10**, 35 (1973).

[6] F.D. Colegrove, L.D. Schearer and G.K. Walters, Phys. Rev. **132**, 2561 (1963).

[7] R.G. Milner, R.D. McKeown and C.E. Woodward, Nucl. Instr. Meth. A**274**, 56 (1989).

[8] M.A. Bouchiat, T.R. Carver, and C.M. Varnum, Phys. Rev. Lett. **5**, 373 (1960).

[9] R.L. Gamblin and T.R. Carver, Phys. Rev. **138**, 964 (1965).

[10] R.M. Herman, Phys. Rev. A **137**, 1062 (1965).

[11] B.C. Grover, Phys. Rev. Lett. **40**, 391 (1978).

[12] C.H. Volk, T.M. Kwon and J.G. Mark, Phys. Rev. A**21**, 1549 (1980).

[13] N.D. Bhaskar, W. Happer, and T. McClelland, Phys. Rev. Lett. **49**, 25 (1982).

[14] N.D. Bhaskar, W. Happer, M. Larsson and X. Zeng, Phys. Rev. Lett. **50**, 105 (1983).

[15] W. Happer, E. Miron, S. Schaefer, D. Schreiber, W.A. van Wijngaarden and X. Zeng, Phys. Rev. A**29**, 3092 (1984).

[16] X. Zeng, Z. Wu, T. Call, E. Miron, D. Schreiber and W. Happer, Phys. Rev. A**31**, 260 (1985).

[17] T.E. Chupp, M.E. Wagshul, K.P. Coulter, A.B. McDonald and W. Happer, Phys. Rev. C**36**, 2244 (1987).

[18] M.E. Wagshul and T.E. Chupp, Phys. Rev. A**40**, 4447 (1989).

[19] K.M. Watson, Phys. Rev. **89**, 575 (1953).

[20] A.K. Kerman, H. McManus, and R.M. Thaler, Ann. Phys. **8**, 551 (1959).

[21] H. Fiedeldey, Nucl. Phys. **A463**, 335 (1986).

[22] J.P. Svenne, private communication.

[23] M.J. Paez and R.H. Landau, Phys. Rev. C**29**, 2267 (1984); R.H. Landau, M. Sagen and G. He, Phys. Rev. C**41**, 50 (1990).

[24] L. Ray and G.W. Hoffmann, Phys. Rev. C**31**, 538 (1985); L. Ray, G.W. Hoffmann, M.L. Barlett, J.D. Lumpe, B.C. Clark, S. Hama and R.L. Mercer, Phys. Rev. C**37**, 1169 (1988).

[25] J. Bystricky, F. Lehar and P. Winternitz, J. Phys. (Paris) **39**, 1 (1978).

[26] P. La France and P. Winternitz, J. Phys. (Paris) **41**, 1391 (1980).

[27] D.K. Hasell *etal.*, Phys. Rev. C**34**, 236 (1986).

[28] G.D. Alkhazov *etal.*, Phys. Lett. B**85**, 43 (1979).

[29] G.W. Hoffmann *etal.*, submitted to Phys. Rev. Lett.

[30] Yi-Fen Yen *et al.*, Phys. Rev. Lett. **66**, 1959 (1991).

[31] R. Tacik *et al.*, Phys. Rev. Lett. **63**, 1784 (1989).

[32] B. Larson *et al.*, Phys. Rev. A**44** (1991), in press.

[33] R.H. Landau, S.C. Pathak and F. Tabakin, Ann. Phys. **78**, 299 (1973).

[34] R.H. Landau and A.W. Thomas, Nucl. Phys. A**302**, (1978) 461.

[35] M. Wakamatsu, Nucl. Phys. A**340**, 280 (1980).

[36] D.J. Ernst, in *Proceedings of the LAMPF Workshop on Physics with Polarized Targets, Los Alamos, New Mexico, 1986*, (LANL Report No. LA-10772-C, 1986), p.129.

[37] R. Mach and S.S. Kamalov, Nucl. Phys. A**511**, 601 (1990).

[38] R. Mach, Nucl. Phys. A**258**, 513 (1976).

[39] R.H. Landau, Phys. Rev. C**15**, 2127 (1977).

[40] F.M.M. Van Geffen *et al.*, Nucl. Phys. A**468**, 683 (1987).

[41] S.S. Kamalov, L. Tiator and C. Bennhold, Few Body Systems (in press).

[42] R.S. Hicks *et al.*, Phys. Rev. C**26**, 339 (1982).

[43] R.A. Brandenburg, Y.E. Kim, A. Tabis, Phys Rev C**12**, 1368 (1975).

[44] G.G. Ohlsen, Rep. Prog. Phys. **35**, 717 (1972); G.G. Ohlsen and P.W. Keaton Jr., in 2^{nd} *Int. Conf. on Polarized Targets*, ed. by G. Shapiro, (Lawrence Berkeley, 1971), LBL-500, pp. 367-9.

[45] G. Fournier *et al.*, Nucl. Phys. A**426**, 542 (1984).

[46] J. Källne *et al.*, Phys. Rev. Lett. **45**, 517 (1980).

[47] W. Demtröder, *Laser Spectroscopy* (Springer–Verlag, Berlin, Heidelberg, 1981), pp. 79 – 111.

[48] A. Gallagher, in *Proceedings of the Fourth International Conference on Atomic Physics, Heidelberg, 1974*, edited by G. zu Putlitz, E.W. Weber, and A. Winnacker (Plenum Press, New York, 1975), pp. 559-574.

[49] TRIUMF Annual Report 1989, pp. 73–74 (unpublished).

[50] L. Krause, in *The Excited State in Chemical Physics* (Wiley, New York, 1975), pp. 267-316.

[51] O. Häusser *et al.*, to be published.

[52] A. Abragam, in "The Principles of Nuclear Magnetism", Oxford University Press, (1961).

[53] F. Block, W.W. Hansen and M. Packard, Phys. Rev. **70**, 474 (1946).

[54] F. Reif, in "Fundamentals of Statistical and Thermal Physics", McGraw - Hill, (1965).

[55] T.J. Killian, Phys. Rev. **27**, 578 (1926).

[56] S.Y. Ch'en, Phys. Rev. **58**, 1051 (1940).

[57] S.Y. Ch'en and M. Takeo, Rev. Mod. Phys. **29**, 20 (1957).

[58] R. A. Bernheim, J. Chem. Phys. **36**, 135 (1962).

[59] O. Häusser, B. Larson, C. Chan, P. Delheij, TRIUMF Annual Report 1989, pp. 59–61 (unpublished).

[60] R.J. Knize and W. Happer, Bull. Am. Phys. Soc. **30**, 866 (1985); R.J. Knize, Phys. Rev. **A40**, 6219 (1989).

[61] M.A. Bouchiat, J. Brossel, and L.C. Pottier, J. Chem. Phys. **56**, 3703 (1972)

[62] Triumf User's Handbook, unpublished.

[63] R. Abegg, TRIUMF internal report.

[64] K.H. Hicks, MRS User's Manual, unpublished.

[65] S. Hadjimichael *et al.*, Phys. Rev. C**27**, 831 (1983).

[66] R.J. Sobie *et al.*, Nucl. Instr. and Meth. **219**, 501 (1984).

[67] J. Källne, J.F. Davis, J.S. McCarthy, R.C. Minehart, R.R. Whitney R.L. Boudrie, J.B. McClelland, and A. Stetz, Phys. Lett. B**103**, 13 (1981).

[68] M. Gmitro, S.S. Kamalov and R. Mach, Phys. Rev. C **36**, 1105 (1987); M. Gmitro, J. Kvasil, R. Mach, Phys. Rev. C**31**, 1349 (1985).

[69] L. Tiator, C. Bennhold and S.S. Kamalov, to appear in Proc. of the Workshop "Pions in Nuclei", Peniscola, Spain, June 2-9, 1991.

[70] C. Bennhold, B.K. Jennings, L. Tiator and S.S. Kamalov, (submitted to Nucl. Phys.).

[71] R.A. Arndt and L.D. Soper, SAID program, πN scattering solutions.

Appendix A

Multiple Scattering Theory

This appendix is included to provide an overview of the general formulation of multiple scattering theory as presented by Kerman, McManus and Thaler[20] including construction of the microscopic optical potential. Details regarding particular models are provided in the preceding chapters. The starting point for any nonrelativistic scattering theory is the Schrödinger equation. The Hamiltonian appropriate for the N-nucleus problem is

$$H = H_o + V, \qquad H_o = H_N + K_o \tag{A.1}$$

where H_N is the nuclear target Hamiltonian, K_o is the kinetic energy operator for the projectile nucleon and the interaction potential V is the sum of two-body interactions between the incident nucleon (r_o) and each of the target nucleons (r_i),

$$V = \sum_{i=1}^{N} v(r_o, r_i) = \sum_{i=1}^{N} v_i \approx Nv \ . \tag{A.2}$$

where v now represents the interaction between the incident proton and a "typical" target nucleon and hence does not depend on the target nucleon index i.

In general V is treated as a perturbation and the eigenstates used for the per-

turbation expansion are those of the Hamiltonian $H_o = H_N + K_o$ so that

$$H_o\chi_i = E_i\chi_i = E_i\frac{1}{(2\pi)^{3/2}}e^{i\mathbf{k}\cdot\mathbf{r_o}}\Phi_i(r_1,\cdots,r_N) \tag{A.3}$$

where the plane wave is the wavefunction of the incident nucleon and Φ_i are the antisymmetrized eigenstates of the target nucleus including both bound excited states and unbound continuum excited states.

The Schrödinger equation for scattering from the potential V is then $(H_o+V)\psi = E\psi$ or $(H_o - E)\psi = -V\psi$. In integral form the equation becomes

$$\psi = \chi_o + \frac{1}{E - H_o + i\epsilon}V\psi \tag{A.4}$$

where the wavefunction χ_o is the product wavefunction of the incident nucleon and the target ground state. This is usually called the Lippmann - Schwinger equation. If this equation is multiplied by V on the left and the identification of an effective scattering operator $T(E)\chi_o = V\psi$ is made, then equation A.4 takes the form

$$T(E) = V + V\frac{1}{E - H_o + i\epsilon}T(E) \tag{A.5}$$

where the factor $+i\epsilon$ is chosen to satisfy the boundary condition of outgoing scattered waves only. In the momentum space representation this operator equation is explicitly given as

$$\langle n'\mathbf{k}'|\,T\,|\mathbf{k}n\rangle = \langle n'\mathbf{k}'|\,V\,|\mathbf{k}n\rangle + \sum_m \int \frac{d\mathbf{p}\,\langle n'\mathbf{k}'|\,V\,|\mathbf{p}m\rangle\,\langle m\mathbf{p}|\,T\,|\mathbf{k}n\rangle}{E - E_m(\mathbf{p}) + i\epsilon} \tag{A.6}$$

where $E_m(\mathbf{p}) = \varepsilon_m + K_o(\mathbf{p})$. If one assumes completely antisymmetric states for the target nucleus then the matrix element of $v(r_o, r_i) = v$ is independent of the target nucleon label i and equation A.6 can be rewritten

$$T = Nv\left(1 + \frac{1}{\alpha}T\right) \tag{A.7}$$

where the propagator is now

$$\frac{1}{\alpha} = \frac{a}{E - H_o + i\epsilon} \tag{A.8}$$

with a being a projection operator onto antisymmetric nuclear states. Equation A.8 has the first order solution

$$T = Nv \ , \tag{A.9}$$

however one would expect that a better approximation to the transition amplitude would be the sum of actual two-body amplitudes rather than the sum of the bare two body interactions. If one then assumes that the actual two body transition matrix τ is defined in terms of the "bare" NN interaction v by

$$\tau = v\left(1 + \frac{1}{\alpha}\tau\right) \tag{A.10}$$

one can then eliminate the bare NN interaction in equation A.7. It should first be noted that the actual "in medium" two body operator τ is assumed to be closely approximated by the free NN operator t which is a solution of the equation

$$t = v\left(1 + \frac{1}{\beta}t\right) = v\left(1 + \frac{1}{E - K_o - K_1 + i\epsilon}t\right) \tag{A.11}$$

where K_1 is the kinetic energy operator of the target nucleon. This is referred to as the "impulse" approximation. Solving for v in terms of τ and substituting this result into equation A.7 yields the equation

$$T = N\tau\frac{1}{1 - (N-1)\frac{1}{\alpha}\tau} \tag{A.12}$$

or, with the definition

$$T' = \frac{N-1}{N}T \tag{A.13}$$

one obtains the integral equation

$$T' = U_o\left(1 + \frac{1}{\alpha}T'\right) \tag{A.14}$$

where $U_o = (N-1)\tau$. In the lowest order approximation equation A.12 has the solution $T = N\tau$ or, using the impulse approximation, $T = Nt$. Since, elastic scattering is usually the dominant process, it is desireable to separate the above equation into a part which does not involve virtual nuclear excitations and one that

does. If two projection operators P and Q are defined such that P projects onto the target ground state and Q out of it ($P + Q = \mathrm{I}$) then equation A.14 can be solved for the optical potential

$$U = U_o \left(1 + \frac{1}{\alpha} QU\right) \tag{A.15}$$

where all but the first term involve target excitations to intermediate nuclear excited states. Since elastic scattering is the dominant process at low momentum transfer the optical potential is approximated by the first order term

$$U = U^1 = U_{oo} = (N-1)t \tag{A.16}$$

It remains only to express the optical potential U in a specific representation. In momentum space the matrix elements of the optical potential are

$$U^1(k,k') = (N-1)\langle k', \phi_{g.s.}| t |k, \phi_{g.s.}\rangle \tag{A.17}$$

Using the fact that the NN t-matrix acts between the projectile and a given target nucleon and the matrix element does not depend on the target nucleon index, along with the additional approximation that the t-matrix does not depend on the the momentum of the target nucleon but only on the momentum transfer $q = k' - k$, one can write the first order optical potential in the"factorized" form

$$U^1_{opt}(k,k') = (N-1)t(q)\tilde{\rho}(q) \tag{A.18}$$

or in terms of the NN scattering amplitude, $M(q)$,

$$U^1_{opt}(q) = -\frac{1}{(2\pi)^2}\frac{2\hbar^2}{m}(N-1)M(q)\tilde{\rho}(q) \tag{A.19}$$

where it is the neglect of the target nucleon momentum that allows the factorization to be performed.

Appendix B

$\vec{p}$-$^3\vec{He}$ Elastic Scattering Data

Table B.1: Data for 3He(p,p) scattering at 200 MeV

θ_{lab}	q	σ_{cm}	Δ	A_{NO}	Δ	A_{ON}	Δ	A_{NN}	Δ
24.00	1.34	4.5579	0.1300	0.7470	0.014	0.294	0.019	0.415	0.028
27.50	1.52	2.9778	0.0890	0.5860	0.013	0.257	0.019	0.346	0.029
31.00	1.70	1.9114	0.0590	0.3530	0.012	0.159	0.018	0.280	0.030
34.50	1.88	1.2706	0.0410	0.1030	0.014	0.101	0.020	0.212	0.036
38.00	2.05	0.8226	0.0270	-0.1020	0.015	-0.030	0.019	0.193	0.036
43.00	2.28	0.4520	0.0176	-0.4020	0.023	-0.066	0.029	0.178	0.054
48.00	2.51	0.2528	0.0082	-0.6160	0.015	-0.196	0.021	0.295	0.033
53.00	2.72	0.1556	0.0054	-0.7150	0.019	-0.282	0.029	0.302	0.043
58.00	2.92	0.0955	0.0033	-0.7120	0.019	-0.386	0.031	0.304	0.043
63.00	3.11	0.0665	0.0024	-0.6110	0.022	-0.399	0.036	0.187	0.052
68.00	3.28	0.0479	0.0018	-0.4400	0.026	-0.483	0.042	0.003	0.061
73.00	3.44	0.0368	0.0016	-0.2340	0.031	-0.460	0.049	-0.232	0.077

Table B.2: Data for 3He(p,p) scattering at 290 MeV

θ_{lab}	q	σ_{cm}	Δ	A_{NO}	Δ	A_{ON}	Δ	A_{NN}	Δ
24.0	1.64	2.99623	0.101	0.530	0.005	0.264	0.011	0.159	0.017
27.5	1.87	1.73473	0.055	0.284	0.006	0.183	0.009	0.128	0.015
31.0	2.09	0.89081	0.029	0.012	0.011	0.116	0.018	0.100	0.029
34.5	2.30	0.43265	0.015	-0.292	0.014	0.013	0.022	0.097	0.032
38.0	2.51	0.22449	0.009	-0.583	0.024	-0.005	0.037	0.137	0.056
43.0	2.80	0.09653	0.005	-0.857	0.021	-0.127	0.026	0.111	0.040
48.0	3.07	0.05123	0.0028	-0.754	0.033	-0.160	0.043	0.111	0.079
53.0	3.33	0.03612	0.0022	-0.416	0.054	-0.143	0.070	0.081	0.127
58.0	3.57	0.02779	0.0017	-0.149	0.050	-0.154	0.062	-0.071	0.114
63.0	3.79	0.02112	0.0012	-0.002	0.061	-0.177	0.077	-0.212	0.139
68.0	4.00	0.01684	0.0009	0.065	0.077	-0.199	0.096	-0.258	0.172
73.0	4.20	0.01292	0.0007	0.106	0.052	-0.143	0.064	-0.355	0.127

Table B.3: Data for 3He(p,p) scattering at 400 MeV

θ_{lab}	q	σ_{cm}	Δ	A_{NO}	Δ	A_{ON}	Δ	A_{NN}	Δ
24.0	1.975	1.508	.050	.292	.015	.262	.024	.028	.035
27.5	2.245	.599	.020	-.044	.015	.266	.023	.032	.023
31.0	2.509	.207	.0073	-.468	.017	.207	.024	.088	.040
34.5	2.765	.0742	.0030	-.818	.023	.069	.030	.027	.052
38.0	3.014	.0417	.0020	-.521	.030	-.074	.041	-.104	.071
43.0	3.354	.0364	.0015	.201	.026	.034	.035	-.331	.061
48.0	3.676	.0302	.0013	.338	.030	.125	.043	-.372	.070
53.0	3.979	.0210	.0011	.326	.034	.198	.047	-.420	.080
58.0	4.263	.0129	.00075	.235	.040	.227	.054	-.479	.094
63.0	4.527	.00776	.00061	.076	.057	.214	.075	-.508	.134
68.0	4.772	.00462	.00047	-.049	.073	.188	.098	-.513	.170
73.0	4.997	.00318	.00037	-.154	.092	.031	.124	-.442	.216

Table B.4: Data for 3He(p,p) scattering at 500 MeV

θ_{lab}	q	σ_{cm}	Δ	A_{NO}	Δ	A_{ON}	Δ	A_{NN}	Δ
24.0	2.25	0.5243	0.0190	0.0170	0.015	0.283	0.021	0.021	0.038
27.5	2.56	0.1188	0.0067	-0.4820	0.032	0.292	0.042	-0.029	0.079
31.0	2.86	0.0423	0.0030	-0.5370	0.057	0.065	0.078	-0.165	0.141
34.5	3.15	0.0406	0.0020	0.2560	0.029	0.052	0.040	-0.318	0.074
38.0	3.43	0.0436	0.0018	0.4650	0.041	0.240	0.061	-0.327	0.058
43.0	3.82	0.0348	0.0013	0.4020	0.024	0.240	0.036	-0.379	0.061
48.0	4.18	0.0189	0.0011	0.2380	0.037	0.267	0.053	-0.363	0.090
53.0	4.52	0.0101	0.0008	0.1270	0.052	0.261	0.074	-0.454	0.127
58.0	4.84	0.0039	0.0004	0.0700	0.082	0.146	0.117	-0.434	0.201
63.0	5.13	0.0020	0.0003	0.0010	0.116	0.254	0.168	-0.531	0.295